HHS Public Access

Author manuscript

Chem Soc Rev. Author manuscript; available in PMC 2020 April 01.

Published in final edited form as:

Chem Soc Rev. 2019 April 01; 48(7): 2053–2108. doi:10.1039/c8cs00618k.

Photothermal Therapy and Photoacoustic Imaging *via* Nanotheranostics in Fighting Cancer

Yijing Liu[#a], **Pravin Bhattarai**[#b], **Zhifei Dai**[b,*], and **Xiaoyuan Chen**[a,*]

[a]Laboratory of Molecular Imaging and Nanomedicine, National Institute of Biomedical Imaging and Bioengineering, National Institutes of Health, Bethesda, MD 20892, USA

[b]Department of Biomedical Engineering, College of Engineering, Peking University, Beijing 100871, China

[#] These authors contributed equally to this work.

Abstract

The nonradiative conversion of light energy into heat (photothermal therapy, PTT) or acoustics (photoacoustic imaging, PAI) have been intensively investigated for the treatment and diagnosis of cancer, respectively. By taking advantage of nanocarriers, both imaging and therapeutic functions together with the enhanced tumour accumulation have been thoroughly studied to improve the pre-clinical efficiency of PAI and PTT. In this review, we first summarize the development of inorganic and organic nano photothermal transduction agents (PTAs) and strategies for improving the PTT outcomes, including applying appropriate laser dosage, guiding the treatment *via* imaging techniques, developing PTAs with absorption in the second NIR window, increasing photothermal conversion efficiency (PCE), and also increasing the accumulation of PTAs in tumours. Second, we introduce the advantages of combining PTT with other therapies in cancer treatment. Third, the emerging applications of PAI in cancer-related research are exemplified. Finally, the perspectives and challenges of the PTT and PAI for combating cancer, especially regarding their clinical translation, are discussed. We believe PTT and PAI having noteworthy features would become promising next-generation non-invasive cancer theranostic techniques and improve our ability to combat cancers.

1. Introduction

Cancer is a major cause of morbidity and mortality worldwide. Each year, there are about 14 million new cancer patients and 8 million people die from cancer-related diseases. Given the high risk and death rate of cancer, researchers around the world have been struggling to develop more accurate and rapid diagnostic strategies and effective therapies to fight against cancer.[1] The most traditional cancer therapies include chemotherapy, radiotherapy, and surgery, in which the patients may suffer from serious side effects and unsatisfied treatment outcomes.[2–5] These treatment failures have motivated the development of precise and more effective treatment strategies to deal with cancer. The emerging therapies in cancer treatment include but are not limited to immunotherapy,[6, 7] gene therapy,[8, 9] photodynamic therapy

[*]**Corresponding Authors** shawn.chen@nih.gov, zhifei.dai@pku.edu.cn.

(PDT),[10] photothermal therapy (PTT),[11, 12] which have improved or can potentially improve the therapeutic outcomes. PTT makes use of the photothermal effect of photothermal transduction agents (PTAs) that can harvest the energy from light and convert the energy into heat to increase the temperature of the surrounding environment and trigger the death of cancer cells.[13, 14] Among different therapies, PTT offers certain advantages: the use of external laser irradiation with adjustable dosage allows precise targeting at tumours so that the damage to surrounding healthy tissues could be minimized; more notably, PTT is a highly effective and non-invasive therapy that is capable of eliminating various types of cancers.[15]

Exogenous PTAs with higher accumulation in tumours than surrounding normal tissues are expected to enhance the PTT outcomes.[16, 17] An ideal PTA should have higher photothermal conversion efficiency (PCE), an absorption that does not overlap with the tumour background and good accumulation in tumours. The occurrence of a variety of PTAs accelerates with the advancement on PTT study.[18–22] In particular, nano PTAs that can accumulate in tumours through enhanced permeability and retention (EPR) effect and active targeting are noteworthy.[23–26] In addition, nano PTAs can achieve higher PCE than small molecular PTAs and potentially integrate multiple imaging modalities and therapeutic functions into one platform for advanced applications.[27–29] In the following part of the review, PTAs are considered as nano PTAs unless otherwise stated. Tremendous efforts have been made toward improving the PTT performances, due to the presence of certain disadvantages or biological barriers that limit the effectiveness of PTT on cancer treatment. The biggest problem of PTT is the limited depth of light penetration, which may lead to incomplete ablation of tumours outside the scope of irradiation. Besides that, other disadvantages include relatively low delivery efficiency of PTAs in tumours, overheating of the tumour area for unnecessary damage to normal tissues, and development of resistance to PTT due to the overexpression of heat shock proteins in certain cancers.[14] A lot of progress has been made to overcome these shortcomings, such as adopting proper laser dosage,[30–32] determination of the best treatment time after administration of PTAs,[33] improving the PCE of PTAs,[34–36] developing PTAs with absorption in the second NIR window,[37–41] and enhancing the delivery efficiency of PTAs in tumours by modulation of nanoparticles' (NPs') shape, size, and surface chemistry or tumour microenvironment (TME).[42–47] In addition, combinations of PTT with other therapies have shown improved treatment outcomes. In many cases, the treatment outcomes of combined therapies are not a simple sum of the effect of each therapy alone, but rather a synergistic effect. PTT can directly kill cancer cells or augment other therapies by improving drug delivery efficiency, stimulating the drug release, modulating TME, eliciting tumour-specific antigen release, or influencing other biological related responsiveness.[48–53] With these achievements, improved treatment outcomes have been observed.

In addition to killing cancer cells, the photothermal effect can generate acoustic waves that can be detected and converted into imaging signals, which is called photoacoustic imaging (PAI).[54] This technique not only provides us an alternative imaging modality for tumour diagnosis, but also enables the detection of several biologically relevant signals in a TME, such as acidic pH, certain enzymes, and reactive oxygen species (ROS).[55, 56] Furthermore, PAI can be useful to assist the operation of surgery by providing instant diagnostic functions.

[57] In most cases, PTAs can be used for PTT and PAI simultaneously, thus could be intrinsic theranostic platforms.

The past few decades have witnessed rapid advances in NP synthesis and the development of efficient and “smart” PTAs for PTT and PAI. Many comprehensive reviews have already been published on these topics, demonstrating the importance and potentials of PTT in scientific research and clinical practice.[11–15, 58–63] Our review includes the most up-to-date reports in photothermal cancer therapy and PAI. In this review, we summarize different types of materials as PTAs and strategies to enhance the efficiency of PTT, discuss examples of combinational therapies by using PTT together with other therapies and introduce the emerging applications of PAI in cancer-related research. Finally, the perspectives and challenges of the PTT and PAI for combating cancer are discussed.

1. Classification and characteristics of PTAs

PTAs can transfer energy from absorbed light into heat to increase the temperature of the surrounding environment. Ideally, PTAs are expected to only increase the temperature locally to reduce the damage to healthy tissues, where the PTA is absent or outside the scope of laser irradiation. To achieve this goal, the absorptions of PTAs are usually adjusted to the tissue-transparent window between 750 and 1350 nm, including both first (750–1000 nm) (NIR-I) and second (1000–1350 nm) (NIR-II) NIR windows.[15] PTAs can be divided into inorganic materials and organic materials (Figure 1). The inorganic materials include noble metal materials,[64, 65] metal chalcogenide materials,[66] carbon-based nanomaterials (*e.g.*, graphene and carbon nanotubes),[20] and other two-dimensional (2D) materials (*e.g.*, black phosphorus, nanosheets, boron nitride, and graphitic carbon nitride, MXenes).[67, 68] The organic PTAs include NIR-responsive small molecules and semiconducting polymer NPs (SPNPs).[55, 69] Generally, inorganic PTAs own higher PCE and better photothermal stability than their organic counterparts. But organic PTAs may win out in terms of biodegradability and biocompatibility. Even with these pros and cons, no conclusion has been drawn regarding which type of PTA is the best for PTT yet. Scientists have made great efforts to further improve the photothermal properties and overcome the shortcomings of different types of materials.

2–1. Noble metal materials

Noble metal materials, which are known to be strongly resistant to oxidation, are one type of most studied inorganic PTAs. Noble metal PTAs, including Au, Ag, Pt, and Pd, can absorb laser light to excite electrons from the ground state to the excited state, followed by the release of energy in the form of heat through nonradiative decay.[15] Among different materials, Au-based PTAs are most studied, due to the advances in their synthesis, their finely tuned absorption, ease of surface modification, and good stability in biologically related conditions.[70] On the surfaces of Au NPs, free conduction band electrons can be polarized by laser irradiation as long as the optical absorption of Au NPs is resonant with the wavelength of incident light, which is called localized surface plasmon resonance (LSPR).[14] The wavelength of LSPR peak is highly sensitive to the structures and sizes of Au NPs. Spherical Au NPs have their absorption peak at about 520 nm. The absorption peak of Au

NPs can be red-shifted by increasing their sizes or changing the structures from spherical to non-spherical shapes or introducing coupling within nanostructures. We have seen a variety of Au nanostructures reported, such as Au nanorods,[71] Au nanoshells,[72] Au nanocages,[73] Au nanorings,[43] Au nano vesicles,[74] and chiral Au NPs,[75] with their LSPR wavelengths ranging from visible to NIR region.[75] Since the first report of PTT with Au NPs in 2003,[76, 77] many literatures have been reported on this topic, demonstrating the importance of Au nanomaterials in PTT. One of the most studied Au-based PTAs is Au nanorods, which have aspect ratio-dependent absorption peak positions and excellent PCE.[78] Au nanorods have two absorption peaks, corresponding to the longitudinal peak in the NIR range and the transverse peak at about 520 nm. The advancement in Au nanorod synthesis, such as improving the yield and purity and adjusting sizes and aspect ratios,[79–83] has led to many successful examples of PTT with Au nanorods.[12, 84–86] The seed-mediated synthesis of Au nanorods was initially developed by Murphy *et al.*[87] Then El-Sayed *et al.* improved the synthesis yield of Au nanorods by using cetyltrimethylammonium bromide (CTAB) capped Au seeds and achieved well-controlled lengths and aspect ratios.[88] Later, Murray *et al.* further improved the monodispersity and expanded the dimensions of synthesized Au nanorods with well-defined lengths and diameters by combining CTAB with another surfactant, sodium oleate, during the synthesis (Figure 2a-i).[80] The longitudinal peaks can be tuned between 800 to 1200 nm by changing the aspect ratios (Figure 2j). However, Au nanorods exhibit relatively large size distribution, which results in the broadening of their longitudinal peaks with the full width at half maximum values between 100 to 200 nm and impaired photothermal effect. More recently, Guerrero-Martinez *et al.* reported the synthesis of Au nanorods with extremely narrow LSPR band *via* a reshaping process, in which the Au nanorods were irradiated by a femtosecond laser.[89] As an alternative to Au nanorods, Au nanobipyramids with sharper tips on both ends have been developed (Figure 2k). These Au structures are expected to have higher monodispersity, smaller width at half maximum values, and stronger electric field enhancement, which lead to improved photothermal performances.[90, 91] Though with many advantages, the application of Au nanorods or Au nanobibypramids in PTT has some limitations, including the use of toxic CTAB as stabilizing ligands, unsatisfied photothermal stability, or lack of payloads holding space. To address these issues, Au nanostructures free of CTAB with anisotropic shapes or sharp branches or internal gaps, such as Au nanorings, Au nanostars, Au nanoshells, have been reported, providing alternative choices for PTAs.[43, 72, 92–97] To provide space for drug loading, hollow Au nanostructures, such as Au nanocages and Au vesicles, or Au nanomaterials coated by additional materials, such as polymer or silica (SiO_2), have been developed.[47, 73, 98–101] For example, Xia *et al.* developed hollow Au nanocages through galvanic reaction by using silver nanocubes as templates (Figure 2l). The Au nanocages were modified by the thermal sensitive polymers, poly(N-isopropylacrylamide) (pNIPAAm)-co-poly acrylamide (AAm), to cover the openings on their surfaces for photothermally controlled drug release. Upon irradiation by a NIR laser, the temperature increase induces the collapse of polymer valves and exposure of openings on Au nanocages, from which the encapsulated payload could leak out.[98] Li *et al.* prepared hollow Au nanospheres through galvanic reaction with cobalt NPs as templates.[102] Because of the high surface area of hollow Au NPs, exceptionally high amount of doxorubicin (Dox) was able to be loaded into NPs. Nie *et al.* reported the amphiphilic block copolymer-mediated self-assembly of Au NPs

into hollow vesicles, which were able to simultaneously hold hydrophilic and hydrophobic payloads in their central void and hydrophobic membrane, respectively. The release of payload from Au vesicles was triggered by laser irradiation, which destabilized the integrity of vesicles.[95, 97]

Other noble metals, such as Pd or Pt, have also been applied as PTAs for PTT. Compared to Au-based PTAs, Pd and Pt-based PTAs have better photothermal stability and some catalytic properties. The NIR responsive Au-based PTAs, such as Au nanorods, would melt into spherical Au NPs under NIR irradiation due to the low melting point of Au, which reduced their PCE due to the shift of absorption peaks away from the wavelength of the laser. On the contrary, the Pd or Pt-based PTAs can maintain their structures better under laser irradiation due to their higher melting points.[103] Scientists have been trying to further improve the performances of Pd or Pt-based PTAs by enhancing the absorption in the NIR range. Zheng *et al.* synthesized the free-standing Pd nanosheets with a thickness of 1.8 nm with tunable NIR absorption peaks from 826 nm to 1068 nm by increasing their edge lengths (Figure 2m,n). These Pd nanosheets not only generated a significant photothermal effect but also maintained their shapes and absorption peaks and intensities even after being exposed to a NIR laser for a long time.[103] More notably, these PTAs can have NIR absorption even at a smaller size than an Au-based PTAs. NPs with sizes smaller than 5 nm are able to clear from kidneys and have a higher chance for clinical translation. Unlike Au-based PTAs, Pd nanosheets can keep their strong absorption in the NIR range even with size below 5 nm. In another study from the same group, Zheng *et al.* developed small-sized Pd nanosheets with an average diameter of 4.4 nm. The small Pd nanosheets not only had good photothermal property, but also demonstrated prolonged circulation time, good tumour uptake, and renal clearable property.[104] Besides Pd nanosheets, small-sized Pt NPs can also be used as PTAs, even though they don't have an absorption peak in the NIR range. Cheng *et al.* developed a dendrimer mediated wet-chemical synthesis method to prepare CuS, Pt, and Pd NPs with ultra-small sizes. Among them, the Pt NPs with an average diameter of 1.5 nm measured from TEM, showed the best photothermal properties. Coupled with tumour targeting ligands, these ultra-small sized Pt NPs showed high tumour accumulation at 24 h postinjection and led to significant tumour regression after PTT.[105] In addition to good photothermal properties, Pd or Pt-based PTAs have some catalytic properties, which can be incorporated with PTT to enhance the overall treatment outcomes.[106] Overall, the noble metal-based PTAs have shown great potential in PTT due to their excellent photothermal and optical properties. However, the noble metal-based PTAs are facing high cost and nondegradable issues, which must be overcome for clinical translation.

2–2. Graphene and graphene analogue-based PTAs

The limitations of noble metal-based PTAs in PTT have motivated scientists to seek other inorganic materials as PTAs. Alternatively, carbon-based materials, such as carbon nanotubes, graphenes, graphene oxides, carbon dots, which have broad optical absorptions and reasonable photothermal properties, have attracted great attention.[107, 108] Particularly notable is the graphene, exfoliated by Novoselov and Geim *et al.* in 2004 (Nobel Prize 2010), has many unique characteristics, including large surface-to-volume ratio, excellent electrical and optical properties.[67] Although there is still room to improve their PCE, the

emergence of these carbon-based PTAs have accelerated the development of other graphene analogues, such as transition metal dichalcogenides (TMDs),[109, 110] transition metal oxides (TMOs),[111] MXenes,[22, 68] hexagonal boron nitride (*h*-BN),[112] carbon nitride (*g*-C_3N_4),[113] black phosphorus,[114–116] which either have improved photothermal properties, degradability, or biocompatibility.[113]

Carbon nanomaterials, such as graphene oxide and carbon nanotubes, have been intensively studied as PTAs, due to their elongated conjugation bands with strong NIR light absorption. Compared to carbon nanotubes, graphenes are expected to have better photothermal anticancer activity.[117] Graphene is a single-atom-thick graphite, in which carbon atoms covalently link to other neighbouring carbon atoms into a hexagonal-packed 2D network. Its atomic thickness and the surface-confined and conjugated electrons have endowed the materials with some compelling electronic and optical properties, both excellent mechanic properties and flexibility, and high surface area.[67] Because of its unique structure and electronic properties, graphene shows plasmonic properties, which can convert energy from the laser into heat through plasmonic photothermal effect.[20] Graphene can be prepared by exfoliation through mechanic force or thermal treatment, epitaxial growth, and chemical vapour deposition. The most common method to produce graphene is the chemical reduction of the exfoliated graphene oxide made from graphite oxide. Both graphene oxide and reduced graphene oxide have been applied in PTT.[118, 119] Liu *et al.* first investigated the *in vivo* behaviours of PEGylated graphene oxide nanosheets and their application in PTT. The graphene oxide nanosheets showed better accumulation in tumours compared to other reported results of carbon nanotubes, which may be related to its 2D structural property. No noticeable toxicity was observed from the graphene oxide nanosheets after their systemic administration and complete tumour regression was observed after PTT.[118] Compared to its oxidized form, the reduced graphene oxide significantly increases its absorption in both visible and NIR regions. Dai *et al.* prepared water-soluble single-layer reduced graphene oxide nanosheets with a diameter of 20 nm by reducing the PEGylated graphene oxide with hydrazine monohydrate (Figure 3a).[120] The resulted reduced graphene oxide maintained its water solubility and showed 6 times enhancement of light absorption at the wavelength of 808 nm (Figure 3b). The enhancement was due to the improved π conjugation of the electrons in reduced form compared to its oxidized counterpart. Owing to the large surface area, the reduced graphene oxide nanosheets are capable of delivering chemotherapeutics with high loading efficiency *via* non-covalent interactions to achieve enhanced treatment outcomes. One problem associated with reduced graphene oxide as PTAs is that it is water insoluble and requires additional surface modification before it can be applied for *in vivo* applications.

Encouraged by the rapid progress of graphene in PTT, many other graphene analogues have been developed to further enhance the PTT efficacy. These materials have similar chemical structures as graphene and, therefore, excellent optical and electronic properties and large surface area, comparable to or even better than graphene. Especially, many of them can be dispersed in water directly after preparation, which is suitable for biomedical applications. Among these materials, 2D TMDs, TMOs, and MXenes have attracted a lot of attention due to their excellent photothermal properties.[22, 111, 121] TMDs or TMOs are made from a transition metal, such as molybdenum (Mo), tungsten (W), titanium (Ti), and chalcogen

atoms, such as sulfur (S), selenium (Se), tellurium (Te), or oxygen (O) atoms. These materials display strong optical absorption in the NIR region and good photothermal properties, due to their thickness-dependent quantum size effect and tuneable crystal structures, leading to their well performance in PTT and other related applications.[67] For instance, a single layer MoS_2 nanosheet is composed of a sandwich-like structure, with a layer of positively charged Mo between two layers of negatively charged S connected *via* covalent interactions. In bulk materials, MoS_2 nanosheets are bonded through weak van der Waals interactions.[122] The exfoliation of raw materials will produce MoS_2 nanosheets, accompanied by the occurrence of some new properties, such as photoluminescence and strong NIR absorption.[21] In addition, both Mo and S are life-containing elements, which render MoS_2 nanosheets relatively good biocompatibility. Dravid *et al.* chemically exfoliated MoS_2 nanosheets by intercalating MoS_2 nanosheets with lithium, followed by their ultrasonication in water. The oxidization of alkali metals and formation of H_2 gas broke the MoS_2 powder into nanosheets. The obtained thin MoS_2 nanosheets were water soluble and demonstrated NIR absorption at 808 nm comparable to that of reduced graphene oxide and higher than graphene oxide and Au nanorods.[123] The chemical exfoliation method, so-called 'top-down' method is time and energy consuming. As an alternative, the MoS_2 nanosheets can also be prepared by chemical synthesis, so-called 'bottom-up' method. Shi *et al.* reported the synthesis of MoS_2 nanosheets in an aqueous solution of polyethylene glycol (PEG) *via* a solvothermal method (Figure 3c). The PEG chain can bind to the surfaces of MoS_2 nanosheets during their synthesis to enhance their stability and water solubility. Through this method, the MoS_2 nanosheets can be produced with high yield and have good dispersion in water, inherent stability under physiological environment, and adjustable sizes.[124] MoS_2 nanosheets with piece diameters of 50.4, 79.2, 103.1, 194.9, and 297.5 nm were produced (Figure 3d-h), of which MoS_2 nanosheets with a diameter of 79.2 nm showed the highest photothermal efficiency. The 80 nm MoS_2 nanosheets were applied to PTT against a 4T1 tumour model, leading to complete elimination of tumours.

Recently, MXenes, a new type of graphene analogue, have been used as PTAs. The MXenes have a general formula of $M_{n+1}X_n$, in which M and X represent transition metal elements (*e.g.*, Ti, tantalum (Ta), Mo, niobium (Nb), vanadium (V), and zirconium (Zr), *etc.*) and carbon (C) or nitrogen (N), respectively.[68, 107] Compared to reduced graphene oxide, MXenes have higher light absorption, probably due to the higher electronic conductivity. Many examples of photothermally induced ablation of tumours derived from MXenes have been demonstrated, such as, Nb_2C, Ti_3C_2, and Ta_4C_3.[125, 126] MXenes are prepared by selectively etching away the A-layer from raw MAX phases, in which A stands for element from group IIIA or IVA.[67] The etching is usually achieved by introducing acidic media, such as hydrogen fluoride or fluoride containing acid. More recently, Geng *et al.* made use of a new etchant, tetramethylammonium hydroxide, to prepare Ti_3C_2 nanosheets terminated with $Al(OH)_4^-$. This strategy not only facilitated the delamination of Ti_3AlC_2 into the thin-layered structure but also introduced Al oxoanions on nanosheets, enhancing their NIR absorption and photothermal properties.[126] The obtained Ti_3C_2 nanosheet showed an extinction coefficient of 29.1 L $g^{-1}cm^{-1}$, which was higher than Au nanorods and some TMD materials. Later, Shi *et al.* reported the synthesis of ultrathin 2D MXene named as tantalum carbide (Ta_4C_3), which showed even higher PCE than traditional Ti_3C_2 nanosheets

and could serve as X-ray computed tomography (CT) contrast agents due to the presence of high Z element of Ta.[22] In another work of Shi *et al.*, a biodegradable ultrathin Nb_2C nanosheets were reported (Figure 3i-k). The Nb_2C nanosheets exhibited absorption in both NIR-I and NIR-II windows and outstanding photothermal conversion efficiencies of 34.9% and 46.65% upon irradiation by an 808 nm and a 1064 nm laser, respectively. Their unique enzyme-responsive biodegradability to human myeloperoxidase is another advantage over other inorganic PTAs.[127]

Recently, black phosphorus has gained more and more attention as PTAs or in other biomedical applications, due to its unique structure and properties, good biocompatibility, and biodegradability.[114–116, 128, 129] Each of its layer is a bilayer structure in the zigzag direction, in which one phosphorous atom is connected to three adjacent phosphorus in two different planes. It exhibits tuneable bandgap and absorption range, good photothermal performances, and can be degraded into non-toxic intermediates, such as phosphate and phosphonate, upon reacting with water and oxygen.[116, 130] As an example, Cao *et al.* have developed a black phosphorus-based hydrogel, from which controllable drug release was achieved through manipulation of external laser stimuli. The entire black phosphorus-based drug delivery hydrogel was nontoxic and completely degraded *in vivo*.[115] The degradation rate of black phosphorus can also be adjustable. For example, Chu *et al.* prepared black phosphorus quantum dots loaded nanospheres by wrapping the black phosphorus quantum dots in poly (lactic-co-glycolic acid) (PLGA). The formation of PLGA shell outside black phosphorus quantum dots reduced access of black phosphorus toward water and, therefore, the degradation rate.[129]

2–3. Other inorganic PTAs

Besides above introduced materials, many other examples of transition metal-based PTAs, such as quantum dots, metal oxide NPs have been reported. The light harvested by quantum dots can be partially converted into heat through non-radiative decay besides fluorescence emission, the process of which is related to NP structures. For example, Chen *et al.* prepared Ag_2S quantum dots with different sizes and found that Ag_2S quantum dots with the largest diameter of 9.8 nm had the optimal PCE.[131] Copper chalcogenides, such as CuS, $Cu_{2-x}S$, and $Cu_{2-x}Se$ have also been applied as PTAs due to their good PCE.[29, 132–135] Chen *et al.* reported the synthesis of the CuS NPs in the cavity of ferritin with an average size of 8 nm and uniform size distribution.[29] The obtained NPs had good biocompatibility and PCE. Metal oxide NPs, such as iron oxide NPs, show black colour and can be used as PTAs. Wu *et al.* reported the solvothermal synthesis of Fe_3O_4 nanoflowers with controllable size.[136] The NPs were demonstrated to be both PTAs and magnetic resonance imaging (MRI) contrast agents. In another example, the same group investigated the optimization of titanium oxide-based materials as PTAs.[137] Traditional TiO_2 NPs have wide bandgap and do not absorb in the NIR region. In their work, Ti_8O_{15} NPs with Magnéli phase were prepared by an arc-melting technique and compared with anatase and rutile TiO_2 materials. The Ti_8O_{15} NPs with Magnéli phase had NIR absorption and better photothermal effect.

2–4. Small molecule-based PTAs

Organic molecules having longer wavelength especially in the NIR-I range and beyond are suitable for biomedical applications including imaging (photoacoustic) and therapy (PTT).[17] Ideally, design and fabrication of organic PTAs should encompass some basic prerequisites for effective PTT: (i) high level of safety and ease to modify formulation, (ii) ability to tune the optical properties in the NIR region *via* dedicated synthesis, (iii) high PCE achieved by reducing singlet oxygen generation yield/fluorescence quantum yield (QY), (iv) excellent biodegradability for the clearance *in vivo*, and (v) light-specific toxicity in the selected regions, *e.g.* tumour cells only.[16, 17, 138] So far, significant progress has been made in the design of organic molecular PTAs together with improved photophysical and chemical properties. To date, NIR-absorbing organic PTAs based on (i) small molecules (cyanine, porphyrin, BODIPY, phthalocyanine, croconaine), and (ii) SPNPs have demonstrated excellent therapeutic efficacy and are studied extensively as a potential PTT agent. Organic small molecule-based PTAs, such as cyanine dyes and porphyrin, have been frequently used in both imaging and therapy of cancer.[139, 140] But they share the same disadvantages, including poor aqueous solubility, limited tumour accumulation, bioavailability, photobleaching, and low photothermal efficiency. Unlike delivery of small molecules in free forms, nanocarriers based delivery tools outperform therapeutic efficacy *via* improved solubilization and pharmacokinetics, enhanced tumour penetration and retention *in vivo*, resistance to photobleaching, and increasing the photothermal efficiency.[141]

2–4-1. Cyanine—Cyanine dyes basically comprise of two aromatic nitrogen-containing heterocycles interconnected by a polymethine chain (also known as “push-pull” configuration).[142] The final characteristics of these dyes depends upon the number of aromatic rings and the polyenes length.[143] Interestingly, unlike other small molecules, cyanine structure is relatively flexible and allows facile modification at different positions of the carbon backbone. For instance, Cy3 having absorption and emission nearly in the visible region can be modified further by the addition of double bond resulting in a red-shift of ~100 nm or by extension of the nitrogen-containing heterocycles to redshift by ~20 nm.[138, 144] This can finely tune excitation/emission wavelength of cyanine dyes (Cy5/Cy7 > 650 nm) to fall in the NIR region. Nevertheless, the increase in the polyenes length or aromatic rings would make cyanines more susceptible to photobleaching and more hydrophobic. To overcome such limitations, various design strategies such as; implementation of a rigid chlorocyclohexenyl ring in the methine chain for better stability,[145] modification with sulfonate groups for enhanced solubility,[145] and conjugation with a small-molecule triplet-state quencher[146] for reduced photobleaching have already been proposed. Together with improved photophysical properties, excellent biocompatibility of cyanine dyes makes them an attractive candidate for biological applications including sensing and imaging.[147, 148] Similarly, cyanine dyes having strong NIR absorbance can also be used as molecular PTAs, provided that the incoming light energy is maximally converted into heat instead of fluorescence or singlet oxygen generation. To this end, cyanine molecules such as ICG, IR825, IR780 and Cypate endowed with excellent photophysical abilities (higher molar extinction coefficient: $>2 \times 10^5$ $M^{-1}cm^{-1}$ but weak fluorescent QY: 1–18%) have emerged as a potential candidate for PTT.[69] Among several cyanine dyes, only ICG has received Food and Drug Administration (FDA) approval and can be administered directly for

diagnostic purposes.[149] Nevertheless, these dyes are prone to degradation after prolonged and repeated exposure of NIR laser resulting in poor photothermal efficiency. This limitation was further addressed by the synthesis of new NIR absorbing dyes IR780 and IR825 having superior photostability over ICG/Cypate.[150, 151] The design of these dyes mainly has a rigid cyclohexenyl ring in the heptamethine chain that enables excellent photothermal abilities even after repeated exposure to NIR laser. This confers improved photostability of cyanine dyes for both fluorescence imaging and photothermal treatments of tumours. Although the Stokes shift and QY of cyanine dyes have great tuning flexibility for the relevant applications, it is important to note that the free dyes do not readily accumulate in the tumours and they are washed out quickly from the targeted regions. Therefore, further works related to the *in vivo* PTT of tumours using such small molecules are explicitly based on the delivery *via* nanocarriers. To date, plethora of findings have highlighted the relative improvement in the photophysical properties of cyanine dyes by harnessing the potential of NPs mainly because (i) NPs loaded with many chromophores have higher absorption cross section compared to single organic dye, (ii) NPs can reduce photobleaching of small molecules *via* activated quenched state possibly due to intermolecular dye interactions, (iii) NPs can increase aqueous solubility and (iv) improve blood-circulation time of small molecular PTAs.[152] So far, organic nanocarriers such as polymeric micelles, vesicles, and liposomes have been mostly used for cancer theranostics including PTT. For instance, IR825 dye has a higher absorption coefficient and lower fluorescence quantum yield that makes it a suitable PTA. However, its therapeutic application is largely restricted due to its very low water solubility and minimal tissue uptake. By taking advantage of nanocarriers, Zhao *et al.* incorporated IR825 in thermoresponsive liposomes to enhance bioavailability and photothermal effect *in vivo*.[153] The simple fabrication strategy to yield liposomal NPs eliminates substantial modification of cyanine dyes at the molecular level and endows additional advantage to co-encapsulate other drugs for combination therapy as well. In addition to this, liposomes are also used to load amphiphilic cyanines such as ICG. The lipophilic polyaromatic polyene tail of amphiphilic ICG molecules can be inserted into the hydrophobic bilayer while the hydrophilic sulfonate head can face both interior aqueous core and the exterior hydrophilic environment. Such spatial arrangement of small molecules may differ according to the class of nanocarriers and are often implicated with varying degrees of photothermal efficacy. To this end, Park *et al.* recently reported that the arrangement of ICG in the lipid bilayer and subsequent interaction with phospholipids was able to regulate the PCE in phototherapeutic applications.[154] The optimized ICG-liposomal composition (DMPC:PEG-PE:ICG=950:50:4) showed better antitumour effect *in vivo* than the free ICG and other liposomal formulations. The relatively large size of liposomes may result in compromised tumour retention and uptake. Therefore, smaller sized nanocarriers such as micelles have comparative advantages of improved circulation time, higher tumour retention and enhanced PTT outcomes *in vivo*. To this goal, Wu *et al.* recently prepared nanomicelles by the self-assembly of IR825 conjugated amphiphilic block copolymers methoxypoly(ethylene glycol)-block-poly(L-aspartic acid sodium salt) (PEG-PLD-IR825).[155] Besides excellent PCE, photothermal ablation, and tumour specificity, these micelles had high drug loading (~21%), sustained tumour retention, prolonged circulation half-life, mitochondrial accumulation, and negligible premature release of cyanine while in circulation *in vivo* (Figure 4a). Notably, mitochondrial localization of micelles favoured

higher PTT after NIR irradiation at a relatively low drug concentration (50 μg mL^{-1}) as observed in the HeLa cells *in vitro*. However, most of the cyanines including aforementioned IR825 are prone to photobleaching as observed by the change from coloured to colourless sample solution after repeated laser irradiation. Therefore, a more versatile micellar system that can possibly reduce photobleaching and enhance PCE is desirable. In a recent example, Chen *et al.* fabricated polymeric micelles encapsulating Cypate as PTAs (CA-Micelles) (Figure 4b).[156] It was observed that the micelles could reduce the photobleaching of Cypate after encapsulation, enhance cellular uptake *via* co-loaded 17-AAG (HSP90 inhibitor), resulting in better tumour accumulation and PTT. In brief, cyanine based nanoprobes for PTT have received considerable attention and improvisation, however, some fundamental limitations ascribed to compromised PCE, photo-stability and tumour specificity requires further investigation.

2–4-2. Porphyrin—Porphyrins with four pyrrole subunits interconnected by methane bridges and their subsequent derivatives (including chlorins and bacteriochlorins) having well-suited photophysical properties are pivotal in clinical phototherapy and imaging.[157] Such porphyrins have gained huge attraction in both diagnostic imaging such as MRI, fluorescence imaging; and therapies such as PDT, radiotherapy and sonodynamic therapy (SDT).[158–160] At present, two porphyrin constituents, Photofrin, a complex mixture of hematoporphyrin derivatives, and benzoporphyrin derivative verteporfin (Visudyne) are approved by FDA as photosensitizers (PS) for PDT in the USA.[161, 162] Nevertheless, monomeric porphyrin structures are susceptible to poor aqueous solubility, limited tumour accumulation, bioavailability, and adverse skin photocytotoxicity. To overcome challenges of monomeric porphyrin delivery and enhance their biological/physiochemical properties, a robust supramolecular based approach where these monomers can assemble *via* intermolecular forces have been studied extensively.[163, 164] The design of supramolecular structures such as dendrimers, liposomes, microbubbles (MBs), polymers, micelles, films and inorganic NPs (silica, metals) are routinely investigated to enhance the penetration ability of deeply-suited tumours, phototherapeutic killing *in vivo* and other several combination therapies.[27, 165, 166] Recently, Zheng *et al.* have summarized advancements in the design of porphyrin supramolecular chemistry for enhanced therapeutic outcomes.[139] For instance, higher therapeutic killing at a relatively low dose of porphyrin, long circulation time, excellent biocompatibility even at high dosing, and increased uptake by tumour cells were successfully validated by using different porphyrin-based supramolecular structures.[167–170] Specially, porphyrins and derivatives having large extinction coefficients have been mostly investigated for PDT.[171] The ability of these molecules to generate a large number of reactive oxygen species (ROS) *via* type-II mechanism (dominant) have been successfully translated for cancer theranostics. Although porphyrins have been the foundation of PDT, Zheng *et al.* recently reported the novel application of porphyrin as an organic PTA that has comparable optical absorption to Au NPs depicting high photothermal efficiency.[19] These phospholipid-porphyrin conjugates could self-assemble to form a liposome-mimicking structure denoted as ‘porphysomes’, having a high loading capacity of porphyrin, excellent biocompatibility, and high NIR absorption ability. The porphysomes demonstrated high extinction coefficient (ε_{680}) of 2.9×10^9 $M^{-1}cm^{-1}$ due to the dense packing of porphyrins (~8×10^4 porphyrins in a single porphysome). Self-quenched porphysomes, therefore, could

release energy mainly in the form of heat instead of fluorescence or singlet oxygen generation with an efficiency to that of plasmonic NPs such as Au. Such mechanism is not applicable to monomeric porphyrins and is solely result of highly-quenched state *via* the self-assembly of high-density porphyrins in a form of the organic nanostructure. Zheng *et al.* further successfully compared the PTT *vs.* PDT efficiency of these porphysomes especially considering the hypoxic and hyperoxic tumours.[172] The results showed clear evidence of complete tumour eradication and overall survival for the mice treated with porphysomes as a PTT in both hypoxic and hyperoxic situations. To pursue excellent phototherapy, more robust nanocarriers having stimuli-responsive properties are also being investigated. Recently, Li *et al.* reported a self-assembled polymeric micelle (poly(ethylene glycol)-block-poly(diisopropanol amino ethyl methacrylate cohydroxyl methacrylate) (PEG-b-PDPA, referred to as PDPA)) conjugated to Ce6 that can function as a both PTT and PDT agent under single laser irradiation of 655 nm (Figure 4c).[173] The phototherapeutic ability was mainly dependent upon the intracellular acid-switchable property of PDPA micelles in TME. Under acidic environment, the responsive core-shell micelles switched from PTT mode which was mainly from the packed porphyrin structures to PDT after disintegration to the monomers (pH ≤ 6.2). Interestingly, the PCE of micelles was independent of the pH change (only dependent upon micelle concentration or the power density) but the singlet oxygen generation was highly pH dependent as observed with a ROS indicator (9,10-anthracenediylbis(methylene)dimalonic acid (ABDA)) *in vitro* (Figure 4d). Collectively, significant hyperthermia combined with singlet oxygen generation demonstrated excellent synergistic therapy both *in vitro* and *in vivo*. Recently, Hedley *et al.* have reported the feasibility study of porphysomes as a PTA for successful treatment of pancreatic cancer in a well-established patient-derived orthotopic xenograft model.[174] This envisages the potential role of porphysomes for future PTT-related pre-clinical studies.

2–4-3. Other Small Molecules—Beside porphyrins and cyanines, there have been a variety of other organic molecular PTAs reported exhibiting photothermal activities.[16] Phthalocyanines having higher molar absorption and excellent optical stability are a good choice for PDT but are less studied for PTT.[175] Recently, Huang *et al.* reported the design of new copper phthalocyanine (PcC1) based small molecules that induced severe hyperthermia regardless of aggregation.[176] Although these small molecules have shown elevated temperature compared to ICG and methylene blue at 685 nm laser irradiation, the detailed *in vivo* studies are further required. In another experiment, Chen *et al.* investigated a wavelength dependent photoconversion characteristics of BODIPY fluorophore to trigger PDT and PTT under 660 nm and 785 nm laser irradiation respectively.[177] The polymeric vesicles loaded with high concentration of BODIPY revealed both J- and H-type aggregates resulting in the shift of absorption peak towards NIR region and a protective functional shield against photobleaching. No tumour regrowth was observed *in vivo* owing to the enhanced tumour accumulation and effective phototherapy of BODIPY NPs. In 2013, Smith *et al.* introduced the use of croconaine (Croc) dyes for effective PTT and negligible singlet oxygen generation at 780 nm laser irradiation.[178] The croconaine dyes having high molar absorption (~800 nm) and low fluorescence QYs collectively make them a suitable candidate for PTT. Moreover, ultralow singlet excited state lifetimes endowed resistance to photobleaching at repeated laser irradiation. Liu *et al.* recently reported the fabrication of

NPs assembled by human serum albumin (HSA) and croconaine dyes self-assembled NPs (HSA-Croc NPs) for pH-dependent PTT.[179] The HSA-Croc NPs with pH responsive NIR-absorption peak (~ 790 nm) at its zwitterionic acidic form showed enhanced photothermal efficacy towards large tumour compared to the pH-inert counterparts *in vivo*. Notably, this new design has possibly overcome past limitations such as high laser power and low hyperthermia that hindered effective PTT based on the use of Croc-dyes. However, more studies related to the biodistribution and clearance of these dyes *in vivo* are required to further validate the suitability for clinical PTT.

2–5. NIR-absorption SPNPs for PTT

Among several organic nanoplatforms, SPNPs with excellent optical property have gained immense popularity recently.[180–184] The large π-conjugated backbone and high electron-delocalized structure of SPNPs allow excellent light-amplifying and light-harvesting properties in the NIR region and therefore offer new opportunities especially in the field of imaging and phototherapy.[185, 186,187] Besides, other properties such as photostability, brightness, cytotoxicity, particle size, absorption and emission spectra are also largely responsible for the excellent PCE of SPNPs. So far, this may be attained by careful modification of backbone structures, selecting the right SPs during the process of fabrication, or *via* surface modification of SPNPs.[152] Several classes of polymers such as polyaniline (PANI),[188] polypyrrole (PPy),[35] PEDOT:PSS,[189] and conjugated donor-acceptor (D-A) structures[190] are extensively studied for the photothermal applications. Among these, polyanilines are the first of its type to be reported for the PTT of cancer. The molecular configuration of PANI allows a facile switch from emeraldine base (EB) to emeraldine salt (ES) in the presence of dopants such as transition metals, strong acids, alkali ions and Lewis acids.[191] This transition can induce significant red-shift in the optical absorbance peak (NIR range) *via* a change in the inter-band gap state between conduction and valence bands. Doped-PANI can therefore absorb incoming NIR light and generate a substantial amount of heat energy that can be used for cancer-cell ablation. In 2011, unlike the use of external dopants, Haam *et al.* reported the feasibility of using intrinsic biological dopants to induce PANI-triggered PTT in epithelial cancer.[192] Unlike normal cells, cancer cells are slightly acidic and are a rich source of oxidative species that can complement the dopants necessary for the protonation of PANI for effective PTT in tumours. So far, only a handful of PANI based purely organic nanostructures are available for PTT.[193] This may be due to the complexity in the modification of PANI that requires conductive materials such as Au, Ag to shift the transition from extremely low pH (<3) to a high pH environment mimicking TME. [194, 195] The SPNPs having higher absorbance and facile light-to-heat conversion ability are desirable for enhanced photothermal killing of cancer. Moreover, such NPs should also encompass better pharmacodynamics when injected *in vivo.* In 2012, Liu *et al.* fabricated a class of NIR-absorbing conducting polymer mixtures based on poly(3,4ethylenedioxythiophene):poly(4-styrenesulfonate) PEDOT:PSS for effective PTT. [196] After series of surface modification, the “stealth-like” PEGylated PEDOT:PSS NPs demonstrated high blood-circulation half-life of ~21 h resulting in excellent tumour accumulation and effective PTT *in vivo*. Since then, various multifunctional PEDOT:PSS NPs capable of delivering chemotherapeutic drugs and simultaneously performing PTT have been investigated for combination therapy.[189] Liu *et al.* reported the feasibility of PPy, also a

family of SPs that were previously used for optical coherence tomography (OCT),[197] as a potential candidate for the PTT of cancer.[198] The poly(vinyl alcohol) (PVA) stabilized PPy NPs having a smaller size (~60 nm) and absorption in the NIR-region was successfully utilized for PTT both *in vitro* and *in vivo*. Since then, PPy NPs having good photostability, biocompatibility, and high conductivity have emerged as a potent PTA in cancer theranostics. Dai *et al.* reported the fabrication of a uniform PPy NPs having excellent photothermal ability *in vitro* and later investigated the photothermal effect of PPy both *in vitro* and *in vivo* in a mouse tumour model.[35, 199] Compared to the PANI NPs, PPy demonstrated excellent PTT effect after exposure to an 808 nm laser (1.5 W cm^{-2} for 10 min) by spontaneous temperature rise (Δt = 20 °C) within 2 min *in vivo*, leading to complete ablation of tumours at 20 days post-therapy. Currently, the design of SPNPs has achieved remarkable progress for enhanced photothermal ablation of tumours. The emerging designs usually capitalize on facile energy transfer of excited photons that can be maximally channelized for the generation of heat. Herein, the diketopyrrolopyrrole (DPP) derivatives having high photostability and planar structure are gaining popularity. Because of a typically high electron-deficient core, these polymers can be successfully attached to an electron-donating substitute such as triphenylamine (TPA) resulting in a donor-acceptor–donor (D-A-D) topology (Figure 5a).[200] The modified D-A topology not only improved the semiconductive property but also enhanced the NIR-absorption essential for effective PTT (Figure 5b). Together with enhanced PTT, the biodegradability and biocompatibility of SPNPs should be carefully considered to meet the clinical requirement. Recently, Pu *et al.* proposed a promising theranostic SPNPs with excellent biodegradability and photothermal properties.[201] As SPs have vinylene bonds that can densely pack or coil within NPs, it is possible to increase the mass absorption coefficients thus enhance PCE/amplified PTT (Figure 5c-e). At present, this PCE (~71%) is the highest compared to the previously reported TBD-based SPs (68.1%) and many other inorganic NPs including Au and quantum dots.[202] Moreover, the enzymatic degradation of vinylene bonds in the presence of oxidative species (peroxidase) allowed facile degradation of SPNVs in the biological environment thereby eliminating the risk of long-term toxicity *in vivo* (Figure 5f). In addition to this, Tang *et al.* developed a photothermally stable and ROS resistant D-A organic NPs (ONPs) for the enhanced phototheranostic application (Figure 5g).[203] Importantly, highly quenched molecular topology in water as observed in the photoluminescence spectra at 1020 nm combined with highly efficient D-A structure that can facilitate facile intramolecular charge transfer (ICT) contributed for the ROS-resistant, reduced photobleaching, highly stable and maximized PCE of ONPs (Figure 5h-j). The summary of these molecules and their corresponding therapeutic activities are listed in Supplementary Table I.

3. Approaches to enhance photothermal treatment outcomes

The success of photothermal cancer therapy is related to many issues, including the use of appropriate radiation dosage, determining the best treatment time, and enhancing the PCE and tumour accumulation of the PTAs. The laser power intensity can influence the cell death mechanism after PTT and laser irradiation overdose may cause overheating and unnecessary damage to normal tissues.[32] Depending on the PTAs' structures and physical properties, their time-dependent accumulation in tumours after systemic administration vary from case

to case. Therefore, imaging techniques should be combined to determine the best time point for treatment. Also, laser light intensity attenuates significantly with the penetration depth, leading to a lower temperature rise of tumours buried deeper in the body.[204] Enhancing the PCE of PTAs and developing NIR-II PTAs can be beneficial to treat such tumours. Last, the concentration of PTAs in the tumours is critical for determining the PTT outcomes. Increasing the accumulation of PTAs in tumours results in more efficient treatment.

3–1. Controlling the appropriate laser dosage

In general, laser light with longer wavelength and stronger intensity has deeper penetration. However, it is important to apply appropriate laser dosage to achieve better PTT outcomes and avoid damage to normal tissues. Studies have shown that photothermal can trigger cell death through either necrosis or apoptosis, depending on the intensity of radiation.[32, 205] Fuente *et al.* has demonstrated that the PTT induced cell death pathway *via* necrosis or apoptosis can be controlled by adjusting the laser irradiation intensity.[205] More specifically, lower laser power density leads to a higher population of cells death from apoptosis and higher laser intensity usually causes necrosis. During necrosis, the cell membrane will be destabilized and broken, followed by the release of intracellular contents. The advantages of necrosis include the efficient and immediate killing of the cancer cells and receiving less resistance to PTT.[14, 32] However, necrosis may also impair the treatment outcomes by triggering pro-inflammatory responses and promoting tumour growth. On the contrary, the integrity of the cell membrane will be preserved during apoptosis. The process is characterized by cell shrinkage, oligonucleosomal fragmentation of nuclear DNA, swelling and leaky mitochondrial membrane, and chromatin condensation. Yet, due to the integrity of the cell membrane, the dying cells can be recognized and uptaken by phagocytic cells in a timely manner, decreasing the undesired inflammatory responses and enhancing treatment performances.[14, 32] The potential problem of photothermally induced apoptosis is that cells may develop resistance to the PTT similar to chemotherapy or radiotherapy. Considering the differences in biological responses due to the dissimilar cell death mechanisms, it is recommended to change the laser dosage for different applications or therapies.

In most of the PTT studies, thermal cameras have been used to monitor the temperature rise in the tumours to regulate the irradiation dosage and avoid overheating. However, this strategy is insufficient to provide temperature mapping for the entire tumour and avoid overheating for specific tumour regions. Thermal camera records the overall temperature of entire tumour tissues, which does not consider the nonuniform distribution of PTAs in tumours and attenuation of laser light with increasing penetration depth. Thus, it is difficult to completely avoid the damage to adjacent normal tissues during PTT caused by the overheating and massive heat transfer, especially for tissues located closer to the surfaces. New methods should be developed to provide extra regulation on the energy input from the laser. For this purpose, Zheng *et al.* developed the photothermal enhancing auto-regulated liposomes (PEARL) with photothermal feedback control function by introducing bacteriopheophorbide-lipid dye conjugates in a thermoresponsive lipid bilayer.[206] More specifically, the lipid-conjugated dyes initially formed J-aggregation in the liposomes, leading to strong light absorption and efficient temperature rise under laser irradiation. When the phase transition temperature of the thermoresponsive lipid bilayer is achieved upon laser

irradiation, the PCE of the PEARL decreased due to the disruption of the J-aggregation, preventing further temperature rise and avoiding potential overheating during PTT. Based on these automatic PEARLs, deeper and more homogeneous heating was achieved in a 3D polyacrylamide hydrogel model. In addition, more accurate temperature monitoring can be achieved by introducing nano thermal meters into PTAs, thus, providing better control over the laser dosage in PTT. For instance, Li *et al.* developed one type of PTAs with temperature monitoring function by wrapping core-shell upconversion NPs with a carbon-layer (csUCNP@C) (Figure 6a-c).[31] The localized temperature was reported by the temperature-dependent fluorescence signals of the UCNPs. The authors also designed a special set-up, which was able to measure the temperature of a macroscopic solution by a thermal probe and determine the microscopic temperature at the nanoscale with a spectrophotometer (Figure 6d). The PTAs made use of the relationship between the fluorescence ratio (525 nm to 545 nm) and a function of temperature to obtain the temperature changes at the nanoscale (Figure 6e). With the special set-up, they found that significantly higher eigen-temperature rises of csUCNP@C were obtained compared to macroscopic temperature rises in solution under laser irradiation at each time point (Figure 6f). Then through *in vitro* experiment, they found that the csUCNP@C internalized cancer cells could be killed under laser irradiation (5 min 0.3 W/cm^2) with the only 1.4 °C increase of the macroscopic temperature (Figure 6g). The fluorescence characterizations indicated an intracellular temperature rise of 23 °C for cancer cells with csUCNP@C internalized upon laser irradiation. But the cancer cells without csUCNP@C remained alive with 1.4 °C increase of the macroscopic temperature by external heating and were dead only when the macroscopic temperature increased by more than 3.6 °C (Figure 6g). In addition, the authors demonstrated that PTT with low laser intensity was able to kill cancer cells containing PTAs but leave adjacent cells without PTAs alive (Figure 6h-j). Based on this mechanism, the authors used lower power density laser to irradiate tumours for multiple times to achieve successful ablation of tumours. In short, the laser power density and temperature change profiles in PTT can determine the different cell death mechanisms, and eventually the final treatment outcomes. More work should be done to monitor and regulate the input of laser energy for improved therapeutic performances.

3–2. Determining the best treatment window

In many preclinical studies, the systemically administered PTAs go through the blood circulation system and accumulate in tumours through EPR effect. The pharmacokinetic behaviour of PTAs varies from each other, due to the differences in their physical properties. Usually, the treatment outcomes can be better if PTT is performed when PTAs reach the highest accumulation in tumours. PTAs having imaging modalities can monitor the accumulation of NPs in tumours in real-time after systemic administration and provide guidance to PTT, which is called imaging-guided therapy.[33, 207] Many imaging modalities, such as positron emission tomography (PET),[208–210] single photon emission computed tomography (SPECT),[211] MRI,[212–214] fluorescence imaging,[55, 215] afterglow luminescence imaging,[216] PAI,[217] ultrasound imaging,[27, 99, 218] OCT,[219] and CT,[220, 221] have been combined with PTAs to assist the conduction of therapies.[222] In some cases, multiple imaging modalities have been combined to provide more information for tumour diagnosis and therapy monitoring. In this section, we will summarize recent examples of how imaging techniques could be used to guide PTT for better treatment outcomes.

3–2-1. Fluorescence and afterglow luminescence imaging-guided PTT—

Fluorescence imaging refers to the collection and recording of optical signals emitted from any form of matter when illuminated by another light with a different wavelength. It offers high temporal-spatial resolution images and short imaging acquisition time. Compared to MRI or PET, which takes longer acquisition time or requires high-cost facilities, fluorescence imaging technique has certain advantages. However, the *in vivo* biomedical applications of fluorescence imaging is limited by the short penetration depths of both fluorescence excitation and emission and interference from the autofluorescence and strong light scattering of tissues in the UV-vis range.[215] This limitation triggered the development of fluorescence contrast agents in the NIR window, which not only improves its penetrating ability but also reduces the interference of the autofluorescence and scattering from the tissues, leading to the enhanced signal-to-noise ratio. Many small molecular fluorescent dyes, such as ICG, can generate both fluorescence and thermal effect under the laser irradiation, which makes them good choices for fluorescence imaging-guided PTT. Cai *et al.* synthesized cell membrane-camouflaged NPs containing ICG and poly(lactic-co-glycolic acid) (PLGA) in the core.[223, 224] After intravenous injection, the accumulation of NPs in tumours can be clearly observed from the NIR fluorescence imaging of ICG molecules under fluorescence microscope. The cell membrane cloaked NPs had excellent tumour accumulation and targeting effect, leading to complete regression of tumours under imaging-guided therapy. In another study reported by Zhang *et al.,* carbon-iron oxide hybrid NPs loaded with ICG were prepared.[225] Compared to free ICGs, the loading of ICG in the NPs improved its photostability due to the absorption of light by carbon NPs, leading to improved fluorescence and photothermal properties. The imaging-guided PTT was achieved in the *in vivo* experiment. More recently, fluorescence materials in the NIR-II window, such as SPNPs, quantum dots, and carbon nanotubes, have attracted great attention, due to the deeper penetration ability and lower background interference of NIR-II fluorescence imaging.[37, 55, 131, 215, 226] Chen *et al.* reported the fabrication of Ag_2S quantum dots with well-defined sizes and size-dependent fluorescence and photothermal properties.[131] The NPs of three different sizes of 4.1, 7.9, and 9.8 nm, were synthesized by using human serum proteins as templates and carefully adjusting feeding ratios of reactants (Figure 7a). Of three sizes, 9.8 nm Ag_2S quantum dots showed the strongest fluorescence peak at around 1060 nm and led to the largest temperature rise after being exposed to a 785 nm laser (Figure 7b-d). After injection, the NIR-II fluorescence signal in the tumour reached a peak at 24 h postinjection, indicating the best time for PTT (Figure 7e,f). Successful PTT outcomes were obtained by injecting Ag_2S quantum dots at a dose of 50.0 μmol kg^{-1} of Ag (Figure 7g).

Afterglow luminescence is another light emission phenomenon, in which the materials can continuously emit long-lasting luminescence even after the excitation has been removed. Compared to fluorescence imaging, afterglow luminescence is better to overcome the interference signals from background.[216, 227] Especially, materials having NIR afterglow luminescence and certain responsive functions can further decrease the signal-to-noise ratio for imaging. Yan *et al.* reported a responsive multifunctional nanoprobe by linking copper sulfide (CuS) NPs onto afterglow luminescent NPs through matrix metalloproteinases (MMPs)-cleavable peptide linkers (H_2N–GPLGVRGC–SH).[228] The core of afterglow luminescent NPs had a luminescence peak at around 695 nm after being illuminated by a

650 nm LED light. In the absence of MMP, the luminescence from the afterglow luminescent NPs was quenched by the adjacent CuS NPs. In TME, where MMPs were present, the cleavage of peptide linkers released the CuS NPs from the surfaces of afterglow luminescent NPs and restored the luminescence for tumour imaging. With the imaging signals, PTT was conducted by making use of the photothermal effect of the released CuS NPs.

Despite the progress on the development of fluorescence or luminescence probes for PTT guidance, the penetration depth is still a limitation compared to other imaging techniques, such as MRI or PET. Furthermore, NIR fluorescent NPs usually have low quantum yields and provide limited fluorescence signals. More work should be done to solve these problems.

3–2-2. PET or SPECT imaging-guided PTT—PTAs with nuclear imaging functions, such as PET and SPECT, enable deeper imaging of tissues or disease sites than fluorescence imaging. Both PET and SPECT detect radioactive signals from radioisotopes to provide the imaging information. While SPECT detects the single gamma ray from each decay, PET detects the photons formed after the annihilation of two oppositely charged intermediate positronium. PET is mainly used for cancer detection due to its ability to reveal changes of certain biological subject, such as biomolecule metabolism and expression of certain receptors. The pharmacokinetics of the PTAs can be monitored by these imaging techniques if radioisotopes have been stably labelled on PTAs with good radiochemical yields and unaltered surface chemistry of PTAs.[210, 229] Since most NPs have longer blood retention time than small molecules, radioisotopes with longer decay half-lives are preferred for tracking the NPs *in vivo*. For example, ^{64}Cu, ^{72}As, and ^{89}Zr have half-lives of 12.7, 26.0, and 78.4 h, respectively. The radioisotope labelling method can be divided into two groups, which are a chelator introducing method or a chelator free labelling method. The chelators bind with radioisotopes through coordination interactions and examples of chelators include 1,4,7,10-tetraazacyclododecane-1,4,7,10-tetraacetic acid (DOTA), 1,4,7-triazacyclononane-1,4,7-triacetic acid (NOTA), diethylene triamine pentaacetic acid (DTPA), and so on. For example, Chen *et al.* prepared perylene diimide NPs with different sizes for PTT, on which DOTA was introduced for ^{64}Cu labelling.[42] The PET imaging data revealed that the highest tumour uptake of 60 nm perylene diimide NPs occurred at 24 h postinjection, indicating the best time to make use of the photothermal properties of perylene diimide NPs for PTT. The chelator introducing method usually requires conjugation chemistry to introduce chelators and may suffer from unstable labelling due to the detachment of chelators or replacement of radiometals by other metal ions present *in vivo*.[229] As an alternative, many chelator-free labelling methods have been developed.[29, 132, 208, 209, 230–234] In a study by Li *et al.,* the researchers introduced ^{64}Cu during the synthesis of citrate-stabilized and PEGylated [^{64}Cu]CuS NPs.[230] To facilitate the labelling, the reactions were done under an elevated temperature condition to shorten the reaction time. The authors compared the pharmacokinetics of two types of CuS NPs through PET imaging and found that PEGylated [^{64}Cu]CuS NPs showed a longer circulation half-life and higher uptake in the tumour at 24 h postinjection. Finally, PTT function of PEGylated [^{64}Cu]CuS NPs was demonstrated. In another study, Chen *et al.* reported a chelator free

post-labelling method to chemically reduce ^{64}Cu on PEGylated Au NPs of different shapes and sizes (Figure 7h).[209] This labelling method was not only fast and efficient but also more stable than the labelling by DOTA chelators in the control group. The control group had stronger radioactive signals in the bladder at 1 h after injection due to the detachment of radiometals from chelators. The authors compared the tumour uptake of Au nanorods with and without RGD functional groups on the surfaces with this quantitative imaging technique and found that RGD targeting could enhance the tumour accumulation of Au nanorods. Finally, the authors used PET imaging of ^{64}Cu labelled PEGylated Au nanorods to guide the ablation of the tumour *via* PTT (Figure 7i-k). Besides ^{64}Cu, other radioisotopes have also been labelled using chelator free method. Cai *et al.* reported the labelling of mesoporous SiO_2 NPs with ^{89}Zr based on the interaction between ^{89}Zr and abundant adjacent deprotonated -Si-O^- groups in the pores.[231] In a later study from the same group, they combined this system with CuS NPs and meso-tetrakis(4-carboxyphenyl)porphyrin (TCPP) and realized the multimodal imaging-guided phototherapy.[232] In another example, Gao *et al.* reported the self-assembly of Fe^{3+} ions, gallic acid, and polyvinyl pyrrolidone (PVP) in aqueous solution through coordination interactions into stable ultra-small NPs with an average size of 2 nm.[211] The presence of a phenolic group of gallic acid enabled the labelling of ^{125}I to NPs through iodogen method. This labelling allowed the study of the pharmacokinetics of NPs through SPECT-CT imaging technique, and highest tumour uptake (5.3 %ID/g) was observed at 2.5 h postinjection due to the ultra-small size. Following this result, the successful photothermal ablation of tumours was conducted at 2.5 h postinjection. In short, through radiolabelling, PET and SPECT can monitor the distribution of NPs in organs or tumours and facilitate the PTT. The problem with PET imaging is the requirement for high-cost instruments. The instruments for SPECT are cheaper but produce images with relatively lower resolution. Both techniques require the handling of the radioactive materials, which may also limit their availability. PET and SPECT are usually combined with CT or MRI to provide more detailed anatomical information.

3–2-3. MRI-guided PTT—MRI is another real-time, non-invasive, and high-resolution imaging technique that can acquire anatomic images from deep tissues or organs in the body. The combination of MRI probes with PTAs can realize the MRI guided PTT.[208, 212–214, 235–241] The MRI probes can be divided into two groups, which are T_2-weighted and T_1-weighted MRI contrast agents. T_2-weighted MRI contrast agents change the transverse relaxivity (r_2) and lead to darkening of images. On the contrary, T_1-weighted MRI contrast agents change the longitudinal relaxivity (r_1) and enhance the brightness of the images. Superparamagnetic iron oxide (Fe_3O_4) NPs are traditional T_2-weighted contrast agents, of which the r_2 values are related to their sizes and aggregation states. For example, Nie *et al.* reported the co-assembly of Fe_3O_4 NPs, polymer-tethered Au NPs, and free amphiphilic block copolymers into Janus hybrid vesicles.[214] In the vesicles, the assembly of Fe_3O_4 NPs and aggregation of Au NPs into half of the vesicles with enhanced plasmon coupling led to 4 times enhancement of r_2 values than individual Fe_3O_4 NPs and strong absorption in the NIR range, respectively. After intravenous injection, the accumulation of vesicles in tumours could be enhanced by applying an external magnet close to tumours and monitored through MRI and PAI. In another study by Chen *et al.* double-layered vesicles were prepared from dumbbell-shaped Janus amphiphilic Au-Fe_3O_4 NPs, which led to the

increase in r_2 values from 53 mM^{-1} s^{-1} to 193 or 295, or 405 mM^{-1} s^{-1} depending on the orientation of and coupling state of Au-Fe_3O_4 NPs in the vesicle membranes.[213] Due to the coupling between Au domains of its building blocks, the vesicles also showed NIR absorption. After injection, significant tumour darkening was observed. These platforms can potentially be used for PTT, which were proved from their excellent PAI performances. The development in synthesis has enabled the access to magnetic NPs other than superparamagnetic Fe_3O_4 NPs. In a recent study, Hou *et al.* reported the synthesis of 12 nm Au–Fe_2C Janus NPs with a r_2 value of 210.6 mM^{-1} s^{-1}, which is higher than that of 14 nm superparamagnetic Fe_2C NPs and Au-Fe_3O_4 NPs and commercially available T_2-weighted MRI contrast agent, Resovist (174 mM^{-1} s^{-1}).[239] Due to the presence of Au and Fe, the NPs had a broad absorption including the NIR range. The authors found that Au–Fe_2C NPs modified by affibody proteins ($Z_{HER2:342}$), which bound to HER2 receptors on MDA-MB-231 cells, showed better tumour uptake compared with PEGylated Au–Fe_2C NPs. The time-dependent T_2-weighted MRI results were used to guide the conduction of PTT to remove the tumours.

Currently, the clinical translation of T_2-weighted contrast agents has been unsuccessful, mainly due to some limitations of T_2-weighted contrast agents. For example, the T_2-weighted contrast agents decrease the brightness of images, which is not preferred for observation. The T_1-weighted contrast agents have attracted intense research interest recently, as they can increase the sensitivity of MRI by making the images brighter.[235] For example, gadolinium (Gd)–chelator complexes, and other metal ions like Mn(II) have been frequently studied.[208, 237] Gd–chelator complexes have been used in the clinic, even though it has low longitudinal relaxivity and some toxic effect. Efforts have been made to improve the performance of Gd–chelator complexes.[242] For example, Marangoni reported that encapsulation of Gd–chelator complexes in the silica layer of Au core–silica layer–Au shell NPs increased r_1 from 3 mM^{-1} s^{-1} to 24 mM^{-1} s^{-1} characterized by a 4.7 T MRI scanner.[230] The NIR absorption of Au core–silica layer–Au shell NPs due to the coupling between Au core and shell indicated the potential PTT applications of the NPs. In another example, Chen *et al.* developed core–satellite NPs with the core of Dox-loaded polydopamine (PDA) and satellites of Gd-metallofullerene. Each metallofullerene contained three Gd ions in one-carbon cage.[208] The encapsulation of Gd ions in metallofullerene led to enhanced r_1 and lower toxic Gd ions release. Determined by MRI and other imaging modalities, the best time to perform PTT was at 24 h post injection. Other ions have also been demonstrated as MRI imaging contrast agents to assist PTT. Feng *et al.* made use of the coordination between metal ions and tannic acid to form a shell outside the NP templates, such as PLGA polymeric nanospheres and nanovesicles and mesoporous SiO_2 NPs (Figure 8a).[237] Interestingly, when Fe^{III}, V^{III}, and Ru^{III} were used, the obtained NPs showed good photothermal effect with the PCE of 40%. The polymer NP@ Fe^{III}/tannic acid shell had an r_1 of 4.19 mM^{-1} s^{-1}. Introducing Mn^{II} into polymer NP@ Fe^{III}/tannic acid led to 6 times increase of r_2. The polymer NP@ Fe^{III} Mn^{II} /tannic acid could serve as both T_2-weighted and T_1-weighted contrast agents. In addition, the polymer NP@metal ion/tannic acid shells could be used for PAI or NIR fluorescence imaging with Cy5.5 encapsulated. After intravenous injection of polymer NP@ Fe^{III}/tannic acid NPs, the highest brightness of tumour area was observed at 4 h postinjection (Figure 8b). The MRI results were consistent

with results from other imaging modalities. Because of the imaging results, PTT was also conducted at 4 h postinjection, leading to significant temperature rise compared to the control groups (Figure 8c). Recently, fluorine-19 (^{19}F) MRI has attracted intense attention because it can provide a better signal-to-noise ratio than ^{1}H MRI, owing to the high background signal of ^{1}H MRI from water in the body. Wang *et al.* reported the synthesis of Cu_7S_4-Au NPs stabilized by polymers with absorption in the NIR window (800–900 nm) (Figure 8d-f).[241] The absorption of Cu_7S_4-Au NPs in this range was achieved by coupling the LSPR between Au and Cu_7S_4 NPs. ^{19}F was grafted to the polymers on the surfaces of NPs. Before injection, no background signals from ^{19}F labelled NPs was observed in tumour. After injection, a very bright MRI signal from ^{19}F labelled NPs was seen (Figure 8g). Better PTT outcomes with Cu_7S_4-Au NPs were demonstrated than the PBS control (Figure 8h,i).

Other imaging techniques, such as OCT, ultrasound imaging or CT, have also been used to guide the PTT.[27, 99, 218, 219, 243–245] Each imaging technique has its own pros and cons. For example, MRI is mainly used for soft tissues, but its resolution is lower than CT. The combining of multiple imaging modalities into one PTA system can provide more detailed information regarding tumour and lead to a better plan for PTT.

3–3. Enhancing PTT outcomes by NIR-II PTAs.

Recently, photothermal conversion from the second NIR window (NIR-II) (1000–1350 nm) has attracted much attention for biological applications.[37–39, 127, 246–249] The merits of NIR-II in biological applications are their deeper penetration than commonly used NIR-I laser and larger maximum permissible exposure (MPE).[40, 127] Potentially, conducting PTT in the NIR-II window can treat tumours deeper in bodies and improve treatment outcomes. This advantage has promoted the development of PTAs with absorption in the NIR-II window. For example, plasmonic NPs with absorption in the NIR-II window have been developed, due to their flexible LSPR depending on the structures. In many cases, the NIR-II absorption has been achieved by generating strong plasmonic coupling within nanostructures.[41, 246, 250] Duan *et al.* developed compact plasmonic blackbodies with many branches through a simple seedless and surfactant-free method by mixing dopamine and Au precursors (Figure 9a).[246] Due to the strong plasmonic coupling between Au branches within nanostructures (Figure 9b), the plasmonic blackbodies had broad absorption from 400 to 1350 nm. The PCE of such nanostructures irradiated by a 1064 nm laser was determined to be 80.8%, which was comparable to that irradiated by an 808 nm laser (88.6%). By covering samples with a piece of 10 mm chicken breast to mimic the light attenuation by the interference of tissues, photothermal effects from NIR-I and NIR-II lasers were evaluated. The irradiation of blackbodies solution by a 1064 nm laser at 1.0 W/cm^2 for 15 min reached a final solution temperature of 3.2 °C higher than that of solution irradiated by an 808 laser. Though this temperature rise is not sufficient to improve the PTT significantly, the 1064 nm laser had a higher MPE than the 808 nm laser and allowed higher laser dosage for 1064 nm laser in PTT, which could improve PTT outcomes. Then, an *in vivo* PTT with both 808 and 1064 nm lasers was conducted on 4T1 tumour-bearing mice with the tumours covered by 5 mm tissues (Figure 9c). At the MPE dose, the temperature rise in tumours resulted from the photothermal effect of blackbodies *via* the illumination of a 1064 nm laser was significantly

higher than that from an 808 nm laser (Figure 9d), leading to improved PTT outcomes (Figure 9e). The results demonstrated the advantage of using NIR-II lasers for PTT. Besides plasmonic NPs, other inorganic PTAs, such as Nb_2C, have also been developed.[127]

In addition to inorganic PTAs, organic PTAs with NIR-II absorption has also been investigated in PTT. To this end, Pu *et al.* have reported the synthesis of organic PTAs semiconducting polymer NPs ($SPNP_{I-II}$) having dual absorption peaks in the NIR-I and II windows for cancer PTT.[248] The synthesis of SPNPs based on poly[(diketopyrrolopyrrole-alt-cyclopentadithiophene)-ran(diketopyrrolopyrrole-alt-thiadiazoloquinoxaline)] (PDCDT) was thoroughly optimized by controlling feed ratio of three monomers. At a molar ratio of 2:1:1, PTAs with nearly identical dual absorption peaks at 1064 and 808 nm were obtained. The optimized PDCDT SPNPs were subsequently transformed into water-soluble copolymers *via* nanoprecipitation with amphiphilic triblock copolymers (PEG-b-PPG-b-PEG). Despite similar PCE of $SPNP_{I-II}$, elevated temperature (58.0 °C) was much more obvious for NPs irradiated with 1064 nm laser even at the depth of 5 mm. Such a high penetration ability of NIR-II absorbing SPNPs optimized within MPE dose (1 W cm^{-2} for 1064 nm, t = 10 min) eventually led to better antitumour efficacy in a xenograft model. In stark contrast to this, optimized 808 nm laser dose within MPE did not show adequate temperature increase required to trigger cell apoptosis.

3–4. Enhancing PCE of PTAs through NP engineering

The ability of PTAs to transduce energy from light to heat is described by PCE. In most cases, the light energy can only be partially converted into heat, with the presence of other competing energy conversion pathways. Upon illumination, PTAs can both absorb and scatter the light, and the sum of the two is called light extinction (Figure 10a,b).[251, 252] For plasmonic PTAs, their absorption, scattering, and extinction coefficient can be obtained from theoretical simulation or experimental studies, which are related to NP size, shape, and composition.[251, 252] Only the energy from absorption can be partially converted into heat. Thus, the enhancement of PCE can be achieved by increasing the absorption and decreasing the scattering of PTAs.[14, 36, 253, 254] Furthermore, the excited electron of PTAs by absorbed light may relax and release energy through both nonradiative and radiative decay pathways, in which the former one induces heat generation and the latter one leads to luminescence emission.[55, 216] For example, the impingement of photons to small molecular chromophores usually results in the excitation of an electron from its ground state (S0) to a higher energy state (S1) followed by subsequent relaxation to the lowest excited state *via* internal conversion. The relaxed molecules in the lowest vibrational level of the excited state can undergo one of the three processes, (i) return to the ground state by emitting photon (known as fluorescence), (ii) follow non-radiative relaxation pathways (heat generation), or (iii) exit from singlet to triplet state (T1) *via* intersystem crossing (known as phosphorescence) (Figure 10c).[152] Therefore, to improve PCE, PTAs should be carefully designed to increase light absorption, decrease light scattering, and promote the energy conversion through nonradiative decay.

3–4-1. Enhancing light absorption—The PCE of PTAs is directly related to their ability to absorb light, which can be defined by the molar absorption coefficient.[251]

Engineering NP structure for stronger absorption coefficient is beneficial for improved PCE. For plasmonic NPs, their absorption will be significantly enhanced when the illumination light is the same as their LSPR peaks. Because of the preference for NIR light in PTT, different methods have been investigated to obtain NIR absorbing plasmonic NPs. On the one hand, with the development of synthetic techniques, many plasmonic structures, such as Au nanoshells, Au nanocages, Au nanorods, Ag nanodisks, have been prepared with their LSPR peaks tuned to desired wavelengths.[43, 80, 94, 98] On the other hand, self-assembly of plasmonic NPs have also been intensively studied, which induces the shift of the absorption to NIR range *via* plasmon coupling.[95] Plasmonic assemblies with different nanostructures such as clusters and vesicles have been prepared through different assembly strategies to obtain the strong absorption in the NIR range.[95–97, 255] For instance, Nie *et al.* assembled 40 nm Au NPs with amphiphilic block copolymer ligands into vesicles which generated stronger coupling between Au NPs than vesicles made from smaller Au NPs and led to strong absorption in the NIR range.[97] Nie *et al.* controlled the block copolymer density on Au NPs and generated much stronger coupling between 15 nm Au NPs when they assembled into vesicles. The obtained vesicles showed good PAI enhancement due to their photothermal properties.[95]

In addition to tuning the plasmon wavelength, some reports have shown that plasmon coupling can enhance the absorption of PTAs. Joshi *et al.* compared the PCE of Au nanomatryoshkas and Au nanoshells and found that the nanomatryoshkas had higher PCE (63%) than that of nanoshell (39%).[256] The Au nanoshell is composed of a SiO_2 core and an Au shell. In the Au nanomatryoshka, the SiO_2 core was changed to an Au NP@SiO_2 hybrid core structure, thus leading to additional coupling between the Au core and the Au shell. The absorption of both structures was tuned to around 800 nm for comparison. The calculated results indicated that the absorption cross-section in a nanomatryoshka is ~1.3 fold larger than a nanoshell, which explained the higher PCE of Au nanomatryoshka. Duan *et al.* developed the hyperbranched blackbody plasmonic NPs with strong intraparticle coupling. Their simulated results indicated that absorption contributed to 98.5% of total extinction.[246] In another example, Yan *et al.* developed a type of porous Pd NPs, which showed higher PCE than Pd nanocubes.[257] Neither of the Pd nanostructures had obvious absorption peaks in the NIR range, but the porous Pd NPs showed stronger absorption throughout the entire NIR range.

The absorption cross-sections of plasmonic PTAs are also related to their shapes. Xia *et al.* reported the comparison of PCE of Au nanohexapods, Au nanorods, and Au nanocages.[258] Among them, Au nanocages showed the highest PCE per Au atom, followed by nanohexapods and nanorods. Considering that the three samples had the same extinction of 1.0 at 805 nm, their different absorptions should be contributed to the variation in PCE. However, due to the inconsistent experimental conditions and results, it is hard to conclude what shape of plasmonic structures would show the strongest absorption cross section and highest PCE.[14]

In addition, the absorption of PTAs can be enhanced through hybridization with other materials. Kohane *et al.* reported that hybridization of Au nanoshells or Au nanorods with reduced graphene oxide can enhance the PCE.[259] As we introduced in the previous section,

though reduced graphene oxide has a photothermal effect, the lack of absorption peak in the NIR range makes it an imperfect PTA. The hybridized Au nanoshells or Au nanorods on reduced graphene oxide served as local nanoantennae to increase the optical absorption at their LSPR peaks. As a result, the higher temperature rise of the solution under laser irradiation was achieved by the hybridized NPs compared to Au NPs or reduced graphene oxide alone. More recently, Chen *et al.* made a carbon nanotube ring coated with Au NPs (CNTR@Au NPs) by reducing Au precursors on CNTR surface assisted by the surface attached redox-active polymers.[260] The obtained nanostructures had enhanced absorption and PCE, because of the existence of the complex coupling modes, such as coupling between CNTR with Au nanostructures and coupling between Au NPs.

The absorption of organic PTAs such as SPs having conjugated structures can also be increased by engineering the nanostructures. For example, absorption coefficients and electron charge transfer of SPNP can be enhanced by tailoring the CP structures to improve the D-A strength. Recently, Liu *et al.* reported a comparative study on the PCE of three different water-dispersible CPNPs having D-A strength in the order of CP_1<CP_2<CP_3.[261] The order of the D-A strength and the mass absorption coefficients matched quite well with the corresponding photothermal efficiency, *i.e.* the CP_3NPs had the highest photothermal activity compared to CP_1 and CP_2 NPs. In addition, the CP_3 NPs further revealed the lowest IC_{50} value of 0.88 μg/mL in U87 glioma cells at 808 nm laser irradiation (0.8 W/cm^2, 5 min) indicating excellent PTT *in vitro*. *In vivo* study in a U87 xenograft mouse model showed complete tumour elimination with a 100% survival rate and no tumour recurrence until 30 days. In brief, the absorption of NIR light and subsequent conversion of light energy to heat is closely related to the absorption coefficients of the NPs.

3–4-2. Decreasing light scattering—Within the extinction of light, the scattered light usually does not contribute to the generation of heat. Thus, the decrease of scattering part of light can improve the PCE. It has been shown that the degree of light scattering increases with the volume of NPs.[36, 254] Wang *et al.* prepared three different sized Au nanorods and five different sized Au nanobipyramids with all of their longitudinal absorption peaks at around 800 nm.[36] Before the laser irradiation, the absorption at 808 nm for all NPs were adjusted to the same. After laser irradiation, NPs with larger volumes led to lower temperature rises of the solution, indicating decreased PCE for larger NPs. This was explained by the higher light energy consumption *via* light scattering specially in larger NPs. Therefore, smaller PTAs with similar structures would be more efficient in photothermal conversion. Yet, some exceptions also exist. For example, El-Sayed *et al.* reported that Au nanorods with median size AuNR (28 × 8 nm) showed better PCE than their larger (38 × 11 nm) or smaller counterparts (17 × 5 nm).[254] The lower PCE for the smallest Au nanorods may be due to their short decay of the field from the surfaces.

3–4-3. Promoting the energy conversion through nonradiative decay and intermolecular coupling—The light-material interaction is usually accompanied by the dissipation of energy *via* nonradiative or radiative decay pathways, in which the former one accounts for the light-to-thermal energy conversion. In this regard, promoting the conversion of energy through nonradiative decay pathway seems plausible to enhance PCE. However, it

requires in-depth knowledge of the various molecular interaction/photophysical processes such as photoinduced electron transfer, fluorescence resonance energy transfer (FRET), or exciton coupling.[152] Specifically, in light-based thermal therapies, this has been thoroughly met by modulating the photophysical processes and spatial interaction of chromophores when arranged in a nanostructure to achieve effective fluorescence quenching, reactive oxygen species (ROS)/singlet oxygen deactivation, and reduced photobleaching.[262, 263] Herein, we take account of various engineering strategies, for instance, synthesis of the D-A NPs, insertion of the light-harvesting unit, packing of PTAs in a close proximity and so on, that have been investigated thoroughly for improving the PCE in therapeutic applications both *in vitro* and *in vivo*.

The photoinduced electron transfer is basically realized by pairing a donor radical cation and acceptor radical anion within the same (intramolecular) or different molecules (intermolecular).[264] This normally requires careful alignment of the donor molecules having molecular orbitals higher than those of the dopants (acceptor). Such well-suited energy levels are highly conducive to facilitate energy transfer resulting in a highly quenched fluorescence and nonradiative channelization of energy after the light irradiation and have subsequently shown higher accountability for the amplification of PTT. In an example of small molecule-based PTAs, Zhao *et al.* chemically introduced a dimethylamine (DMA) unit (Donor) in the aza-BODIPY core (Acceptor) (obtained by substituting a nitrogen atom in the 8-position carbon atom of naïve BODIPY) resulting in the formation of a D-A pair and further solubilized with amphiphilic polymer, DSPE−mPEG$_{5000}$, to yield PEGylated-aza-BODIPY NPs (A1).[265] The facile intramolecular photoinduced electron transfer mechanism was successfully established between the aza-BODIPY and DMA unit contributing largely to the enhanced PCE *via* nonradiative decay of excited photons. Both theoretical calculation and steady-state and time-resolved photoluminescence (TRPL) spectra validated that the intramolecular photoinduced electron transfer mechanism can increase the probability of the excited photons to follow nonradiative decay path for enhanced photothermal conversion. The short TRLP decay rate of the A1 molecule (with DMA unit) was obvious compared to the control (without DMA unit). In contrast to the small molecules, additional efforts are placed to understand the molecular chemistry of SPNPs that are primarily involved in improving the PCE. Recently, Pu *et al.* have proposed an intraparticle molecular orbital engineering approach to enhance both imaging (PAI) and therapeutic (PTT) ability of SPNPs in living mice.[266] The simple and facile design strategy incorporating D-A type SPs and an electron-withdrawing carbon dot (fullerene: PC70BM) having energy level ideally suited in the range to favour photoinduced electron transfer could effectively result in complete fluorescence quenching and conversely promote heat generation after irradiation of laser (Figure 11a). This was mainly achieved by careful optimization in the amount of dopant necessary to quench the fluorescence of SPNPs at different doping ratios (Figure 11b). The final concentration of 20 w/w% PC70BM (dopant) was found to be the effective formulation in the preparation of SPNPs. In comparison to the non-doped SPNPs, the fluorescence quenched SPNP$_{20}$ demonstrated enhanced PA-brightness and increased PTT (48 to 62 °C) *in vivo* (Figure 11c,d). Indeed, D-A architecture comprising both small molecules or SPNPs have found overwhelming photothermal application recently and is still in the process of improvisation. For instance, Lee *et al.* reported a porphyrin–pyrene (light-harvesting unit)

functionalized D-A SPNPs [5,5′-dibromo4,4′-bis(2-octyldodecyl)-2,2′-bithiophene (D); 5,6-difluoro-4,7-bis[5-(trimethylstannyl) thiophen-2-yl]benzo-2,1,3-thiadiazole (A)] (PPor-PEG SPNPs) for enhanced PTT.[190] The functionalization of D-A structures *via* a light-harvesting unit showed excellent improvement in the PCE (62.3%) of SPNPs. In addition to a facile intramolecular charge transfer and effective fluorescence quenching after NP formation, the porphyrin–pyrene pendant further augmented the red light-absorbing capacity of PPor-PEG SPNPs for enhanced PTT.

In contrast to nonradiative decay, it is also possible for an excited chromophore (triplet state) to enter the intersystem crossing pathway which is responsible for the generation of ROS (Type-I PDT) or singlet oxygen (Type-II PDT).[267] For instance, small molecule agents such as porphyrin are well-documented to follow the aforementioned pathway for the generation of singlet oxygen instead of the nonradiative pathway. Therefore, effective design strategy to minimize intersystem crossing can ultimately reduce the generation of singlet oxygen but conversely maximizes the PCE. In an early attempt, Zheng *et al.* proposed direct insertion of Mn^{3+} ions to the porphysome structure resulting in improved photostability, minimum photobleaching and high photothermal efficiency over free-base porphysomes (Figure 11e).[268] The Mn-chelation into the porphyrin nanostructure greatly quenched the generation of ROS and activated PTT, presumably due to the increased probability of excited photons to follow nonradiative decay pathway (Figure 11f). The enhanced photostability was verified after irradiating metal-chelated porphysomes by 680 nm laser for 5 min where more than 95% of the Q-band absorbance was still maintained compared to free-base porphysomes (less than 20%). Importantly, over repeated irradiation Mn-porphysomes were still able to induce appreciable hyperthermia regardless of the disrupted or intact NP structure. It is therefore possible to quench the porphyrins photochemistry intramolecularly *via* metal chelation and activate PTT mode, irrespective of the integrity of the supramolecular assembly. Unfortunately, singlet oxygen quenching solely by molecular engineering of PS is relatively complex and very least explored. Therefore, an alternative mechanism such as FRET is also reported to minimize the singlet oxygen generation of a PS.[269] In general, the small molecules in very close proximity to the PS packed together in a nanostructure can smartly convert the incoming NIRF energy to heat instead of singlet oxygen *via* FRET mechanism.[270] The maximum benefit of such mechanism has been pursued in the design of synergistic combination therapy such as PTT/PDT.[271]

The photophysical processes in small molecules can also be revisited by engineering their spatial arrangements within a nanostructure. As such, NPs can harness the advantage of higher drug loading to accommodate many individual chromophores within each particle resulting in a highly quenched molecular state *via* strong π-stacking, such as J-type or H-type aggregates.[272] Kasha *et al.* observed that the higher concentration of the small molecules in an aqueous solution is often accompanied by the aggregation resulting in the bathochromic or hypsochromic absorption shift.[273, 274] This bathochromic shift was attributed mainly to the J-aggregates (head to tail stacking) while the hypsochromic shift to the H-aggregates (head to head). Such highly ordered molecular stacking is often reported as an effective strategy to reduce the rate of photobleaching, improve photostability, and promote nonradiative decay pathway by quenching fluorescence and ROS. In an example, Yan *et al.* demonstrated the fabrication of highly stable photothermal nanodots (PPP-NDs)

via peptide-modulated self-assembly of photoactive porphyrin (Figure 12a).[275] The self-assembled colloidal nanodots (~25 nm), unlike irregular porphyrin aggregates, showed broad and red-shifted absorption peak indicating strong π-stacking of tetraphenylporphyrin (TPP) (Figure 12b). Such strong π-stacking interactions (J-aggregates) in the assembled nanodots contributed mainly to the higher PCE especially by ROS inhibition and fluorescence quenching. The PPP-NDs revealed almost 99% quenching of singlet oxygen quantum yield *in vitro*. Similarly, Chen *et al.* further reported that J-type aggregates of Cypate inside silica nanochannels can dramatically enhance photothermal efficacy together with relatively less photobleaching compared to the free Cypate.[276] Moreover, these J-aggregates also worked as a protective shield to prevent the degradation of unsaturated bonds of Cypate by the ROS. In summary, all of these findings clearly indicate that the distribution of small molecules within a spatially limited compartment of nanostructures can induce J and H-type interactions that might have a potential role for effective PTT. However, detailed mechanism based on the individual conformation of J- or H-type aggregates for the enhanced PCE in photothermal applications, so far to our knowledge, has not been reported yet. The intermolecular coupling based (J- and H-type) photothermal applications are still in its infancy and demands more future work.

3–5. Increasing the tumour accumulation of PTAs

The key to successful PTT is to increase the delivery efficiency of PTAs in tumours and achieve sufficient tumour accumulation. Some researchers indicated that high concertation of Au nanorods in solution impaired temperature rise in the deep region of phantoms, due to the strong light absorption by Au nanorods at the top region of phantoms. But this can possibly be achieved *in vivo* only at exceptionally high injection dose of Au nanorods, which is beyond the scope of this discussion.[277] Generally, the accumulation of nanomaterials in tumours is based on EPR effect, which is described by the enhanced penetration of NPs into tumours through abnormal tumour blood vessels with leaky cell-to-cell junctions and extended retention of NPs in tumours due to the impaired lymphatic systems.[23, 26] However, systemically administered NPs would encounter many biological barriers before they reach the target and participate in PTT. These barriers include clearance by mononuclear phagocyte system (MPS), penetrating blood vessels into tumours, resistance for NPs diffusion in tumours, and expelling of NPs from tumours due to the elevated intratumoural pressure.[278] Many strategies have been investigated to improve the delivery of PTAs in tumours, which include changing the coatings or protecting layers outside NPs, introducing targeting ligands to NPs, optimizing the NP size and shape,[42–46, 279, 280] offering PTAs with responsiveness,[281–293] modulating TME with NIR light or photothermal effect.[47, 294–298]

3–5-1. Changing the surface chemistry of PTAs for enhanced tumour accumulation—

The interface between NPs and biological systems is where a complicated set of interactions acts together to determine the *in vivo* fate of NPs.[299] The surface chemistry of NPs, including charge, ligands, and coating, is the first part to interact with biological systems. Usually neutral or slightly negatively charged NPs have longer circulation time. The surface coatings of NPs are essential to maintain the dispersity and stability of NPs in a biological medium and prevent NPs from protein adsorption and

clearance by MPS. All these factors contribute to the enhanced tumour uptake of NPs. The most commonly used stabilizing ligands for NPs is PEG. The PEG can provide steric hindrance to NPs in order to maintain their dispersity in a biological environment. PTAs such as Au NPs, MoS_2, graphene oxide, SP micelles, and many others, stabilized by PEG have demonstrated good photothermal outcomes.[43, 120, 124] Without proper stabilizing ligands, NPs may easily aggregate due to the screened electrostatic repulsion forces in a biological environment with high ionic strength. Both PEG densities and lengths can affect the blood circulation and biodistribution of PTAs, which is believed to be related to the antifouling property of PEG.[300, 301] Chan *et al.* systematically studied how variable PEG densities on different sized Au NPs would influence their protein adsorption and macrophage uptake. They found that when the PEG density was below 0.5 PEG/nm^2, the protein absorption and internalization of Au NPs by macrophages decreased as the PEG densities increased.[300] In a more recent study, Pu *et al.* reported the self-assembly of amphiphilic PEG containing poly(p-phenylenevinylene) (PPV) derivatives into NPs (SPPVN) (Figure 13a).[302] Compared to the NPs made by poly[2-methoxy-5-(2-ethylhexyloxy)-1,4-phenylenevinylene] (MEH-PPV) and amphiphilic triblock copolymer (PEG-b-PPG-b-PEG), the SPPVN had higher PEG densities, leading to their enhanced tumour uptake than MEH-PPV NPs. The afterglow luminescence from SPPVN generated higher signal-to-background ratios than fluorescence imaging, which obtained fast tumour imaging at 40 min postinjection and detected tumour metastasis as small as 1 mm^3. A lot of studies have shown that introducing PEG on NP surfaces can decrease or prevent the formation of protein corona on their surfaces due to the strong hydration on PEG.[301, 303] Some recent reports have indicated that instead of complete prevention of serum protein adsorption, the PEG ligands actually selectively suppress adsorption of certain proteins, such as immunoglobulins and complement factors, as well as enrich the adsorption of certain proteins, such as clusterin, both of which contribute to the “stealth effect” of PEG.[304] Besides PEG, other coatings such as zwitterionic ligands have also been used to provide PTAs with stability and antifouling properties.[287, 305–310] However, there is a dilemma regarding the use of PEG or zwitterionic ligands as the coating materials, as both interactions between NPs with MPS and cancer cells will be reduced due to the coatings. Therefore, other strategies are needed to selectively enhance PTAs’ interactions toward cancer cells.

Introducing targeting groups on PTAs can increase the cancer cell uptake efficiency of PTAs and promote the higher accumulation and longer retention of PTAs in tumours, and eventually minimize damage to normal cells and improve treatment performances.[24] The targeting groups make use of their specific affinity toward molecules or receptors that are overexpressed on the cancer cells or tissues, to enhance the interactions between PTAs and cancer cells or TME. The commonly used targeting groups include antibodies, peptides, nucleic acids, polysaccharides, and small molecules.[11] In the presence of targeting groups, the cell uptake efficiency of PTAs is significantly increased. For example, Yang *et al.* reported using small peptide targeting groups, arginine-glycine-aspartic acid (RGD), to enhance the uptake of Ti_3C_2@mesoporos SiO_2 NPs by interacting with the $\alpha_v\beta_3$ receptors expressed on HCC cell membranes, which showed higher uptake than PTAs stabilized by PEG observed from their fluorescence signals under confocal microscopy.[311] The

Ti_3C_2@mesoporos SiO_2 NPs were used as drug carriers for combination of PTT and chemotherapy. Wang *et al.* prepared one type of PTAs (PFOB@IR825-HA-CY5.5) by encapsulation of perfluorooctylbromide into hyaluronic acid (HA) NPs, which were conjugated with Cy5.5 and IR825 on the surface or in the core, respectively (Figure 13b). The obtained PTAs combined triple modal imaging and PTT functions.[312] The HA can bind to CD44 that are overexpressed on many types of cancer cell membranes. Their study indicated that NPs were internalized much more by HT-29 cancer cells than HUVEC normal cells after 1 h of incubation time. The surface conjugated Cy5.5, which was initially quenched by IR825, turned on the fluorescence after it was released from the HA backbones by reacting with hyaluronidases in tumours. The fluorescence imaging was used to guide the PTT with IR825 as PTAs to eliminate tumours. Furthermore, the interactions between NPs and cells can be further enhanced by introducing multiple types of targeting groups in a single PTA nanostructure. Tae *et al.* investigated the uptake of graphene oxide PTAs with both folate and cyclic-RGD targeting ligands by KB cells compared with PTAs with a single type of targeting ligands.[313] The folate and cyclic-RGD can bind to overexpressed folate and $\alpha_v\beta_3$ receptors, respectively. Both flow cytometry and confocal imaging results indicated that the dual-targeting PTAs showed 1.9- and 2.4-fold increased internalization by cells than PTAs with single cyclic-RGD or folate ligands, respectively. *In vivo* results showed that only the dual-targeting graphene oxide PTAs achieved the complete removal of tumours under the same laser irradiation condition.

Many studies have demonstrated that the enhanced cellular uptake of PTAs with targeting ligands can lead to higher tumour accumulation of PTAs and improved treatment performances. An overall 50 % increase in tumour accumulation of NPs with targeting ligands than their passive targeting counterparts has been reported from the analysis of previous data.[314] However, there are also some reports indicating that PTAs with targeting groups do not significantly change their tumour accumulation level compared with PTAs without targeting groups.[315] Chan *et al.* compared the tumour accumulation of different sized Au NPs (15, 30, 60, 100 nm) through active targeting and passive targeting. The NPs were conjugated with either PEG or PEG in conjunction with transferrin. An MDA-MB-435 orthotopic tumour model was used to evaluate their differences in tumour accumulation. Among four different sized Au NPs, only the 60 nm Au NPs with targeting ligands showed 5 times faster and about 2 times higher tumour uptake than NPs without targeting ligands on their surfaces. No significant difference was observed for other sized Au NPs. This discrepancy may be resulted from the short circulation half-lives of NPs and loss of binding ability of targeting ligands to receptors on cell membranes after the change of NPs' identity in *in vivo* environment, indicating the complexity of active targeting for enhanced tumour accumulation. In addition, the densities of targeting ligands on NP surfaces should be carefully adjusted to achieve both enhanced targeting efficiency and avoid potential destabilization of NPs, especially in a biological environment.

Recently, cell membrane camouflage, initiated by Zhang *et al.* has been developed as a new coating strategy for NPs and has attracted broad attention.[316, 317] The coating martials can be derived from cancer cells,[223, 318, 319] macrophage cells,[320, 321] red blood cells,[322–327] and so on. PTAs with such biologically derived coatings are evasive to immune systems and possess the intrinsic self-targeting ability, thus will be able to achieve long blood circulation

and cancer cell-selective targeting simultaneously.[328] For example, Liu *et al.* used cracked cancer cell membranes (CCCM) from Hela to encapsulate NPs made from Dox and ICG to prepare Dox NPs@ICG@CCC NPs (DICNPs) (Figure 13c).[318] The obtained DICNPs had high drug loading efficiency, excellent photothermal properties, and good tumour accumulation. *In vitro* experiments showed that the DICNPs had selectively higher uptake by Hela cells than other control cells, including COS7 cells, L929cells, HepG2 cells, and macrophage Raw 264.7 cells. Especially, the low uptake by macrophage cells demonstrated the advantages of cell membrane camouflage in selective targeting and "stealth effect". Due to the CCCM coating, the DICNPs had high stability and low premature drug release. Compared with the CCCM-free Dox NP@ICG NPs (DINPs), significantly higher fluorescence signals in tumours were observed for DICNPs after intravenous injection, which was the overall effect of less premature drug release and higher tumour uptake of DINPs. The ability of DICNPs to target Hela cells selectively was also evaluated in a mouse model with Hela and HepG2 tumours inoculated on the left and right hind limbs, respectively. After intravenous injection, the Hela tumours on the left hind limbs had higher fluorescence signal than that in HepG2 tumours. Finally, the DICNPs showed the best treatment performance in a combination therapy with PTT and chemotherapy. In another example, Liu *et al.* used a macrophage membrane to modify the surface of iron oxide NPs.[320] This coating not only endowed NPs with good immune evasion but also provided NPs with active targeting to breast cancer cells due to the cell-cell adhesion between macrophages and cancer cells. Finally, effective PTT was conducted to treat the breast cancer *in vivo.* Overall, cell membrane camouflage is a more advanced coating strategy, but production of cancer membrane may take certain efforts.

3–5-2. Engineering the sizes and shapes of PTAs for enhanced tumour accumulation—Both size and shape of PTAs can influence their circulation half-lives, biodistribution in different organs, and accumulation level in tumours, since they can influence many biological processes, such as cellular uptake, crossing blood vessels, diffusion in tumour tissues, and so on.[278] Through analysis of previously reported results, NPs with a hydrodynamic size smaller than 100 nm showed higher tumour accumulation.[314] NPs larger than 100 nm could be cleared from blood circulation rapidly by MPS organs like liver or spleen and compromised their uptake in tumours. Yet, NPs smaller than 5 nm may go through renal clearance pathway, which shortens their circulation time and decreases their accumulation in tumours.[278] For NPs between 5 and 100 nm, smaller NPs usually show faster accumulation and better diffusion in tumours. However, the fast accumulation does not necessarily lead to higher accumulation, as larger NPs stay in tumours for a longer period of time due to their better retention, while smaller NPs can be pushed back into blood vessels from tumour tissues more easily by high intratumoural pressure. The best NP size that balances high tumour accumulation and good diffusivity may vary from case to case. Regarding NP shapes, non-spherical NPs differ from their spherical counterparts in the interactions toward cell membrane, tumbling under the shear force of blood flow, and many other biophysical processes.[44] Many studies have shown that non-spherical NPs, especially rod-like or cylindrical NPs, demonstrated some advantages in tumour uptake than spherical NPs.[329] However, this conclusion is not solid as there are many factors influencing the *in*

vivo fate and contradictory results may be obtained. The conclusion would be even harder to make when both the size and shape of NPs are considered simultaneously.

In vitro experiment is helpful to understand the size and shape effect on cellular uptake in a simplified model. One aim to investigate the shape and size effect of NPs on cell uptake is to seek for the best structure that can enhance the tumour accumulation. As most NP sizes for *in vivo* studies lie in the range of 5 to 100 nm, NPs in this size range mainly enter the cells through endocytosis.[330] The endocytosis is a process integrating the adhesion energy between NPs and cell membrane through specific or non-specific interactions, membrane deformation against membrane tension, and the entropy penalty from clustering of receptors. The changing of NPs' sizes or shapes would influence these interactions and change their cellular uptake efficiency. In one study, Chan *et al.* investigated uptake of Au NPs with sizes of 14, 30, 50, 74, and 100 nm and Au nanorods with the length by the width of 40 × 14 nm and 74 × 14 nm in Hela cells.[331] The results indicated a strong relationship between the uptake efficiency of NPs and their shapes. Among different sizes, 50 nm Au NPs showing the highest cell uptake. The changing of shape from spherical NPs to rod-like NPs led to reduced cell uptake. The possible explanation is that non-specific protein adsorption on NPs dictated the endocytosis of NPs. Smaller NPs had fewer interactions toward cell membrane receptors while larger Au NPs or rods depleted the available receptors on membrane due to the larger contact area. Chu *et al.* compared the macrophage (RAW264.7) uptake of BSA-coated smaller (7 × 30 nm) and bigger Au nanorods (14 × 56 nm) with similar aspect ratios and found that smaller Au nanorods had higher macrophage uptake and better biocompatibility.[332] After observing this phenomenon, they injected Au nanorods containing macrophages intratumourally and made use of the better tumour penetration ability of macrophages in tumour hypoxic environment to enhance the diffusion of smaller Au nanorods in tumours. Compared to the injection of Au nanorods alone, more uniform heating and larger temperature increase were observed in tumours with the injection of Au nanorods containing macrophages upon laser irradiation.

The features of a good structure include decreased MPS clearance during circulation and enhanced uptake of NPs by cancer cells. To some extent, these two features may be contradictory to each other. The actual effect of size and shape has to be verified *in vivo.*[42, 43, 46, 279, 280, 333–335] Chen *et al.* assembled amphiphilic perylene diimide (PDI) derivatives into a series of PDI NPs with sizes of 30, 60, 100, and 200 nm and studied the size effect of NPs on tumour accumulation.[42] The NPs were labelled with ^{64}Cu and their tumour accumulation was monitored by PET imaging and PAI. Among different sizes, 60 nm PDI NPs showed the highest tumour uptake, with about 10.63 ± 1.54 %ID/g in the tumour at 24 h postinjection. The PDI NPs had excellent photothermal properties and were used in PTT. Chen *et al.* evaluated the size effect of Au nanorods on biodistribution and tumour accumulation.[279] The results indicated that smaller Au nanorods had longer blood circulation time due to their slower clearance by MPS organs. Yet, Au nanorods with longer aspect ratio demonstrated better tumour accumulation. The overall results indicated that the volume and aspect ratio, the two important features of Au nanorods, must be balanced for better tumour delivery. Xia *et al.* compared the biodistribution and tumour uptake of four different shaped Au nanostructures with similar diameters, which included Au nanospheres, nanodisks, nanorods, and cubic nanocages.[280] All nanostructures were labelled with ^{198}Au

and their biodistribution was monitored with the imaging signals from Cerenkov radiation. Their results demonstrated that Au nanospheres were the best in terms of tumour uptake, however, Au nanorods and Au nanocages had better diffusivity, leading to deeper penetration in the tumour area. More recently, Chen *et al.* compared the macrophage uptake of 2D Au nanostructures, including nanorings and nanoplates with Au nanospheres (Figure 14a-c).[43] Different Au nanostructures with or without preformed protein corona were incubated with macrophage cells (Raw 264.7) at 37 °C for 8 h, followed by the analysis of Au content being internalized by an inductively coupled plasma optical emission spectroscopy (ICP-OES). The macrophage uptake was the highest for Au nanoplates, followed by Au nanospheres and Au nanorings (Figure 14b). The results were explained by the reduced interactions to cell membrane due to the decreased contact area of NPs with the shapes changing from plate to ring. This explanation was evidenced by the similar trend for the uptake of different Au nanostructures by macrophages cells at 4 °C. Under this condition the NPs preferred to stick to the membrane of cells instead of being internalized through endocytosis (Figure 14c). The *in vivo* liver and tumour uptakes of Au nanorings, Au nanoplates, and Au nanosphere of 50 nm labelled with ^{64}Cu were then evaluated *via* PET imaging (Figure 14d).[43] Because of the lower macrophage uptake of Au nanorings, they had the longest blood circulation time and the lowest liver and spleen uptake, which led to the highest tumour accumulation (Figure 14e-g). The authors also evaluated the size effect of Au nanorings on tumour uptake by injecting 30, 50, and 130 nm Au nanorings. The largest Au nanorings were cleared from the blood circulation very rapidly. The 30 nm Au nanorings showed faster tumour accumulation but also shorter tumour retention than 50 nm Au nanorings. Therefore, 50 nm Au nanorings were the best for photothermal ablation of tumours due to their good accumulation in tumours and PCE.

To improve the accumulation of PTAs in tumours *via* controlling the coating or shape or size of NPs requires a deeper understanding of nano-bio interactions. Limited by our observation method, we can't obtain a full picture of how NPs interact with biological systems *in vivo*, which results in an insufficient understanding of the nano-bio interactions and sometimes may conflict the conclusions. More efforts and better observation techniques are still demanded for advancing our knowledge about nano-bio interactions.

3–5-3. Responding to TME for enhanced tumour accumulation of PTAs—In many cases, there is no single condition that can fit for every purpose. For example, larger NP size is good for tumour retention, but smaller NP size is good for tumour penetration. Developing "smart" nanomaterials that can change their physicochemical properties in different *in vivo* environments is a promising strategy to achieve high tumour accumulation and retention but with relatively good penetration at the same time. PTAs that can increase their sizes in response to the TME is one way to balance tumour retention and penetration. PTAs with initial relatively smaller size are good for blood circulation, penetrating leaky blood vessels into tumours, and diffusing into deep tumour regions. After entering tumours, the smart PTAs can intelligently aggregate to increase their sizes in response to certain intrinsic stimuli within TME in a time- and concentration-dependent manner. This allows the enhancement of tumour retention with improved tumour penetration ability than intrinsically large PTAs. One character of TME is the acidic pH, due to anaerobic glycolysis and hypoxia

conditions in the tumour.[336] This character can be used to trigger the aggregation of NPs in tumours by breaking the charge balance that stabilizes NPs. Ji *et al.* prepared 16 nm zwitterionic Au NPs stabilized by mix-charge ligands, 11-mercaptoundecanoic acid and (10-mercaptodecyl) trimethylammonium bromide.[287] The obtained zwitterionic NPs had several features: good stability in blood or normal pH conditions, capable of assembling into large aggregates with NIR absorption in acidic pH environment, enhanced uptake by cancer cells in the acidic environment, and preferred uptake by cancer cells than macrophages. Compared with Au NPs stabilized by PEG, the zwitterionic NPs had similar blood circulation time but about two-fold higher tumour uptake and much longer tumour retention. Because of higher tumour uptake and NIR absorption of assembled zwitterionic NPs, improved PTT treatment outcomes were obtained. The decreased charge repulsion due to pH change can also come from NPs themselves instead of stabilizing ligands. Shi *et al.* reported a Mo-based polyoxometalate (POM) clusters that can assemble under acidic environment into large aggregates, in which the electronic repulsion forces between NPs were significantly decreased due to the protonation of POM macroanions (Figure 15a).[284] The hydrogen bonding interactions would overcome the electronic repulsions to induce the aggregation of POM clusters in tumours. Moreover, the acidification and reduction environment in tumours can enhance their absorption at 808 nm, increasing the photothermally induced temperature rise of POM clusters (Figure 15b,c). The POM clusters had a hydrodynamic diameter of 1.8 nm, providing them renal clearance ability (Figure 15d). The POM clusters reached the highest uptake in tumours at 1 h postinjection. Despite of such small sizes, a significant amount of POM clusters remained in tumours for 2 days after injection, which was mainly attributed to the aggregation induced prolonged tumour retention time (Figure 15d). POM clusters efficiently removed tumours *via* PTT due to their acidic and reductive environment induced-enhancement of absorption at 808 nm (Figure 15e). The interactions between complementary DNA can also be used to assemble PTAs elicited by pH change. Tang *et al.* designed one type of nanomachine capable of aggregating in the acidic environment by making use of host-guest chemistry and pH responsiveness. Two groups of Au NPs around 20 nm diameter were stabilized by two complementary single-strand DNAs, respectively.[281] Each DNA sequence was terminated by a pyridine-2-imine group, which was capped by alpha-cyclodextrin (α-CD) under neutral pH initially. The α-CD prevented the hybridization of complementary DNAs to keep the two types of Au NPs separated. When these nanomachines entered tumour, α-CD caps would be released due to the acidic pH-triggered protonation of the pyridine-2-imine at the end of DNA ligands, restoring the hybridization interactions between complementary DNAs on two types of Au NPs to induce their aggregation. Compared to DNA-stabilized Au NPs without capped α-CD, the nanomachines showed enhanced tumour uptake and retention after intravenous injection and better PTT performances.

In addition to pH, some enzymes that are overexpressed in tumour region can also be used to trigger the aggregation of PTAs in tumours.[283, 285, 286] For example, Chen *et al.* reported an alkaline phosphatase (ALP) responsive system in which small micelles assembled from ICG and NapFFKYp (ALP-responsive peptide) would reassemble into long fibres due to the change of the amphiphilic balance after dephosphorylation of NapFFKYp.[286] Compared to free ICG which cleared from the body in 4 h, this strategy significantly increased the

retention of ICG in Hela and 4T1 tumours even at 48 h postinjection. The higher accumulation of ICG in the tumour region facilitated enhanced PTT outcome. Metalloproteinase-2 (MMP-2) is another type of enzyme that is overexpressed in many tumour types. Li *et al.* reported one type of MMP-2 responsive PTAs made by linking a mixture of two types of peptides, CPLGVRGDDRGD (peptide 1, MMP-2 cleavable) and CKKKLVFF (peptide 2, assembly motif) to 13 nm Au NPs (Au NPs@Pep1/Pep2), with a defined ratio through interactions between thiol groups in Cys and Au.[283] The peptide 2 can induce the aggregation of Au NPs by forming hydrogen bonds (Figure 15f). Under normal conditions, the monodispersity of Au NPs was maintained by the peptide 1 ligands. In the presence of MMP-2, the PLGVRGDD part of the peptide 1 was cleaved, leading to the destabilization and aggregation of Au NPs. As a result, the tumour accumulation of MMP-2 responsive PTAs increased 3 times compared to the control group with only peptide 1 on Au NPs (Ctrl 1) and control group with MMP-2 irresponsive peptide 1 and peptide 2 on Au NPs surfaces (Ctrl 2) (Figure 15g). The aggregation of Au NPs in tumour induced red-shift of their absorption to NIR range and improved the PTT efficiency in U87MG tumour model (Figure 15h).

PTAs that can intelligently switch its surface charge from neutral or negative to positive in TME is another promising way to enhance the accumulation and retention of PTAs in tumours.[288–293] Because of the intrinsic negative charge of cell membranes, PTAs with initial neutral or negative charges have weaker interactions toward both MPS or tumour cells, which usually results in longer blood circulation but also a short tumour retention time. Switching the surface charge of PTAs into positive in TME will enhance the interactions between PTAs and cancer cells, leading to higher tumour uptake and better tumour retention. The charge conversion can be achieved through protonation of functional groups, such as a primary or secondary amine.[290, 291] Chiu *et al.* reported the synthesis of charge-switchable drug delivery system by conjugating N-Acetyl histidine (NAcHis) modified D-α-tocopheryl polyethylene glycol 1000 onto ICG and Dox co-loaded PLGA NPs.[290] By changing the pH of the medium from 7.4 to 5.0, the surface charge of NPs shifted from negative to nearly neutral and then to positive, due to the gradual protonation of the imidazole groups. Compared to the control NPs with static negative charge, the charge-switchable NPs showed enhanced uptake by TRAMP-C1 cells and macrophages, due to the enhanced affinity of neutral or slightly positively charged NP surfaces to cell membranes. After intravenous injection, significantly stronger fluorescence signals of ICG delivered by charge-switchable NPs were observed in tumours than free ICG or ICG delivered by static negatively charged NPs. Moreover, the charge-switchable NPs showed enhanced tumour penetration than static negatively charged NPs, due to the combination of NPs' small sizes and higher uptake of charge-switchable NPs by tumour-associated macrophages. The PTT results indicated that the ICG/Dox co-loaded charge switchable NPs showed the most profound photothermally induced temperature rise in tumours under NIR laser irradiation.

The charge conversion can also be generated by exposing positively charged groups in an acidic environment *via* breakage of chemical bonds.[288, 289, 292] For example, in a study by Liu *et al.*, graphene oxide modified with PEG and 2,3-dimethylmaleic anhydride (DA) conjugated poly(allylamine hydrochloride) (PAH), was used to load and deliver Dox.[293] The tumour acidic pH environment would trigger the Dox release from graphene oxide as well as

the DA release from PAH to restore the positively charged surfaces. This led to enhanced tumour uptake of Dox delivered by graphene oxide than free Dox and improved PTT outcomes.

3–5-4. Enhancing the tumour delivery of PTAs through the photothermal effect—The laser irradiation can be selectively targeted at tumour regions and induce dramatic and fast temperature rise initially from PTAs to entire tumour regions. This highly targeted stimulus allows the selective modulation of the physicochemical properties of PTAs in tumour regions or the direct tuning of TME, to further augment the tumour delivery of PTAs.

The photothermally induced temperature rise, especially with sublethal dose, can modulate the TME to magnify the uptake of PTAs. The mild temperature rise can increase tumour vascular permeability, initiate recruitment for certain biomolecules or cells, and enable the improved diffusion of PTAs in tumours.[295, 297, 337, 338] The mild temperature rise, referred to 40–45 °C, is capable of enhancing tumour blood flow and oxygenation and increase vascular permeability.[294, 295, 337, 339, 340] Since PTAs travel through the leaky vessel wall into tumours, the increase in vascular permeability can enhance uptake of PTAs in tumours. In a study by Nie *et al.,* the authors demonstrated that the tumour accumulation of an Au nanoshell-coated mesoporous SiO_2 with surface-conjugated transferrin (Tf) was enhanced with the aid of NIR light irradiation.[294] Gemcitabine (GEM) was also encapsulated into the PTAs for a combination of chemotherapy and PTT. The tumours were irradiated by a laser for three times (0.5 W/cm^2, 1 min × 3 times, 1 min interval) at 24 h postinjection and the enhanced tumour uptake of PTAs with laser irradiation could be visualized by the stronger two-photon confocal microscopy imaging signals. Then the tumours were collected and analysed by an ICP to characterize the Au content in tumours. The results revealed that the tumour uptake of PTAs increased from 206 ± 28 ng/g to 377 ± 40 ng/g with the assistance of laser irradiation. In addition to mild temperature rise, the higher temperature rise caused by photothermal effect induces injuries in tumours, which can recruit certain biomolecules or cells to tumours. Based on this mechanism, researchers have designed some interesting strategies to enhance the tumour uptake of NPs. Bhatia *et al.* reported a very interesting NP communicating systems, in which Au nanorods disrupted blood vessels to activate the extrinsic coagulation pathway to recruit fibrins to tumours.[298] This can enhance the tumour accumulation of NPs coated with fibrin-targeting peptides. In another example, Liu *et al.* developed the Au nanorods encapsulated platelets (PLTs) PTAs through electroporation method (PLT-Au nanorod).[296] The PTAs with PLT coating can evade the phagocytosis by immune cells, which endowed the PTAs with a longer circulation half-life *in vivo* than Au nanorods and PLT membrane cloaked Au nanorods (PLT-M-Au nanorod) (Figure 16a). The PLT-Au nanorods inherited the properties of PLTs that can be attracted to the injury sites. A self-reinforcing feedback manner was used to enhance the delivery of PTAs by first intravenous injection of PTAs followed by irradiation of the tumour area with an 808 nm laser at 2 W/cm^{-2} for 5 min to cause injuries that recruited more PTAs to tumour area (Figure 16a). The quantitative results of the Au content in tumours *via* ICP measurement indicated higher accumulation of PLT-Au nanorods in tumours after subsequent doses of injections with laser irradiation than that of injection of PLT-Au nanorods without irradiation

of tumour regions (Figure 16c). As a result, a higher temperature rise after each time of PTT with the injection of PLT-Au nanorods was obtained than the control groups with Au nanorods or PLT-M-Au nanorods injection, leading to the improved PTT treatment outcomes with PLT-Au nanorods in a head and neck squamous cell carcinoma (HNSCC) tumour model (Figure 16d).

Furthermore, the diffusion of PTAs in tumours is hindered by resistance from collagen in tumour extracellular matrix (ECM), further limiting the delivery efficiency *in vivo.* The photothermal effect can also be used to decrease the resistance in tumours.[341, 342] Pu *et al.* constructed an SP/enzyme hybrid NPs by conjugating bromelain (Bro), a temperature-sensitive collagenase, to the surfaces of nano-assemblies of SP amphiphiles (PCB-Bro) (Figure 16e).[341] The Bro is supposed to have the highest activity in collagen digestion at a temperature around 45 °C, which is higher than the normal body temperature. Low dose laser irradiation (0.2 W/cm^2) at tumour for three times without exceeding the temperature above 43 °C after intravenous injection of PCB-Bros was sufficient to enhance the collagen digestion activity of Bro. The fluorescence signal from PCB-Bro NPs in tumours after injection with laser irradiation was 1.42 times higher than the control group with PCB NPs injected, indicating that improved tumour delivery was achieved by digestion of collagen in tumour ECM (Figure 16f). At 6 h postinjection, the PTT was conducted by exposing the tumours to an 808 nm laser at 0.3 W/cm^2, in which the group with digested tumour ECM showed the highest temperature rise and best treatment outcomes (Figure 16g).

Instead of modulating TME, photothermal treatment can serve as an external stimulus to modulate the physicochemical properties of PTAs in different environments. As we have discussed above, size-switchable properties can be beneficial for increasing tumour uptake of PTAs. This can be achieved by introducing thermal sensitive materials into PTAs. For instance, Poly(N-isopropylacrylamide) (PNIPAM) is a frequently used thermal sensitive material with low critical solution temperature (LCST). Chen *et al.* reported the synthesis of one type of core-shell nanocomposites with its core of Au nanorod@SiO_2 coated by a polymer shell of poly (NIPAM-co-acrylic acid).[47] The murine 4T1 tumour model was used to evaluate the tumour accumulation of PTAs. They found that increasing the temperature of the tumour area either by immersing the tumour in a water bath or laser irradiation can increase the uptake of PTAs in tumours. The tumour accumulation of PTAs increased by more than 7 times at 30 min postinjection when the tumour was exposed to the laser irradiation. This dramatical increase in tumour accumulation was explained by: first, the increased vascular permeability due to the photothermal effects of PTAs; and second, shrinkage of PTA sizes due to the thermally induced collapse of the PNIPAM. The laser irradiation induced temperature rise and enhanced accumulation of PTAs in tumour formed a feedback loop cycle, which explained the continuous temperature increase in the tumours without reaching a plateau during the PTT after injection of the nanocomposite.

4. Combining PTT with other therapies

Monotherapies are normally insufficient to trigger an adequate therapeutic response and PTT is not an exception. Even with great treatment efficacy, their limitation, such as insufficient light penetration depth, may cause the incomplete elimination of cancer cells, especially for

residual tumour cells at the treatment margins, leading to tumour recurrence and metastases in distant organs.[18] Combination of PTT and other therapies can improve the overall treatment results. In many cases, the combination of different therapies is not a simple addition. Instead, one therapy may benefit from the outcomes or effects of other therapies, achieving synergistic treatment outcomes.[48–53] One of the advantages that may apply to all combination therapies is to lower the dose of each therapy rather than individual therapies to achieve similar or even better outcomes. Besides this advantage, the efficient thermal generation in the desired location, one key feature of PTT, can improve the efficiency of combination therapy in different ways. As we introduced in the previous section, photothermal treatment can be used to enhance the accumulation and permeability of NPs or drug carriers in tumours. Furthermore, studies have indicated that PTT, depending on the laser dosage, can promote the cellular uptake of drug carriers, trigger the drug release from carriers in irradiation areas, overcome drug resistance, and inhibit DNA repairing, which would be favorable for any drug delivery involved therapy.[49, 343–346] In addition, PTT can increase the oxygen perfusion to change tumour hypoxia microenvironment, favoring oxygen-dependent therapies, such as PDT or radiotherapy.[339] The thermal ablation of tumour cells may also facilitate the combination of PTT with immunotherapy due to the release of tumour-specific antigens.[347] Therefore, the combination of PTT with other therapies has great potential to achieve the synergistic effect and improved treatment performances.

4–1. Combining PTT with chemotherapy

Uneven heating in different tumour regions has been frequently observed because of the nonuniform distribution of PTAs in a heterogeneous tumour and attenuated laser intensity at locations deeper from skins. This heterogeneous heating could result in incomplete elimination of cancer cells and tumour recurrence. Combining PTT with chemotherapy can be more effective in cancer treatment due to the synergistic effects and the ability to treat tumour metastases outside the scope of irradiation. The on-demand, controllable drug release is demanded in chemotherapies. Chemotherapeutics are loaded into drug carriers through different mechanisms, which include hydrophobic interactions, coordinating interactions, electronic interactions, hydrogen bonding, π-π interactions, chemical conjugation, and encapsulation of hydrophilic compounds. There is a balance between stable drug carriers for preventing premature drug release and fast drug release in tumours, for any drug delivery carrier. PTT has been demonstrated as an external stimulus to trigger the tumour-specific and spatiotemporal drug release. The drug release can be triggered by photothermally mediated disruption of drug carriers, the structure or conformation change due to the presence of thermally sensitive materials, cleavage of thermal responsive chemical bonds, or destabilization of the interactions between drug and carriers. In addition, the drug release rate can also be adjusted by manipulation of laser intensity. Depending on different drug loading strategies and desired drug release profiles, laser type, and dosage should be carefully controlled to promote demanded and efficient drug release. For example, Halas *et al.* compared the photothermally triggered drug release mechanism of the two different PTA drug delivery systems, which were Au nanoshells conjugated with double-stranded DNA and protein HSA, respectively, under the irradiation of a continuous wave (CW) or a pulsed laser.[346] Two drugs, docetaxel and HER2-targeted lapatinib, were loaded to PTAs through

the formation of a complex with DNA or binding to HSA. They found that the CW laser could increase the temperature around PTA to dehybridize double-stranded DNA due to the disruption of hydrogen bonds and trigger of drug release, while the pulsed laser could break the thiol-Au bond between DNA and Au surface but maintain the hybridized DNA structure, preventing the release of free drugs. In the case of HSA, both CW and pulsed lasers could trigger the release of the drug through either photothermal effect or denatured protein structure, respectively.

Chemotherapy frequently fails in the cancer treatment, because of poor pharmacokinetics and insufficient delivery of drugs, and most notably, development of multiple drug resistance (MDR) by cancer cells.[348] MDR may be derived from the deficient uptake of chemotherapeutic drugs by cells, increased drug efflux mediated by pump proteins, and expression of MDR-associated proteins.[49, 348–350] Photothermal treatment can potentially down-regulate the drug-efflux proteins to overcome the MDR for improved treatment. Chen *et al.* reported the assembly of Pt(IV) prodrug, cyanine dye (Cypate), and block copolymer containing PEG and decylamine-grafted poly(l-aspartic acid) (mPEG-*b*-PAsp) into micelle NPs (P/C-micelles) for combination of PTT and chemotherapy to overcome MDR of Pt(IV) prodrug (Figure 17a).[350] The authors first compared the uptake of Pt(IV) prodrug and Cypate by A549 and A549R cells, which were normal and cisplatin-resistant cells, respectively. Both cells showed similar uptake of Cypate, but the cisplatin-resistant cells only had about 50% uptake of Pt(IV) prodrug of that by normal A549 cells (Figure 17b). By using micelles as drug carriers, the uptake of Pt(IV) prodrug by A549R cells was significantly increased, with little differences compared to the uptake of Pt(IV) prodrug by A549 cells (Figure 17b). The efflux of Pt(IV) prodrug delivered by P/C-micelles from A549R cells also decreased compared with the efflux of free Pt(IV) prodrug (Figure 17c). These results indicated that the micelle structures can enhance the uptake of Pt(IV) prodrug by cisplatin-resistant cells. Then, a decreased IC50 of Pt(IV) prodrug for A549R from a value of 24.7 μg/mL for free drug, to 3.0 μg/mL of drug-containing micelles, and to 0.27 μg/mL of drug-containing micelles plus laser irradiation were obtained. Such lowered IC50 value is accompanied by the decreased resistance factors, which could be partially explained by the inhibition of MDR-associated protein 1 (MRP1) due to photothermal effect. The following *in vivo* study demonstrated that the combination of PTT and chemotherapy can eliminate the cisplatin-resistant tumour model. In another study from Zhao *et al.*, the authors prepared the NPs made by encapsulating MoS_2 with polyethylenimine (PEI) and HA (MoS_2-PEI-HA) to deliver Dox for the treatment of one type of drug-resistance tumour model, MCF-7-ADR.[349] The Western blot results indicated that through a mild photothermally induced hyperthermia, the expression of MDR P-glycoprotein (P-gp) can be downregulated. The HA could target at CD44 overexpressed cells to enhance the uptake of NPs. Together with the overcoming of chemotherapy drug resistance, the combination of PTT and chemotherapy dramatically decreased cell viability from around 50% to 2.9%. *In vivo* results demonstrated that about 96% inhibition ratio of MCF-7-ADR tumour model was achieved through a combination of PTT and chemotherapy by injection of Dox@ MoS_2-PEI-HA, which was much higher than the other control groups.

We have discussed that PTT can modulate TME to enhance the delivery of PTAs. The synergistic effects of combination of PTT and chemotherapy can also come from

photothermally mediated enhanced tumour accumulation and penetration of chemotherapeutic drug carriers for better treatment.[297] This enhancement can result from the increased blood flow and blood pressure in hyperthermia area, augmented NP extravasation from tumour vessels, enhanced diffusion in tumour interstitial matrix and cell uptake of chemotherapeutics.[47, 295, 339, 343] Yet, the desired temperatures for different enhancement mechanisms may not be the same. It has been reported that mild temperature rise between 40 to 42 °C is the favourable range of temperature to enhance liposome NPs extravasation from tumour blood vessels possibly owing to the formation of larger pores on blood vessels *via* the disaggregation of endothelial cell cytoskeleton and cell shrinkage.[337] The enhanced extravasation induced by the mild hyperthermia is not permanent. The blood vessels may return to the state before hyperthermia has been applied due to the development of vascular thermotolerance. Below 40 °C, the enhanced extravasation is not obvious, while temperature higher than 42 °C would cause haemorrhage and stasis in blood vessels and block extravasation of liposomes. It has also been reported that photothermal treatment can improve the transportation of NPs in tumour interstitial matrix. Raeesi and Chan *et al.* investigated the effect of photothermal treatment on the collagen structures using a collagen (I) μ-channel setup. They found that by introducing Au nanorods in the collagen channel and applying laser irradiation to increase the temperature to 45–55 °C, the transformation and denaturing of collagen fibres occurred, leading to the reduced resistance that prevented the diffusion of NPs.[338] As a result, in their model, the effective diffusivity of the 50 nm and 120 nm Au NPs increased for ~14 fold and ~21 fold, respectively, after the photothermal experiment. The results indicated that the diffusion of drug carriers in tumour ECM could be improved with the assistance of photothermal effect.

Although PTT can remove primary tumours efficiently, it can't eliminate residual cancer cells or treat tumour metastases outside the scope of laser irradiation. Combining PTT and chemotherapy can generate improved treatment outcomes.[351–355] In this context, Chen and co-workers developed the supramolecular micelles assembled from polyrotaxane building blocks as a theranostic platform.[351] The axle of polyrotaxane was amphiphilic PDI terminated block copolymer of PEG-b-poly(ε-caprolactone) (PCL), which formed host-guest complexation with the wheel of the primary-amino-containing β-cyclodextrin (β-CD-NH_2). Paclitaxel (PTX) was encapsulated in micelles during the self-assembly process. The PDI components provided the micelles with good photothermal properties. The presence of amines from β-CD-NH_2 enabled the crosslinking of micelle shell *via* reaction with N-hydroxysulfosuccinimide (NHS) ester-activated GSH-responsive crosslinkers (NHS-SS-NHS), forming "gatekeepers" that prevented the immature drug release during circulation. In the absence of GSH, only 6.27 % of PTX was released from micelles in 24 h. The much faster release rate was obtained in the presence of GSH and NIR laser irradiation, which was due to the removal of "gatekeepers' *via* cleavage of disulfide bonds in crosslinkers and destabilization of micelle structures through photothermal effect (Figure 17d). *In vitro* results indicated the synergetic effect on cancer treatment which was achieved through the combination therapies using these NPs. Owing to the good tumour accumulation and on-demand drug release, the supramolecular micelles, in a single-dose injection, could efficiently treat Hela tumour model through a combination of PTT and chemotherapy without any recurrence. All other control groups had tumour recurrence after the treatment.

The combination therapy by the supramolecular micelles was also evaluated in an orthotopic 4T1 tumour model. The treatment results indicated that a combination of PTT and chemotherapy led to better antimetastatic activity by suppressing the growth of surface lung metastases (Figure 17e,f) . In another study, Zhang and co-authors simultaneously loaded Dox and cisplatin onto polymer modified single walled carbon nanohorns (SWNHs) as a chemo-photothermal theranostic system.[352] Both synergistic effect of Dox and cisplatin and chemotherapy and PTT improved *in vitro* treatment of 4T1 cancer cells. *In vivo* study showed that combination of PTT and chemotherapy had the best treatment outcomes. Even though PTT alone effectively removed the primary tumour, the survival rate of mice in this group was similar to mice treated with PBS or SWNHs only. The *ex vivo* fluorescence imaging of tumour metastases indicated that the SWNH theranostic system could deliver chemotherapy drugs to tumour metastases, leading to prolonged survival rate by combining with PTT. In short, PTT can trigger the drug release, enhance the drug carrier accumulation and diffusion in tumours, overcome the MDR, and elicit strong efficacy in treating tumours.

4–2. Combining PTT with immunotherapy

Recently, immunotherapy, based on the patients' own immune systems to fight cancers, can potentially become a safer and more effective therapy than other traditional therapies. Tumours have certain immune suppression mechanism that protects them from being attacked by the body's immune system. To stimulate the immunotherapy, strategies such as checkpoint-blockade therapy, adoptive T-cell transfer especially the emerging chimeric antigen receptor T (CAR-T), and utilization of cancer vaccines, have been applied.[6, 7] Especially, the development of cancer vaccines with tumour-associated antigens can stimulate the body's specific immune response toward cancer cells. This stimulation can be more effective with the assistance of immunoadjuvants or checkpoint inhibitors, which promote the maturation of antigen-presenting cells and cytotoxic T cells as well as inhibition of immune suppression mechanism in tumours.[6] Combining PTT with immunotherapy can achieve synergistic effect for the following reasons: first, the PTT-induced cancer cell death can release the tumour-specific antigens *in situ*, triggering the specific antitumour immune response; second, the development of patients' own antitumour response can eliminate disseminated, metastatic tumour beyond the scope of laser irradiation and prevent the tumour recurrence. One requirement for conducting this kind of combination therapy is to avoid the use of immunocompromised mice, which have been frequently used in many studies. Given the background, Liu *et al.* prepared the PTAs by encapsulating ICG and imiquimod (R837), a Toll-like-receptor-7 agonist together in PLGA NPs (PLGA-ICG-R837 NPs) through oil-in-water emulsions.[356] After conducting PTT with PLGA-ICG-R837 NPs *in vivo* with a 4T1 tumour model, higher percentage of matured dendritic cells (DCs) were observed in inguinal lymph nodes and tumours compared to PLGA-ICG NPs and free R837, indicating a stronger immune stimulation effect of PLGA-ICG-R837 NPs. The authors further evaluated the combination therapies in mice with both primary and secondary tumours, in which only the primary tumours were irradiated by a NIR laser. With the injection of checkpoint inhibitor, anti-cytotoxic T-lymphocyte antigen-4 (CTLA4), treating primary tumours with PLGA-ICG-R837 NPs and NIR laser irradiation, led to significant regression of both primary and secondary tumours, which was even better than that of mice treated by the combination of surgery and PLGA-ICG-R837 NPs and CTLA4. This

combination therapy can also effectively treat metastatic tumour model, made by injection of luciferase-expressed 4T1 cells (fLuc-4T1) into mice before their primary tumours were treated. The regression of secondary or distal tumour mainly resulted from the stimulated immune response by a combination of the tumour-specific antigens generated by PTT and influence of Toll-like-receptor-7 agonist and checkpoint inhibitor.

Even with tremendous progress on the combination of PTT and immunotherapy, the detailed mechanism for stimulation of immune response still needs further investigation. Most of the previous studies used checkpoint inhibitors to stimulate the immune response. A more recent study indicated that a combination of PTT with a sub-therapeutic dose of Dox can elicit robust anti-tumour immune responses and eliminate both primary and secondary tumours (Figure 18b).[357] In their work, a core-shell nanostructure with a core of a spiky Au NP in a dopamine shell was made (SGNP@PDAs) (Figure 18a). The coating of PDA can enhance the photothermal stability of spiky Au NPs under laser irradiation, thus providing a persistent and stable photothermal ability. In a CT26 tumour model, The PTT *via* SGNP@PDAs alone led to the regression of 75% large solid tumours, 4-fold higher of $CD8^+$ T-cell responses than the PBS control group, and anti-tumour immunity toward re-challenged tumours. Then the authors evaluated the combination of PTT and chemotherapy with a sub-therapeutic dose of Dox in a dual tumour mice model, in which only the primary tumours were exposed to the NIR laser irradiation. The chemotherapy alone had no obvious impact on tumour growth, yet the combination with PTT led to complete tumour regression in all the mice in the group. The regression of secondary tumours without laser irradiation was also observed. The mechanism study indicated that the infiltration and activation of $CD8^+$ T cells and NK cells by the combination therapy was responsible for the enhanced immune response to cancer cells. Finally, they demonstrated that this combination could effectively treat advanced orthotopic HNSCC tumour model and inhibit the growth of untreated, distal tumours. Overall, the combination of PTT and immunotherapy can effectively treat both locally advanced tumours and tumour metastases and develop long-time immunity towards potential recurrence.

4–3. Combining PTT with gene therapy

Gene therapy can down-regulate or substitute mutated genes with plasmid DNA or reduce certain protein expression by RNA interference.[8] In cancer treatment, gene therapy can induce the cancer cell apoptosis, down-regulate the expression of heat shock proteins that protect cells from the damage caused by photothermally induced hyperthermia, or upregulation of cytotoxic immune cytokines. Combining gene therapy with PTT can potentially achieve the similar therapeutic effect with lower laser intensity. In addition, DNA or RNA with a strong negative charge is difficult to be internalized by cells, and they suffer from serious enzymatic degradation *in vivo*. The delivery of DNA or RNA through PTA nanocarriers can enhance their cell uptake efficiency and *in vivo* stability.[358–366] It has also been reported that photothermal treatment can induce the endosomal escape of gene delivery carriers and promote the release of the gene in the cytosol.[367] Thus, the combination of PTT and gene therapy can achieve synergistic effect.[368, 369]

For example, Yang *et al.* used black phosphorous nanosheets functionalized by polyethylenimine (PEI) as a carrier to deliver survivin siRNA for combination therapy.[366] The siRNA can silence the expression of survivin protein, an inhibitor of apoptosis, to decrease cell viability. Compared to the effect of naked siRNA, 80% of survivin protein expression was inhibited by siRNA delivered *via* black phosphorous nanosheets. As a result, 44% cell inhibition was obtained due to the effect of survivin siRNA. This number was further increased to 64% with PTT, indicating the synergistic effect of the combination therapy. The authors evaluated the therapy in an MCF-7 tumour model which proved the effective treatment *via* the combination therapy than the other control groups. More recently, Xu *et al.* demonstrated that the co-delivery of plasmid DNA, antioncogene p53, and sorafenib by Au nanorod containing rattle-structured rough nanocapsules, could achieve better treatment performance with the combination of PTT, gene therapy, and chemotherapy.[364] These examples proved that combining the gene therapy-induced apoptosis with PTT can achieve overall better treatment outcomes.

Decreasing PTT dose can reduce the unexpected damage to healthy tissue in the irradiation area and the uncomfortableness of patients resulted from the heat. However, the efficiency of PTT may be compromised by the activation of heat shock proteins, which, in turn, requires stronger laser power density to overcome the thermoresistance. To solve the problem, siRNA has been used to block the heat-shock response, indicated by the expression of heat shock proteins, such as HSP70 and BAG3.[360, 361] The siRNA can interfere with the expression of heat shock proteins to inhibit the heat-shock response, thus, results in the enhancement of PTT performance. Li *et al.* reported the Au nanorods-siRNA nanocomplex for a combination of PTT and gene therapy.[359] The Au nanorods were modified by negatively charged poly(sodium 4-styrenesulfonate) (PSS) and positively charged poly(diallyldimethylammonium chloride) (PDDAC) through layer-by-layer self-assembly, exposing positive charge outside, which was further complexed with siRNA that targets BAG3. The BAG3 can form complex with HSP70 and antiapoptotic modulators can be stabilized and protected, leading to better survival and reduce thermoresistance of cancer cells. Au nanorods-siRNA nanocomplex showed comparable inhibition of BAG3 expression as commercial agents *in vitro* with Cal-27 cells. Through intratumoural injection, the treatment *via* Au nanorods-siRNA complexes plus PTT was compared to the other control groups. The intratumoural injection of the siRNA with NIR laser irradiation couldn't inhibit tumour growth, indicating low toxicity of siRNA and laser irradiation alone. The injection of Au nanorods-siRNA complex without laser irradiation or Au nanorods with laser irradiation delayed tumour growth. The injection of the Au nanorods-siRNA complex plus PTT significantly regressed tumour growth than the other control groups.

4–4. Combining PTT with PDT or photothermally induced ROS generation therapy

By using non-invasive and light-driven therapeutic nanoplatform, more efforts are concentrated on combining PTT and PDT to yield a better therapeutic synergism compared to either PTT or PDT alone.[370] Furthermore, the PTT can work in a facile manner regardless of oxygen content whereas improved oxygen perfusion by PTT can amplify PDT to yield synergistic therapeutic outcome even in severely hypoxic solid tumours. Since the first report by Liu *et al.*, combining porphyrin PS (Ce6) into graphene oxide NPs,[371] a wide

variety of nanocarriers combining PTT and PDT have been designed and examined to validate the therapeutic efficacy both *in vitro* and *in vivo*.[27, 177, 372–376] Herein, to avoid any overlapping and repetition of information, we would focus more on the recent advances of the area while providing some references to excellent reviews that have been published recently.[63, 377–379] The light-driven combination therapy of two optically different moieties co-encapsulated in a single nanoplatform is often challenged by a complex synthesis procedure. To overcome this, Xu *et al.* recently reported the fabrication of Au nanocups conjugated to a photosensitizer (PS) and TAT-peptides for tumour-targeted combined PTT/PDT *via* a simple chemical method (Figure 19a).[380] The PTT of Au nanocups with excellent PCE (38.5%) and the singlet oxygen ($^1O_2$) generation by the use of Ce6 as a PS synergistically supplemented for the complete tumour eradication at 808 and 660 nm laser irradiation, respectively. The facile synthesis process and safe dosing scheme of laser irradiations make this system compelling. However, the use of two separate laser sources might impose an additional burden for clinical applications. The use of single irradiation to achieve PTT and PDT synergistically can reduce the treatment time lag and increase the therapeutic efficacy in patients. However, the irradiation time and light dose should be chosen carefully to yield better synergistic outcomes. Recently, Dong *et al.* designed an organic diketopyrrolopyrrole triphenylamine (DPP-TPA) NPs for PAI-guided combined PTT/PDT therapy under a single 660 nm laser irradiation.[200] The enhanced PCE (34.5%) and excellent $^1O_2$ generation (33.6%) ability of NPs inhibited the tumour growth completely without any recurrence *in vivo*. One of the major advantages noted in this combination therapy is the excellent synergistic therapeutic efficacy achieved at a relatively low drug dose and laser irradiation (0.2 mg/kg, 1.0 W/cm^2) compared to the monotherapies by using the similar types of NPs.

Mild hyperthermia followed by subsequent PDT can result in better therapeutic and synergistic outcomes, because mild hyperthermia initially can result in the increased blood flow and endothelial gaps in tumours that can correspondingly improve the oxygen availability for effective PDT and also enhance the delivery of nanocarriers for better PTT.[377] The prolonged irradiation further enables the release of PS or activates ROS generation that would ultimately destroy the tumour vasculatures demonstrating synergistic PTT and PDT. Therefore, it is reasonable to combine PTT/PDT for synergistic phototherapy at a single excitation wavelength. In this regard, Chen *et al.* fabricated an organic nanodroplet comprising a PFC core as an oxygen reservoir, thermoresponsive perylene diimide (PDI) molecules and $ZnF_{16}Pc$ molecules as a PS (PS-PDI-PAnD) (Figure 19b).[245] With the controlled dosing of 675 nm laser, the PS-PDI-PAnD actively contributed for the PTT and PDT synergistically at a single irradiation. More importantly, the PFC core largely contributed to the overcoming of oxygen-deficiency in hypoxic tumours observed by negligible fluorescence of HIF1-α signals from the tumours treated with PS-PDI-PAnD. The complete tumour ablation with a minimal injury *in vivo* further validated the enhanced synergistic therapeutic outcome by combined PTT/PDT under a single irradiation dose. On a special note, oxygen replenishment strategy might impose an extra burden in the synthesis of NPs therefore limiting clinical efficiency and synergistic effect *in vivo*. Alternative strategies to generate free radicals that can induce cytotoxicity to the tumour cells similar to PDT but irrespective of the oxygen concentration can be of high clinical significance. To this end, two

similar yet innovative design strategies envisioned independently by Xia *et al.*[381] and Zhang *et al.*[382] capitalize on the photothermal effect of Au nanocages to generate free radicals from a polymerization initiator, namely, 2,2′-azobis[2-(2-imidazolin-2-yl)propane] dihydrochloride (AIPH/AIBI), to kill cancer cells, respectively (Figure 19c,d). The water-soluble azo-compounds AIPH/AIBI can decompose rapidly at a higher temperature to generate alkyl radicals (RC) to eradicate cancer cells under both normoxic and hypoxic conditions but with different mechanisms (Figure 19e). It was observed that the alkoxyl radicals (ROC) generated during normoxic condition could induce direct oxidative stress in the presence of cellular oxygen while hypoxic condition led to the generation of accumulative oxidative stress *via* GSH depletion mechanism. In brief, combining PTT with polymerization initiator has opened a new field to achieve similar therapeutic efficacy even in the harsh TME. Recently, a handful of excellent design strategies have been put forward by consuming the NIR-triggered photothermal heat generation for enhanced therapeutic efficiency. In an example, NIR induced photothermal heat was utilized to amplify the $^1O_2$ generation capacity of PS for effective PDT. Zhu *et al.* strategically designed a core-shell micelle, comprising a two-photon (2PA) absorbing hyperbranched conjugated polymer (HCP) core, a thermoresponsive shell made up of hyperbranched polyether (HPE) and grafted with a Ce6 PS on the surface (HCP@HPE-Ce6) (Figure 19f).[383] The NIR-triggered temperature elevation above LCST (~39 °C) disintegrated the intermediate thermoresponsive HPE resulting in the decreased intramolecular distance and subsequent activation of FRET between Ce6 and HCP. The activation of micelles, in turn, amplified the generation of $^1O_2$ *via* enhanced 2PA activity as observed by increased cytotoxic effect both *in vitro* and *in vivo*. Moreover, combining 2PA-PDT together with the long-wavelength NIR-light as an excitation source can offer more deep tissue penetration and excellent therapeutic efficacy (Figure 19g). Similarly, Yoon *et al.* designed a “one-for-all” (PDT/PTT/PAI) phototheranostic nanomaterial *via* self-assembled phthalocyanines conjugated to biotin as a targeting group (NanoPcTBs) (Figure 19h).[384] The nanoassemblies could inherently facilitate PTT/PAI at 655 nm laser irradiation and easily switch to trigger PDT/Fluorescence imaging *via* avidin-biotin induced partial disassembly mechanism (Figure 19i). The combined phototherapy was evident in biotin receptor-overexpressed cells (A549/HeLa) compared to biotin receptor-negative cells (WI38-VA13) demonstrating target-responsive nature of NanoPcTBs *in vitro*. *In vivo* administration of NPs showed higher tumour targeting ability in A549 xenograft model irrespective of the tumour location, however, no complete tumour inhibition was observed. Nevertheless, modular design and stimuli-responsive properties make NanoPcTBs a potential candidate for multimodal imaging and combined phototherapeutic applications.

4–5. Combining PTT with radiotherapy

Combination of PTT and radiotherapy has also been reported to achieve better antitumour effect.[39, 53, 220, 221, 385–392] Similar to PDT, radiotherapy efficacy is related to oxygen level in tumour and the photothermally induced enhancement of oxygen perfusion can increase radiotherapy efficacy. In addition, some PTAs containing high-Z elements, such as Au and bismuth (Bi), can also be used as radiosensitizers. Li *et al.* reported the synthesis of ultrasmall Bi NPs for combined PTT and radiotherapy.[392] The NPs were prepared through reduction of Bi ion into NPs by oleylamine under N_2 with heating. The obtained NPs were

transferred into water by DSPE-PEG encapsulation and labeled with peptide (CGNKRTRGC, LyP-1) for active tumour targeting. Upon illumination by a 1064 nm laser, Bi NPs were able to generate heat due to their broad absorption and photothermal effect. In the meantime, Bi NPs could also serve as a radiosensitizer for enhanced radiotherapy. The combination of RT and mild PTT with Bi NPs was evaluated in a subcutaneous mouse tumour model. The monotherapy only led to delayed growth of tumours due to the use of low X-ray dose and laser intensity. However, the combination therapy completely inhibited the growth of tumours.

4–6. Combining PTT with surgery

Surgery is frequently used in cancer treatment to remove the tumour and some of the nearby margins (primary surgery), to diagnose tumour through a surgical biopsy, and to reduce the risk of getting cancer.[358] In primary surgery, incomplete removal of tumour cells remains a serious problem that may cause lethal recurrence and metastases. The combination of PTT and surgery has some unique advantages.[50, 187, 358, 393–395] Not only that PTT can efficiently remove cancer cells, but the surgical bed can also be directly exposed to laser irradiation, overcoming the physical limitation of short laser penetration depth. In a study by Lu *et al.*, the authors demonstrated a combination of surgery and the adjuvant PTT (aPTT) decreased tumour recurrence after breast-conserving surgery (BCS) without sacrificing cosmetic outcome.[394] The BCS is recommended for treating breast cancers diagnosed at an earlier stage. It is usually followed by whole-breast radiotherapy to reduce the risk of recurrence, which, however, may increase the death rate by inducing heart or secondary malignant disease. The authors intravenously injected PEG-coated Au bipyramidal NPs as PTAs for aPTT in an orthotopic breast cancer mouse model. Instead of using a conventional laser setup, in which laser beam is focused on a small point (Figure 20a), the authors used a transformed and more evenly distributed laser beam setup for the aPTT (Figure 20b). The more uniform temperature rise of tumour region during aPTT could be observed from thermal images of tumours (Figure 20c). Though scarificing some laser intensity, aPTT could be more efficient to remove the residual tumour cells in the surgical bed, especially at the periphery of tumours, while at the same time, reduced the damage to the skin around the surgical bed to obtain good cosmetic outcomes. Histological results indicated the successful resection of tumours after surgery, yet the development of tumour recurrence after treatment *via* surgery alone indicated the presence of residual cancer cells in surgical bed. A combination of surgery with aPTT reduced the risk of tumour recurrence and achieved better cosmetic protection than the conventional PTT (Figure 20d). The combination of PTT and surgery can also be done by local injection of PTAs. Yu and colleagues reported a sprayable PTT system to achieve better cancer treatment outcomes and antibacterial properties.[187] The main components of the sprayable system was nanogels made by encapsulation of black phosphorus nanosheets into a thermosensitive polymer of poly(d,l-lactide)-poly(ethylene glycol)-poly(d,l-lactide) (PDLLA-PEG-PDLLA: PLEL). Upon laser illumination, photothermal effects of black phosphorus nanosheets induced the macroscopic gelation of nanogel. After surgical removal of the subcutaneous HeLa tumour, the PTAs were sprayed into the wound area, followed by NIR laser irradiation. The formation of gel on the wound area enhanced the photothermal effect and efficiently removed residual tumour cells. Compared to control groups without any treatment or with surgery alone, the combination of

PTT and surgery completely prevented tumour recurrence and extended survival time. Moreover, the PTAs showed good biodegradability and photothermally induced antibacterial performances, depicting great potentials in real clinical applications. These examples demonstrated the advantages of the combination of PTT and surgery. In addition, the combination of PTT, surgery and other therapies, such as immunotherapy, gene therapy, and chemotherapy can potentially further increase the treatment efficiency.[50, 358]

5. Improving cancer diagnosis and treatment *via* PAI

The ability to visualize anatomical structures in a living biological system has revolutionized the treatment efficacy in a day-to-day clinical practice. The most common and inexpensive imaging modality using rich optical source or fluorescent dyes are a good choice to discern details at both cellular and molecular levels. However, both optical and fluorescent imaging modalities suffer largely from the loss or scattering of signals in a biological medium resulting in a compromised image resolution at a millimeter depth. Fortunately, PAI combining both optical and acoustic feature offers advantages which are nearly impossible to achieve by using any of the pre-existing conventional imaging tools at the depth beyond the limit of optical detection. Unlike optical imaging, PAI mainly relies on the thermoelastic expansion of biological molecules to generate acoustic waves upon the incidence of the photon. These acoustic waves scatter minimally, therefore can be perceived from the deep tissues (beyond the limit of the optical window) without any loss in signal intensity and are readily converted to images in real-time.

In general, PAI system mainly ensembles a pulsed laser source (can also use intensity-modulated light source) for the excitation of a biological sample and an ultrasonic transducer to perceive the generated acoustic waves. But depending upon the functional capabilities, PAI embodiments may differ accordingly: photoacoustic endoscopy (PAE), focused-scanning photoacoustic microscopy (PAM), and photoacoustic tomography (PAT)/ photoacoustic computed tomography (PACT) are three main types at present.[54] Among these, PAT/PACT are specially more useful for deep tissue imaging (both microscopic and macroscopic) and offers relatively better chances for clinical applications. The state-of-the-art PAT embodiments encompassing the high end optical source (Nd:YAG to LED), ultrasonic array detectors (single-element to volumetric array), and high-performance reconstruction algorithms have already found overwhelming consideration in preclinical applications including imaging of angiogenesis, biomarkers, gene activities and also in the clinical applications such as melanoma cancer imaging, neonatal brain imaging, detection of prostate and breast cancers, and image-guided resection of sentinel lymph nodes (SLNs) for cancer staging.[396, 397]

PAI technique can inherently capture contrast from the endogenous biological absorbers to reveal the biological function, anatomy, molecular/genetic processes, and metabolism *in vivo*. Such endogenous absorbers are found inside the living subjects such as hemoglobin, DNA/RNA, water, melanin and lipids and can be illuminated by the photons to obtain PAI contrasts without altering their biological properties. Some preliminary and important attempts in this area include the use of haemoglobin to obtain functional and anatomical imaging of the blood circulation system and cancer hallmarks such as angiogenesis,[398] use

of DNA/RNA to map individual cell nuclei,[399] use of melanin for detecting and staging melanoma,[400] capturing neuronal activities,[401] blood oxygen saturation,[402] and so on. However, such intrinsic chromophores alone are unable to recapitulate every complex biological process. In order to expand PAI in a wide range of biological processes, several genetically encoded chromophores including green fluorescent proteins (GFPs), and enzymatic reporter genes such as lacZ and tyrosinase have been investigated.[403] Such reporter gene imaging enables direct or indirect visualization of the cells which are mostly invisible to PAI in the NIR window *in vivo*.[404] However, some reporter gene systems such as the family of GFPs exhibit too blue-shifted absorption and limit PAI ability due to strong background signals at the visible spectrum. Recently, a reversibly photoswitchable bacterial phytochrome BphP1 has been successfully utilized to capture tumour growth and monitor metastases by PAI with high sensitivity and better image contrasts.[405] In addition, pixel-wise subtraction of the images at OFF and ON states over 20 switching cycles greatly reduced the effect of background signal without any photobleaching.[405] Other signal amplification approaches such as dynamic contrast enhancement and multispectral unmixing have also been reported to map the distribution of contrast agents at relatively low concentrations.[406] Since multispectral unmixing depends upon the absorption wavelength of chromophores, accurate quantification of absorber concentrations at depth is crucial for the validation of result.[407]

Despite the remarkable progress of endogenous PAI contrast agents, the need for exogenous contrast agents is indispensable. The exogenous PAI contrast agents having (1) high NIR absorption per unit mass or per molar concentration, (2) absorption spectra with sharp peaks for unmixing background absorption, (3) excellent photostability under increasing intensity of excitation light, and (4) good biocompatibility are ideally suited for deep tissue PAI applications.[408] Besides, other physicochemical properties encompassing shape, size, surface chemistries, and chemical composition are also of practical relevance to improvise circulation time and imaging *in vivo*. In a general view, the exogenous PAI contrast agents almost share the photophysical properties with the photothermal nanoprobes. Therefore, most of the nanoprobes discussed for the enhanced PTT are also valid for obtaining better photoacoustic images. Recently, a wide number of exogenous PAI contrast agents have been investigated for tumour detection, imaging changes in cellular events inside TME, lymph-node imaging, and so on. Rather than distinguishing PAI contrast agents based on the molecular structure, herein we classify and highlight cancer-related applications of PAI based on the exogenous contrast agents that have been of potential interest for the advancement of PAI.

5–1. PAI nanoprobes for tumour imaging

PAI is of high importance especially in cancer treatment for precise tumour location, biodistribution of nanomedicines and therapeutic monitoring of pre- and post-treatment *in vivo*.[54, 222, 408, 409] To acknowledge this, a plethora of NPs having excellent PAI contrast have been introduced recently.[34, 57, 131, 200, 410] One of the major applications of PAI relies on the early detection of tumour that can help improve patient survival time. To this end, Gambhir *et al.* fabricated Au nanorods to image ovarian tumour for image-guided resection.[411] The dual-modality imaging technique combining surface-enhanced Raman spectroscopy

(SERS) and PAI can overcome limitations owing to the relatively poor depth penetration of SERS and low sensitivity of PAI, respectively. After optimizing different sizes of Au nanorods, NPs with an aspect ratio of 3.5 demonstrating highest photoacoustic signal were used to image the xenograft tumours of cell lines: 2008, SKOV3 and HEY. The combined imaging platform can be of potential interest to evaluate ovarian lesions in patients those who have undergone blood-based screening previously. In addition to this, exogenous contrast agents that can passively accumulate *in vivo* facilitate clear visualization of deeply-suited tumours and inner vasculatures for guided-phototherapy. Recently, Yin *et al.* reported a design of TDI-poly(acrylic acid) (TPA)-based nanomedicine (TNM) for the multispectral optoacoustic tomography (MSOT) imaging-guided PTT (Figure 21a).[34] Taking advantage of the excellent passive accumulation and longer residence time of TNM NPs *in vivo*, the MSOT acquired 3D images at 12 h revealed clear visualization of tumour size, shape, and inner vasculature essential for effective guided therapy (Figure 21b). Mice treated with TNM NPs followed by 660 nm laser irradiation showed complete tumour ablation without any sign of pulmonary metastasis compared to the controls. Alternatively, targeted contrast agents based on the antibodies, ligands or aptamers can nullify non-specific background from the incoming photoacoustic signals and facilitate enhanced localization in cancer cells to improve the signal to noise ratio significantly.[412–414] The concept of active targeting NPs has been greatly advanced for non-invasive PAI detection of several other tumours such as oral squamous carcinoma (HER2, EGFR),[415] glioblastoma ($\alpha_v\beta_3$),[416] and prostate cancer (HER2),[417] with high signal specificity and spatial resolution. Recently, Pu *et al.* reported the fabrication of a targeted SPNP (cRGD-SPNP) *via* self-quenched molecular engineering approach for enhanced PAI.[418] The simple modification of the chemical structure combined with the targeting ability of the cRGD-SPNPs eventually led to the amplified PAI contrast and clear visualization of a tumour *in vivo* (Figure 21c,d). This can be attributed to the increased cellular uptake of cRGD targeted SPNPs by 4T1 tumour cells compared to the non-targeting counterparts. In brief, both passive and active targeting NPs can aid in the enhancement of PAI signal in the tumour regions, although later may provide relatively better outcomes. PAT offers a competitive advantage to image deeply-suited tissue with high resolution compared to other optical imaging modalities such as OCT and confocal microscopy. However, to achieve this goal, exogenous contrast agent with high NIR absorption is essential. Dai *et al.* designed and demonstrated the use of an CP-based PPy NPs as a PAT contrast agent.[35] The small diameter (~46 nm) monodispersed PPy NPs having strong NIR-absorption allowed clear visualization up to the depth of ~4.3 cm *in vitro*. Further, the *in vivo* administration of PPy in a xenograft mouse model showed clear PAT images of the brain vasculature within 1 h postinjection. The rich optical contrast obtained by the injection of PPy NPs could easily differentiate the blood vessels from the brain parenchyma and was even more evident in the image acquired after image subtraction. In summary, such organic PPy NPs can serve the clinical need of highly biocompatible, and sensitive PAT contrast agents for deep-tissue imaging. In addition to this, the photoacoustic signal enhancement strategies are still crucial for improving the diagnosis sensitivity of deeply suited tumors. One of the common approaches to amplify photoacoustic signal is to increase the optical absorption characteristics of contrast agents.[56] It should also be noted that most of the enhancement techniques discussed previously in the context of PTAs are also equally applicable for photoacoustic probes. The increase in the optical property of

nanoprobe is often accompanied by the red-shifted absorption peak which further helps to minimize background noise and therefore enhance the photoacoustic contrasts.[419] Other newly designed nanoprobes such as the photoswitchable proteins or activatable agents which have been discussed in the preceding section also accounts for the indirect enhancement of photoacoustic signals *via* background minimization approach. Alternatively, improving the photothermal properties or heat transfer processes can correspondingly help to improve the photoacoustic sensitivity as well.[420] This may take account of various surface modification techniques such as coating plasmonic materials by graphene oxide, silica layers and others. For instance, Pu *et al.* have utilized silica layer as a surface engineering technique to amplify photoacoustic contrast of SPNPs.[421] The silica coated SPNPs increased interfacial heat conductance resulting in higher photothermal heating and subsequent increase in photoacoustic contrasts as compared to the uncoated SPNPs. Nevertheless, continuous effort is directed in screening better surface modification strategy that can yield excellent photoacoustic contrasts. For instance, compared to the fully silica coated gold nanoshells, the use of anisotropic silica coated-Au NPs have been recently reported to enhance PAI abilities *in vivo.*[422] According to the design, the partially exposed gold surface could interact to form plasmon-coupled aggregates in a tumor environment resulting in higher NIR photoacoustic intensity and better imaging resolution. In brief, strategies encompassing absorption modulation either *via* surface coating or aggregation of plasmonic nanomaterials, effective heat transfer mechanism, and background signal reduction are essential tools for the amplification of photoacoustic signal in tumor imaging.

5–2. PA nanoprobes for the lymph node imaging and cell tracking

Metastasis of cancer cells in the distant organs is the major cause of cancer-related deaths.[423] The major pathway for the dissemination of metastatic cells is routed *via* lymphatic vessels to their draining LNs. Therefore, mapping of metastases in the first lymph node i.e. sentinel lymph node (SLN) is essential for cancer staging. The current modality for the lymph node mapping in the clinic is based on SLN biopsy which demands very experienced hands even to meet the accuracy of approximately 95%.[396] Besides, other invasive procedures such as radiolabelled colloid, methylene blue or isosulfan blue are also clinically available. However, invasive diagnosis technique often increases the risk of sensory nerve injury, seroma formation and lymphedema in patients. The recent advancements in PAI and nanomaterial-based exogenous contrast agents propose an alternative method in the noninvasive, nonionizing, and high-resolution mapping of SLN in the small animal model. PAI using Au nanocages demonstrated a depth capability of ~31 mm for SLN mapping with satisfactory spatial resolution and clinical potential.[424] Based on a similar strategy, other commercially cheap and biocompatible NPs have also been reported as PAT contrast agents for near-infrared detection of SLN.[425] However, the only major issue about these materials is the long-term toxicity issue *in vivo* for clinical translation. Towards this goal, various organic NPs based on small molecules such as cyanine, porphyrin, and SPNPs have also been designed and used to map SLNs and lymphatic vessels.[426] The complete fluorescence quenching and high particle extinction coefficient owing to the high-density packing of porphyrin enabled clear visualization of rat lymph nodes *via* PAI and simultaneously the non-radiative decay of porphyrin excitons aided excellent PTT.[19] In a clinical setting, size variance of colloidal NPs is challenging to match the surgery window with the NP migration

and distribution. The size of NP is a critical factor which determines the rate of diffusion through the interstitium, draining in the lymphatic system, and uptake by the LNs. Therefore, to overcome the unmet clinical urgency, Chen *et al.* investigated size-dependent accumulation of perylene diimide (PDI) NPs in the lymphatic system *via* PAI and PET imaging after intravenous injection.[42] A series of radiolabelled [^{64}Cu] PDI NPs were formulated and self-assembled to yield NPs of sizes 30, 60, 100, and 200 nm. The investigation results revealed that 100 nm is the optimal size for differentiating sciatic and popliteal LNs based on the time required by the PDI NPs to migrate to the popliteal LN (20 mins) and then to the sciatic LN (90 min) after injection (Figure 22a,b). The total migration time of NPs facilitates surgical window of 1 h to which is essential to perform SLN biopsy and other relevant examinations. The size-dependent migration results of PDI NPs are noteworthy to identify ideal time window for multiple bio-applications and pathological examinations in the clinic. Moreover, to improve the detection sensitivity by contrast enhancement, PAI has also been used in combination with fluorescence imaging for the non-invasive lymph node mapping.[427] The detection of circulating cancer cells *in vivo* also provides an alternative way for the prevention of metastases in distant organs. Towards this goal, Zharov *et al.* depicted a way to magnetically capture circulating tumour cells in the bloodstream of mice followed by rapid photoacoustic detection.[428] The multicolour detection and magnetic trapping strategy greatly facilitated *in vivo* detection of circulating tumour cells (CTCs) labelled with magnetic NPs for flow velocities up to 5 cm s^{-1}. The clinical application of such strategy may aid in the microsurgical extraction of captured CTCs for pathological analysis or non-invasive ablation using a laser to prevent the spread of metastasis in the distant organs. A more robust design of targeted NPs can be utilized further for the real-time tracking and precise elimination of residual tumours *in vivo*. To accomplish this, Lapotko *et al.* reported a cancer cell-specific plasmonic nanobubbles (PNBs) that can assist intraoperative surgery of both resectable/unresectable residual microtumours (MRD, microscopic residual disease) with a precision sensitivity of single cell, acoustic detection time of 1 ms and penetration depth of 4 mm in a real time.[57] The basic strategy follows, (i) systemic delivery of EGFR conjugated Au NPs that can selectively accumulate as a cluster in cancer cells but not in the normal cells (Figure 22c), (ii) low power laser irradiation to generate PNBs followed by acoustic detection (Figure 22d), (iii) intraoperative surgery assisted by PNBs for resectable MRDs or PNB mediated mechanical destruction of unresectable MRDs. The highly sensitive real-time acoustic detection and specificity of PNBs revealed improved surgical benefit in both of the cases *in vivo*. Recent advances in the detection of an individual cell by PAI have been extended further to characterize the morphological abnormalities in the cells,[429] changes in the oxygen saturation of individual flowing red blood cells and so on.[430]

5–3. PAI nanoprobes for TME imaging

Tumour progression is mostly accompanied by the aberrant changes in the activity of enzymes (MMPs, Furin, Hyaluronidase), reactive oxygen species (ROS), proteins and pH within a TME. Therefore, accurate and sensitive monitoring/detection can provide invaluable information regarding the disease progression. This can be even more useful in the design of novel therapeutic tools for the prevention of tumours at the early stage.

Recently a large number of PA nanoprobes have been investigated for imaging the changes in the tumour microenvironment. [431]

5–3-1. PAI for the imaging of pH in the TME—The metabolic changes in a TME, beyond the Warburg Effect, is a cumulative effect of acidosis, hypoxia and/or hyperkalemia. [432] In particular, the shift in the metabolic state of a cell, for example, low pH, inside a TME is among few reasons for the failure of cancer treatment as observed by metastasis, tumour recurrence, and angiogenesis.[433] Therefore, the design of pH-sensitive probes is quite essential for evaluating the success of therapeutic interventions. In a recent example based on NP-dye complexes with dual photoacoustic absorption strategy, Pu *et al.* have proposed activatable ratiometric PAI probes for pH monitoring by the use of SPNPs.[434] The design combines an inert semiconducting oligomer (SO, F-DTS) photoacoustic matrix and a BODIPY (pH-BDP) that can serve as both photoacoustic enhancer and pH indicator. The surface characteristics of pH-BDP having hydroxyl group can undergo protonation at acidic environment thereby endowing pH-sensing ability to the semiconducting oligomer nanoprobes (SONs). The SONs prepared by doping $50_{w/w}$% of pH-BDP into F-DTS showed dual absorption peak at 680 nm and a shoulder peak at 750 nm that could completely quench the fluorescence of F-DTS (Figure 23a,b). However, with the decreasing pH, the absorption peak at 750 nm decreased while 680 nm peak remained the same, providing corresponding ratiometric signal changes at pH 5.5 [Ab_{680}/Ab_{750}, $R_{5.5}$=8.6] measured by 3.44 and 1.91-fold increase compared to $R_{7.4}$=2.5 and $R_{6.4}$=4.5, respectively. Therefore, the highest signal-to-noise ratio calculated as $R_{5.5}/R_{7.4}$ and linear ratiometric response (PAI_{680}/PAI_{750}) in the physiologically relevant pH range allowed accurate estimation of the pH. In addition, *in vivo* PAI performed on the subcutaneous HeLa xenograft tumour model showed relatively increased photoacoustic intensity at 680 nm (ΔPAI_{680}) with time compared to the negligible change at 750 nm (ΔPAI_{750}) owing mainly to the simultaneous acidic activation of the nanoprobes in the TME (Figure 23c). The resulting ratiometric maximum photoacoustic intensity ($\Delta PAI_{680}/\Delta PAI_{750}$) at 6 h postinjection estimated by the calibration curve was found to be ~6.3 which was very close to the theoretical value reported in the range of 6.5–6.8 (Figure 23d). Although not exact, these results depict relative accuracy both *in vitro* and *in vivo* by using a simple ratiometric PAI probe. Of a similar note, other highly reliable pH-activatable PAI probes based on turn-off[435] or turn-on[436] strategy have also been investigated in living tumour mice models. So far, true quantitative measurement of pH by using PAI is challenged by the intermix of background signals coming mostly from the dual forms of haemoglobin (oxygenated and deoxygenated). Conventional spectral acoustic methods using simple linear unmixing strategies are therefore incapable to separate them at the time of imaging.[437] Future progress should encompass more elegant spectral unmixing technique that can reduce the complexity in the separation of background signals and improve the detection sensitivity of physiological parameters, *in vivo*[438]. Recently, Wang *et al.* reported an elegant approach for the detection of pH using four different laser wavelengths (565, 576, 584 and 600 nm) combined with spectral unmixing as a background reduction technique.[439] This method substantially resolved the intermix of haemoglobin signals coming from the background to yield true quantitative pH value with a minimal error of ~0.16 pH at the penetration depth of 6 mm. Although this is the lowest possible error

reported at present, further quantification is possible after considering the depth-dependent fluence attenuation of the laser when simulating the point-by-point pH levels.

5–3-2. PAI for the imaging of ROS in the TME—The other small-molecule mediators in the TME comprise of ROS and is an essential hallmark of various pathological diseases including cancer. In stark contrast to the pH-activatable PAI probes, the ROS in the TME can severely degrade the NPs *in vivo*, therefore limiting the efficiency of ROS imaging PAI probes. The challenge is usually pursued with the improved photostability of the NPs that can resist ROS-induced degradation *in vivo*. To this end, Pu *et al.* designed a ratiometric photoacoustic probe for imaging ROS by combining a photovoltaic SP derivative-SPNP1 [poly(cyclopentadithiophene-alt-benzothiadiazole)] and a ROS-sensitive cyanine dye derivative (IR775S) having two separate strong absorption peaks in the NIR-region.[440] Herein, the cyanine dye as a sensing unit responded to the target molecule $ONOO^-$ and ClO^- to yield the absorption change at 735 and 820 nm, and the other SPNP1-inert dye served as the reference absorption at 750 nm for ratiometric detection. The IR775S doped SPNP1 did not show any corresponding change in the photoacoustic intensity when reacted with other ROS ($^{\bullet}NO$, $O2^{\bullet-}$, $^{\bullet}OH$, H_2O_2 and $^1O_2$) validating effective ratiometric detection of ROS *via* PAI (PAI700/PAI820). The ratiometric detection was also validated in murine macrophage RAW264.7 cells and zymosan sensitized murine model of acute oedema both *in vitro* and *in vivo*, respectively. Recently, Pu *et al.* have extended this concept to design a self-assembled activatable and biodegradable PAI probes encapsulating a hydrophobic dye NIR775 for *in vivo* detection of hypochlorite (ClO^-) (Figure 23e).[441] In this design, a ROS inert NIR775 dye at 780 nm was used as a reference absorption while the semiconducting oligomer amphiphile (SOA) worked as a target sensitive molecule having absorption at 680 nm (Figure 23f). The robust design considerations based on $\pi-\pi$ stacking and hydrophobic interactions to form a structurally stable oligomer NPs followed by subsequent degradation of ClO^- oxidizable backbone in the presence of target analyte allows higher flexibility for preclinical imaging applications (Figure 23g). The ratiometric detection ($\Delta PAI_{780}/\Delta PAI_{680}$) of ClO^- was investigated by recording the decreasing photoacoustic intensity at 680 nm to the unchanged signal intensity at 780 nm in the presence of ClO^- both *in vitro* and *in vivo* (Figure 23h,i). Recently, in a separate experiment, Pu *et al.* have introduced a new activatable NIR-absorbing SPNP probe for the PAI of peroxynitrite ($ONOO^-$) *in vivo*.[442] The detection of $ONOO^-$ is imperative in understanding the immunosuppressive TME and facilitate the design of effective immunotherapeutic nanoprobes. In comparison to earlier ratiometric probes, the new design strategy based on the absorption shift (in the presence of the target analyte) eliminates the challenging task of selecting two optically different materials. In this regard, the primary sensing component, boronate-caged boron-dipyrromethene dye (BBD), were doped using peroxynitrite-responsive bulky boranes: triphenylborane (TPB)/tris(pentafluorophenyl)borane (TPFB) to enhance specificity towards the ratiometric detection of $ONOO^-$. The minimal interference of H_2O_2 was attributed to the presence of excess bulky boranes that safeguarded the BBD within nanoprobes. The sensing property of BBD nanoprobes in the presence of $ONOO^-$ for selective ratiometric PAI (PAI_{750}/PAI_{680}) was envisioned with the decreasing absorption peak at 675 nm accompanied by a subsequent increase at 745 nm. *In vivo* experimental data conducted in a 4T1 xenograft tumour model with/without pre-treatment of a ROS scavenger, N-acetyl-l-cysteine (NAC),

further validated the efficacy of doped BBD nanoprobes. The signal obtained at 4 h post injection in NAC-untreated mice showed maximum ratiometric photoacoustic intensity compared to the treated ones, indicating effective activation of BBD nanoprobes *in vivo*.

5–3-3. PAI for the imaging of enzymes in the TME—The enzymatic degradation of the proteins in the ECM by MMPs (family of zinc-dependent endopeptidases) have a crucial role in the pathogenesis of tumours and other diseases such as cardiovascular, inflammatory and neurological disorders. Therefore, development of noninvasive imaging tool that can monitor the MMP activity within TME would help understand the tumour biology. In this regard, Liu *et al.* fabricated a PAI probe based on copper sulfide (CuS) NPs that are conjugated to a black hole quencher 3 (BHQ3) *via* an MMP-cleavable peptide linker (CPQ).[443] The CPQ NPs initially revealed two distinct separated absorption peaks having strong photoacoustic signal at 630 nm and 930 nm for BHQ3 and CuS, respectively. Inside TME, the CPQ NPs showed decreased PA signal at 680 nm originating from the BHQ3. This can be explained with respect to the activity of MMPs inside TME that can specifically cleave the peptide linker promoting faster clearance of BHQ3 compared to the CuS NPs that retained inside the tumour for the longer time period. The relative change in the photoacoustic signal of CPQ obtained at 680 nm/930 nm correspondingly served as the indicator of MMPs activity inside the TME. Several other target/stimuli-responsive PAI nanoprobes are already underway for cancer-related applications and have been reviewed elsewhere.[181, 444]

5–3-4. PAI for the imaging of proteins in the TME—Of particular note, ROS-generated stress in TME is also directly linked to the direct modification of protein structures, for example, chemoselective oxidation of cysteine residues by H_2O_2 generation, that has an important role in the tumourigenesis or other pathological processes. Therefore, non-invasive detection of proteins such as cysteine sulfenic acid, the initial oxidation product formed after the reaction of H_2O_2 and a thiolate, can provide in-depth genetic information about tumourigenesis. So far, very few fluorescent probes[445] or immunostaining methods[446] have been reported for successful detection of sulfenic acids in tumour models. To meet the current clinical demand, Pu *et al.* synthesized a reaction-based NIR-absorbing SPNPs (rSPNPs) for PAI of protein sulfenic acids *in vivo*.[447] The enhanced sensitivity in the detection of sulfenic acids was pursued by specific design considerations to minimize the interference from the optically active SPs without compromising the imaging properties. The design of NPs basically comprised an SP core shielded by the inert silica and PEGylated corona. The surface functionalization was further achieved using a sulfenic acid reactive group (1,3-cyclohexanedione) *via* click chemistry. The *in vivo* PAI signal intensity at 680 nm was relatively higher for rSPNP2 compared to SPNP2 owing to the reactivity of protein sulfenic acids and rSPNP2 in a TME (Figure 24a,b). The specificity of the protein interaction to rSPNP2 was further validated by the immunofluorescence staining study that showed higher green fluorescence intensity after reacting with the antisulfenic acid antibody (Figure 24c,d).

5–3-5. PAI for the imaging of hypoxic state in the TME—So far, PAI has made huge progress in both diagnosis and treatment of cancer and other life-threatening diseases,

nevertheless, still several key issues regulating sensitivity and efficacy and other impressive applications are yet to be achieved. In the special note, hypoxia detection in a solid tumour is crucial for both preclinical and clinical studies. Recently, the development of a hypoxia-responsive small molecule for the PAI of the hypoxic tumour is note-worthy.[448] The N-oxide (Hyp-1) can convert to aniline (red-Hyp-1) followed by the corresponding red-shifted absorption from 670 to 760 nm in the oxygen-deficient condition. This bathochromic shift allows detection of photoacoustic signals from the red-Hyp-1 molecules but not from the Hyp-1 upon excitation at 760 nm. Therefore, strong PAI signals detected from the tumour region of mice correspondingly represents the severe hypoxic state *in vivo* (Figure 24e,f). In the similar background, future works should be focused on the design of more effective PAI nanoprobes for *in vivo* applications in this direction.

5–4. Next generation PAI contrast agents

Contrast-enhanced PAI signal generation *via* gaseous expansion, *e.g.* microbubbles (MBs) having a gaseous core and enveloping shell made of polymer/lipid, can aid molecular imaging and subsequent tumour detection through the visualization of targets expressed on the tumour vasculatures. Recently, Zheng *et al.* designed a photonic MB based on a porphyrin shell and lipids that self-assembled into a phospholipid bilayer nanovesicles encapsulating a fluorinated gas (called as “Porsche MBs”).[449] Unlike several other contrast agents synthesized *via* a complex mechanism, this method is relatively facile following a single step process to yield highly stable and stiff porphyrin-lipid conjugate of size ~2.7 μm (3–5 times higher stiffness). In addition, porphyrin-lipid conjugate and high order packing density within the MB shell could contribute to enhanced PAI signal generation. MBs functional capacity can be further enhanced by the use of various NPs as a surface coating material.[450] The surface functionalization can endow MBs with multifunctionality and also help enhance the stability in the biological medium.[451] Recently, Paradossi *et al.* have proposed a new concept to attach pristine graphene on the surface of poly(vinyl alcohol) based MBs (PVA MBs) *via* surfactant assisted ultrasonication technique for enhancing PAI signals both *in vitro* and *in vivo*.[452] Such graphene-polymer shelled MBs may provide a new perspective to capture endogenous metabolites having low absorption and allows customized targeting of diseases after successful surface functionalization. Besides, MBs have also been used as a multimodal imaging contrast agent for both ultrasound/PAI by incorporating NIR absorbing plasmonic agents and can further enhance PAI by changing optoacoustic contrast.[453] The major limitation of MBs is the size in micrometer ranges, therefore, limits extravasation into the tumour *via* the EPR effect. Although ultrasound-mediated MBs conversion to NPs has shown a great advantage for therapeutic applications,[27] the enhanced PAI contrast is yet difficult to achieve after conversion.[454] An alternative strategy to obtain enhanced PAI contrast similar to MBs is possible by the use of phase-change nanodroplets. The use of liquid phase-change nanoscale contrast agents instead of the gaseous core can extend PAI ability beyond the extravascular targets and facilitate receptor-targeted interaction at the molecular level.[455] Recently, Emelianov *et al.* synthesized a biocompatible and biologically safe ICG-loaded perfluorocarbon (PFC) nanodroplets for enhanced ultrasonic imaging.[456] PFC droplets encapsulating optical absorbers such as ICG are likely to experience laser-triggered phase transition (at relatively less energy than high intensity ultrasound), a liquid to gas phase, thereby inducing a one-time high amplitude PAI signal.

As designed ICG-PFC nanodroplets facilitated the obvious enhancement of PAI and ultrasonic images measured in terms of contrast, suggesting a valuable tool for cancer diagnosis. To enhance PAI and ultrasound imaging in a wider NIR range, smaller nanodroplets (core ~250 nm diameter) based on PPy shell and PFC core, called as sonophotoacoustics (SPA), has been proposed by Pozzo *et al.*[457] The selection of a PFC core based on low boiling points have reduced the activation threshold of droplet vaporization drastically (2-fold) to match ideally with the clinical safety limit (0.2 MPa at 1 mJ/cm^2). Although PAI allows deep tumour imaging non-invasively, it is highly advantageous to incorporate fluorescence imaging in a single nanoplatform to overcome low-sensitivity of PAI alone. To accomplish this, Tang *et al.* recently introduced a light-triggered smart organic NP that allows a facile switch from PAI to fluorescence imaging with respect to the change in molecular structure, *viz.*, closed-ring to ring-opened state, respectively.[458] The newly designed smart dithienylethene-2-(1-(4-(1,2,2-triphenylvinyl)phenyl)ethylidene)malononitrile (DTE-TPECM) NP allowing simultaneous preoperative PAI and intraoperative fluorescence imaging/PDT can be a useful tool for image-guided surgery *in vivo*. However, the limitations of using two different excitations and emission wavelength for switching has to be resolved further. At present, PAI is well documented to overcome penetration depth with better imaging resolution. However, use of PAI contrast agents in the NIR-I window are still susceptible to higher background signals coming from the endogenous chromophores that lie nearly in the same window. Recently, newly designed PAI contrast agents that have absorption range in the longer wavelength, NIR-II window, have drastically improved the signal to noise ratio mainly due to less scattering and reduced tissue absorbance in the living biological tissues. The early proof-of-concept application presented by Pu *et al.* to capture photoacoustic image from the deep-suited brain vasculatures at 1064 nm laser irradiation (NIR-II) have energized additional research in NIR-II-based PAI (Figure 25a).[459] This newly designed SPNP-derivate having red-shifted absorption in the NIR-II range exhibited ~1.5-fold higher SNR for the PAI acquired at 1064 nm compared to 750 nm at the same tissue depth of 3 cm (Figure 25b-d). Taking advantage of higher MPE especially for longer wavelength, deep penetration (approx. 4 to 5 cm) at a relatively increased drug concentration (0.05 mg/ml to 1 mg/ml) and increased laser energy density (5.5 to 20 mJ/cm^2) was clearly evident during *ex vivo* imaging. Therefore, shifting absorption from first to second NIR-window is meaningful for enhancing PAI contrast especially for imaging deep underlying living structures *in vivo* and highlights need for more research in this direction. The rapid development in the fabrication of similar NIR-II-based on SPNPs for PAI of deep-suited tumour further supports the growing opportunities in the field of biomedical imaging and cancer therapy.[460, 461]

6. Summary and outlook

In summary, the rapid development of nanotechnology has greatly contributed to the advancement of PTT and PAI in cancer treatment and diagnosis. PTT is an effective, non-invasive, and highly targeted cancer therapy. New biocompatible and degradable PTA materials with improved PCE have been invented and proven to be effective in at least pre-clinical experiments. Scientists have been investigating the effect of shape, size, and surface coating of PTAs on improving their tumour delivery efficiency through EPR effect or active

targeting. With the advancement in the targeted therapy, tumour accumulation has been greatly benefitted as observed by the increasing preclinical success of photothermal treatment globally. In addition, the photothermal effect can modulate TME to improve the tumour delivery efficiency, which can be further improved by adding responsive properties to PTAs to make them “smart”. Most importantly, novel intraparticle engineering approaches have been thoroughly studied to maximize non-radiative energy transfer resulting in higher PCE. In addition to the excellent therapeutic efficacy of PTT, researchers have also highlighted the need for imaging-guided therapy. This has successfully led to the development of multimodal imaging-guided PTT resulting in the simultaneous monitoring of therapeutic efficacy and treatment response in animal models *in vivo.* Furthermore, combining PTT with other therapies can potentially treat tumours outside the scope of laser irradiation and achieve better therapeutic outcomes compared to PTT alone. Especially, combining PTT with immunotherapy could be very promising, since photothermally induced cancer cell death can elicit patients’ own immune response to fight against cancers. Despite encouraging advancements, translation of pre-clinical successes as observed in PTT/PAI into the real clinical application is the most challenging task. Some clinical trials with PTT using Au nanoshells were conducted, but no result has been reported.[14] The challenge for the clinical translation is related to both limited penetration depth of laser light and general concerns regarding applying nanotechnology *in vivo.* More effort should be concentrated in the development and approval of PTAs having larger extinction coefficients specially in the NIR-II for the treatment and imaging of deeply-suited tumours. Current strategies to overcome laser penetration problem for PTT include using a fibre optic NIR laser to penetrate the body to reach tumours or combination of PTT with surgery, in which the surgical bed can be directly exposed to laser irradiation. Further improvement of the laser fibre device could lead to better treatment and diagnosis performances. The general concerns regarding using nanomaterials for PTT include low delivery of PTAs in tumours, safety issues, and inability to achieve a large-scale synthesis of PTAs with good safety control. The delivery of NPs in a tumour through intravenous injection still has much room for improvement. Our insufficient understanding of interactions between NPs and organs, MPS systems, and tumours hinders the development of new PTA designs for improved tumour uptake. The innovative design of PTAs that can overcome different biological barriers to reach tumours and targeted locations should be developed based on our improved knowledge of nano-bio interactions. For example, endowing PTAs with a biological mimic coating, such as cell membrane camouflage, could be a promising direction for future study. An alternative strategy is to use local injection instead of intravenous injection and combining PTT with other therapies for better treatment. The safety concerns include both side effect during treatment and toxicity of nanomaterials. The side effect can be decreased by developing more precise PTT with heat regulation mechanisms in a complex biological system. For example, more accurate and sensitive real-time temperature monitoring techniques need to be developed and coupled with lasers with adjustable power density to avoid unnecessary damages caused by overtreatment. Furthermore, the PTAs should have fast imaging signals that indicate their distribution and concentration in tumours to assist the adjustment of the intensity and spot size of laser light during the treatment for better outcomes. In addition, it would be helpful to design NPs that selectively target cancer cells with significantly lower uptake by other types of cells in tumours to further decrease the side

effect during treatment, which requires the presence of the functional groups on NPs with high specificity and affinity to cancer cells. The toxicity regarding using nanoformulation *in vivo* are different from small molecules since they would stay in the body for a much longer time. The toxicity concerns not only come from NPs themselves, but also from most of the solvents and chemicals involved during the synthesis. Although nanomaterials may exhibit low cytotoxicity to cells or organs or tissues in a short time range, their long-time cytotoxicity and related immune response should be carefully evaluated.[30] One possible direction to reduce the safety concerns is to design biodegradable and clearable PTAs. Yet, it has to be noted that improving NPs biodegradability and clearance ability may sacrifice their stability and blood retention time, leading to decreased tumour uptake. Such trade-offs invite more challenges to design suitable PTAs for these applications. In addition, lacking a scalable production method and quality control especially for large synthesis are another two factors that limit the clinical translation of PTAs. The injection dose of PTAs increases rapidly as the studied models change from small animals to big animals and eventually to human beings. Scaled-up production of nanomaterials without changing their quality sets a very high requirement for the synthesis of many types of PTAs. This is essential for both developing effective PTAs for real clinical applications and reducing the costs for the treatment. Regarding this issue, simple formulations may be more promising to be translated into clinical applications.

PAI can be of high clinical relevance in monitoring disease, tumor progression, and therapeutic efficacy non-invasively. And one major advantage to combine PAI and PTT to fight cancer is to achieve simultaneous cancer diagnosis and treatment by using only one type of materials. Herein, we have reviewed and discussed several excellent proof-of-concept applications of PAI including lymph node detection, TME imaging, cell tracking and so on. Although rich optical contrast is essential for PAI applications, it should not come with the expense of higher drug dosage. The emerging photoacoustic contrast agents should therefore minimize the trade-off between drug dosage and contrast enhancement for the effective clinical application. Recent progress in the design of a stimuli-responsive photoacoustic nanoprobes demonstrating excellent dynamic contrast-enhanced PAI, high signal to noise ratio, and enhanced sensitivity should empower great advantage for the future clinical studies.[462] The clinical application of PAI further relies upon the adequate accuracy of contrast agents to facilitate excellent quantification *in vivo* regardless of penetration depth. The depth-dependent light attenuation and intermix of unwanted background signals imposes great challenge in the accurate quantification of biological parameters by PAI *in vivo*, such as pH value in tumors.[407, 434] So far, only a very few photoacoustic contrast agents have been able to meet such stringent criteria but with some limitations. Therefore, next generation PAI should fundamentally address this issue based on the design and implementation of novel reconstruction and spectral unmixing algorithms.[439] For instance, the recently reported eigenspectra multispectral optoacoustic tomography (eMSOT) has shown upto 10-fold improved estimation of blood oxygen saturation (sO_2) at tissue depths >5 mm compared to the conventional linear spectral unmixing.[438] Alternatively, design of novel PAI probes having spectral properties in the NIR range combined together with emerging unmixing algorithms should offer additional benefit to enhance sensitivity and accuracy of the system. To ensure higher pre-clinical impact, it is plausible to improve the

biodegradability of photoacoustic contrast agents *in vivo*. In a recent example, the development of fully degradable SPNPs by the action of ROS in the stimulated macrophages *in vitro* envisages a bright future of SPNPs for future studies.[463] More rigorous *in vivo* studies in a realistic animal models are expected in this direction. Beside this, other technical challenges[54] such as thick bone penetration for imaging of brain-tumours, air-filled cavities such as imaging of lung tumours and some experimental inconsistencies[464] such as variations in the use of animal model, drug doses, tumor sizes/weight and physicochemical properties of NPs should be rationalized with the progress of PAI system, harmonization of experimental protocols, and compliance within safety limits[465] for both diagnosis and therapy. Overall, there is still a long way to go before PTAs can be translated into real clinical applications, which requires the joint effort of scientists around the globe.

Supplementary Material

Refer to Web version on PubMed Central for supplementary material.

Acknowledgments

The work was financially supported by the Intramural Research Program of the National Institute of Biomedical Imaging and Bioengineering, National Institutes of Health and National Key Research and Development Program of China (No. 2016YFA0201400).

References

1. Li Z, Tan S, Li S, Shen Q and Wang K, Oncol. Rep, 2017, 38, 611–624. [PubMed: 28627697]
2. Kalbasi A, Komar C, Tooker GM, Liu M, Lee JW, Gladney WL, Ben-Josef E and Beatty GL, Clin. Cancer Res, 2017, 23, 137–148. [PubMed: 27354473]
3. Perez-Herrero E and Fernandez-Medarde A, Eur. J. Pharm. Biopharm, 2015, 93, 52–79. [PubMed: 25813885]
4. Curtin NJ, Nat. Rev. Cancer, 2012, 12, 801–817. [PubMed: 23175119]
5. Baumann M, Krause M and Hill R, Nat. Rev. Cancer, 2008, 8, 545–554. [PubMed: 18511937]
6. Ribas A and Wolchok JD, Science, 2018, 359, 1350–1355. [PubMed: 29567705]
7. June CH, O'Connor RS, Kawalekar OU, Ghassemi S and Milone MC, Science, 2018, 359, 1361–1365. [PubMed: 29567707]
8. Teo PY, Cheng W, Hedrick JL and Yang YY, Adv. Drug Deliv. Rev, 2016, 98, 41–63. [PubMed: 26529199]
9. Shen J, Zhang W, Qi R, Mao ZW and Shen H, Chem. Soc. Rev, 2018, 47, 1969–1995. [PubMed: 29417968]
10. Fan W, Huang P and Chen X, Chem. Soc. Rev, 2016, 45, 6488–6519. [PubMed: 27722560]
11. Ban Q, Bai T, Duan X and Kong J, Biomater. Sci, 2017, 5, 190–210. [PubMed: 27990534]
12. Zou L, Wang H, He B, Zeng L, Tan T, Cao H, He X, Zhang Z, Guo S and Li Y, Theranostics, 2016, 6, 762–772. [PubMed: 27162548]
13. Beik J, Abed Z, Ghoreishi FS, Hosseini-Nami S, Mehrzadi S, Shakeri-Zadeh A and Kamrava SK, J. Control. Release, 2016, 235, 205–221. [PubMed: 27264551]
14. Abadeer NS and Murphy CJ, J. Phys. Chem. C, 2016, 120, 4691–4716.
15. Gai S, Yang G, Yang P, He F, Lin J, Jin D and Xing B, Nano Today, 2018, 19, 146–187.
16. Jung HS, Verwilst P, Sharma A, Shin J, Sessler JL and Kim JS, Chem. Soc. Rev, 2018, 47, 2280–2297. [PubMed: 29528360]
17. Cheng L, Wang C, Feng L, Yang K and Liu Z, Chem. Rev, 2014, 114, 10869–10939. [PubMed: 25260098]

18. Riley RS and Day ES, Wiley Interdiscip. Rev. Nanomed. Nanobiotechnol, 2017, 9, e1449.
19. Lovell JF, Jin CS, Huynh E, Jin HL, Kim C, Rubinstein JL, Chan WCW, Cao WG, Wang LV and Zheng G, Nat. Mater, 2011, 10, 324–332. [PubMed: 21423187]
20. Chen YW, Su YL, Hu SH and Chen SY, Adv. Drug Deliv. Rev, 2016, 105, 190–204. [PubMed: 27262922]
21. Liu T and Liu Z, Adv. Healthc. Mater, 2018, 7, e1701158. [PubMed: 29280340]
22. Lin H, Wang Y, Gao S, Chen Y and Shi J, Adv. Mater, 2018, 30, 1703284.
23. Matsumoto Y, Nichols JW, Toh K, Nomoto T, Cabral H, Miura Y, Christie RJ, Yamada N, Ogura T, Kano MR, Matsumura Y, Nishiyama N, Yamasoba T, Bae YH and Kataoka K, Nat. Nanotechnol, 2016, 11, 533–538. [PubMed: 26878143]
24. Bertrand N, Wu J, Xu X, Kamaly N and Farokhzad OC, Adv. Drug Deliv. Rev, 2014, 66, 2–25. [PubMed: 24270007]
25. Setyawati MI, Tay CY, Chia SL, Goh SL, Fang W, Neo MJ, Chong HC, Tan SM, Loo SCJ, Ng KW, Xie JP, Ong CN, Tan NS and Leong DT, Nat. Commun, 2013, 4, 1673. [PubMed: 23575677]
26. Matsumura Y and Maeda H, Cancer Res, 1986, 46, 6387–6392. [PubMed: 2946403]
27. Xu Y, Liang X, Bhattarai P, Sun Y, Zhou Y, Wang S, Chen W, Ge H, Wang J, Cui L and Dai Z, Adv. Funct. Mater, 2017, 27, 1704096.
28. Lin LS, Yang X, Zhou Z, Yang Z, Jacobson O, Liu Y, Yang A, Niu G, Song J, Yang HH and Chen X, Adv. Mater, 2017, 29, 1606681.
29. Wang Z, Huang P, Jacobson O, Wang Z, Liu Y, Lin L, Lin J, Lu N, Zhang H, Tian R, Niu G, Liu G and Chen X, ACS Nano, 2016, 10, 3453–3460. [PubMed: 26871955]
30. Ali MR, Rahman MA, Wu Y, Han T, Peng X, Mackey MA, Wang D, Shin HJ, Chen ZG, Xiao H, Wu R, Tang Y, Shin DM and El-Sayed MA, Proc. Natl. Acad. Sci. U. S. A, 2017, 114, E3110–E3118. [PubMed: 28356516]
31. Zhu X, Feng W, Chang J, Tan YW, Li J, Chen M, Sun Y and Li F, Nat. Commun, 2016, 7, 10437. [PubMed: 26842674]
32. Melamed JR, Edelstein RS and Day ES, ACS Nano, 2015, 9, 6–11. [PubMed: 25590560]
33. Chen Q, Wen J, Li H, Xu Y, Liu F and Sun S, Biomaterials, 2016, 106, 144–166. [PubMed: 27561885]
34. Zhang S, Guo W, Wei J, Li C, Liang XJ and Yin M, ACS Nano, 2017, 11, 3797–3805. [PubMed: 28301720]
35. Zha Z, Yue X, Ren Q and Dai Z, Adv. Mater, 2013, 25, 777–782. [PubMed: 23143782]
36. Chen H, Shao L, Ming T, Sun Z, Zhao C, Yang B and Wang J, Small, 2010, 6, 2272–2280. [PubMed: 20827680]
37. Lu X, Yuan P, Zhang W, Wu Q, Wang X, Zhao M, Sun P, Huang W and Fan Q, Polym. Chem, 2018, 9, 3118–3126.
38. Han X, Huang J, Jing X, Yang D, Lin H, Wang Z, Li P and Chen Y, ACS Nano, 2018, 12, 4545–4555. [PubMed: 29697960]
39. Li A, Li X, Yu X, Li W, Zhao R, An X, Cui D, Chen X and Li W, Biomaterials, 2017, 112, 164–175. [PubMed: 27768971]
40. Cao Y, Dou JH, Zhao NJ, Zhang S, Zheng YQ, Zhang JP, Wang JY, Pei J and Wang Y, Chem. Mater, 2017, 29, 718–725.
41. Tsai MF, Chang SH, Cheng FY, Shanmugam V, Cheng YS, Su CH and Yeh CS, ACS Nano, 2013, 7, 5330–5342. [PubMed: 23651267]
42. Yang Z, Tian R, Wu J, Fan Q, Yung BC, Niu G, Jacobson O, Wang Z, Liu G, Yu G, Huang W, Song J and Chen X, ACS Nano, 2017, 11, 4247–4255. [PubMed: 28345873]
43. Liu Y, Wang Z, Liu Y, Zhu G, Jacobson O, Fu X, Bai R, Lin X, Lu N, Yang X, Fan W, Song J, Wang Z, Yu G, Zhang F, Kalish H, Niu G, Nie Z and Chen X, ACS Nano, 2017, 11, 10539–10548. [PubMed: 28953351]
44. Kinnear C, Moore TL, Rodriguez-Lorenzo L, Rothen-Rutishauser B and Petri-Fink A, Chem. Rev, 2017, 117, 11476–11521. [PubMed: 28862437]

45. Yang H, Chen Z, Zhang L, Yung WY, Leung KC, Chan HY and Choi CH, Small, 2016, 12, 5178–5189. [PubMed: 27442290]
46. Albanese A, Tang PS and Chan WC, Annu. Rev. Biomed. Eng, 2012, 14, 1–16. [PubMed: 22524388]
47. Zhang Z, Wang J, Nie X, Wen T, Ji Y, Wu X, Zhao Y and Chen C, J. Am. Chem. Soc, 2014, 136, 7317–7326. [PubMed: 24773323]
48. Zeng JY, Zhang MK, Peng MY, Gong D and Zhang XZ, Adv. Funct. Mater, 2018, 28, 1705451.
49. Yao M, Ma Y, Liu H, Khan MI, Shen S, Li S, Zhao Y, Liu Y, Zhang G, Li X, Zhong F, Jiang W and Wang Y, Biomacromolecules, 2018, 19, 1130–1141. [PubMed: 29514006]
50. Wang T, Wang D, Yu H, Feng B, Zhou F, Zhang H, Zhou L, Jiao S and Li Y, Nat. Commun, 2018, 9, 1532. [PubMed: 29670088]
51. Wang P, Zhang L, Zheng W, Cong L, Guo Z, Xie Y, Wang L, Tang R, Feng Q, Hamada Y, Gonda K, Hu Z, Wu X and Jiang X, Angew. Chem., Int. Ed, 2018, 57, 1491–1496.
52. Chen W, Qin M, Chen X, Wang Q, Zhang Z and Sun X, Theranostics, 2018, 8, 2229–2241. [PubMed: 29721075]
53. Guo Z, Zhu S, Yong Y, Zhang X, Dong X, Du J, Xie J, Wang Q, Gu Z and Zhao Y, Adv. Mater, 2017, 29, 1704136.
54. Nie L and Chen X, Chem. Soc. Rev, 2014, 43, 7132–7170. [PubMed: 24967718]
55. Li J, Rao J and Pu K, Biomaterials, 2018, 155, 217–235. [PubMed: 29190479]
56. Wang S, Lin J, Wang T, Chen X and Huang P, Theranostics, 2016, 6, 2394–2413. [PubMed: 27877243]
57. Lukianova-Hleb EY, Kim YS, Belatsarkouski I, Gillenwater AM, O'Neill BE and Lapotko DO, Nat. Nanotechnol, 2016, 11, 525–532. [PubMed: 26878142]
58. Kim H, Chung K, Lee S, Kim DH and Lee H, Wiley Interdiscip. Rev. Nanomed. Nanobiotechnol, 2016, 8, 23–45. [PubMed: 25903643]
59. Huang X, Jain PK, El-Sayed IH and El-Sayed MA, Lasers Med. Sci, 2008, 23, 217–228. [PubMed: 17674122]
60. Melancon MP, Zhou M and Li C, Acc. Chem. Res, 2011, 44, 947–956. [PubMed: 21848277]
61. Ai X, Mu J and Xing B, Theranostics, 2016, 6, 2439–2457. [PubMed: 27877246]
62. Shanmugam V, Selvakumar S and Yeh CS, Chem. Soc. Rev, 2014, 43, 6254–6287. [PubMed: 24811160]
63. Vankayala R and Hwang KC, Adv. Mater, 2018, 30, e1706320. [PubMed: 29577458]
64. Tang Y, Yang T, Wang Q, Lv X, Song X, Ke H, Guo Z, Huang X, Hu J, Li Z, Yang P, Yang X and Chen H, Biomaterials, 2018, 154, 248–260. [PubMed: 29144983]
65. Dreaden EC, Alkilany AM, Huang X, Murphy CJ and El-Sayed MA, Chem. Soc. Rev, 2012, 41, 2740–2779. [PubMed: 22109657]
66. Li X, Shan J, Zhang W, Su S, Yuwen L and Wang L, Small, 2017, 13, 1602660.
67. Tan C, Cao X, Wu XJ, He Q, Yang J, Zhang X, Chen J, Zhao W, Han S, Nam GH, Sindoro M and Zhang H, Chem. Rev, 2017, 117, 6225–6331. [PubMed: 28306244]
68. Huang K, Li Z, Lin J, Han G and Huang P, Chem. Soc. Rev, 2018, 47, 5109–5124. [PubMed: 29667670]
69. Song XJ, Chen Q and Liu Z, Nano Res, 2015, 8, 340–354.
70. Chen H, Shao L, Li Q and Wang J, Chem. Soc. Rev, 2013, 42, 2679–2724. [PubMed: 23128995]
71. Alkilany AM, Thompson LB, Boulos SP, Sisco PN and Murphy CJ, Adv. Drug Deliv. Rev, 2012, 64, 190–199. [PubMed: 21397647]
72. Bardhan R, Grady NK, Cole JR, Joshi A and Halas NJ, ACS Nano, 2009, 3, 744–752. [PubMed: 19231823]
73. Xia Y, Li W, Cobley CM, Chen J, Xia X, Zhang Q, Yang M, Cho EC and Brown PK, Acc. Chem. Res, 2011, 44, 914–924. [PubMed: 21528889]
74. Liu YJ, He J, Yang KK, Yi CL, Liu Y, Nie LM, Khashab NM, Chen XY and Nie ZH, Angew. Chem., Int. Ed, 2015, 54, 15809–15812.

75. Lee HE, Ahn HY, Mun J, Lee YY, Kim M, Cho NH, Chang K, Kim WS, Rho J and Nam KT, Nature, 2018, 556, 360–365. [PubMed: 29670265]
76. O'Neal DP, Hirsch LR, Halas NJ, Payne JD and West JL, Cancer Lett, 2004, 209, 171–176. [PubMed: 15159019]
77. Hirsch LR, Stafford RJ, Bankson JA, Sershen SR, Rivera B, Price RE, Hazle JD, Halas NJ and West JL, Proc. Natl. Acad. Sci. U. S. A, 2003, 100, 13549–13554. [PubMed: 14597719]
78. Huang X, El-Sayed IH, Qian W and El-Sayed MA, J. Am. Chem. Soc, 2006, 128, 2115–2120. [PubMed: 16464114]
79. Vigderman L and Zubarev ER, Chem. Mater, 2013, 25, 1450–1457.
80. Ye X, Zheng C, Chen J, Gao Y and Murray CB, Nano Lett, 2013, 13, 765–771. [PubMed: 23286198]
81. Jia H, Fang C, Zhu XM, Ruan Q, Wang YX and Wang J, Langmuir, 2015, 31, 7418–7426. [PubMed: 26079391]
82. Sanchez-Iglesias A, Winckelmans N, Altantzis T, Bals S, Grzelczak M and Liz-Marzan LM, J. Am. Chem. Soc, 2017, 139, 107–110. [PubMed: 28009166]
83. Chang HH and Murphy CJ, Chem. Mater, 2018, 30, 1427–1435.
84. Huang P, Lin J, Li W, Rong P, Wang Z, Wang S, Wang X, Sun X, Aronova M, Niu G, Leapman RD, Nie Z and Chen X, Angew. Chem., Int. Ed, 2013, 52, 13958–13964.
85. Liao J, Li W, Peng J, Yang Q, Li H, Wei Y, Zhang X and Qian Z, Theranostics, 2015, 5, 345–356. [PubMed: 25699095]
86. Zhang W, Wang F, Wang Y, Wang J, Yu Y, Guo S, Chen R and Zhou D, J. Control. Release, 2016, 232, 9–19. [PubMed: 27072026]
87. Jana NR, Gearheart L and Murphy CJ, Adv. Mater, 2001, 13, 1389–1393.
88. Nikoobakht B and El-Sayed MA, Chem. Mater, 2003, 15, 1957–1962.
89. Gonzalez-Rubio G, Diaz-Nunez P, Rivera A, Prada A, Tardajos G, Gonzalez-Izquierdo J, Banares L, Llombart P, Macdowell LG, Alcolea Palafox M, Liz-Marzan LM, Pena-Rodriguez O and Guerrero-Martinez A, Science, 2017, 358, 640–644. [PubMed: 29097547]
90. Li Q, Zhuo X, Li S, Ruan Q, Xu Q-H and Wang J, Adv. Opt. Mater, 2015, 3, 801–812.
91. Lee JH, Gibson KJ, Chen G and Weizmann Y, Nat. Commun, 2015, 6, 7571. [PubMed: 26113393]
92. Hu Y, Chou TM, Wang HJ and Du H, *J. Phys. Chem*. C., 2014, 118, 16011–16018.
93. Jimenez de Aberasturi D, Serrano-Montes AB, Langer J, Henriksen-Lacey M, Parak WJ and Liz-Marzán LM, Chem. Mater, 2016, 28, 6779–6790.
94. Song J, Yang X, Yang Z, Lin L, Liu Y, Zhou Z, Shen Z, Yu G, Dai Y, Jacobson O, Munasinghe J, Yung B, Teng GJ and Chen X, ACS Nano, 2017, 11, 6102–6113. [PubMed: 28605594]
95. Liu Y, He J, Yang K, Yi C, Liu Y, Nie L, Khashab NM, Chen X and Nie Z, Angew. Chem., Int. Ed, 2015, 54, 15809–15812.
96. Song J, Zhou J and Duan H, J. Am. Chem. Soc, 2012, 134, 13458–13469. [PubMed: 22831389]
97. He J, Huang X, Li YC, Liu Y, Babu T, Aronova MA, Wang S, Lu Z, Chen X and Nie Z, J. Am. Chem. Soc, 2013, 135, 7974–7984. [PubMed: 23642094]
98. Yavuz MS, Cheng Y, Chen J, Cobley CM, Zhang Q, Rycenga M, Xie J, Kim C, Song KH, Schwartz AG, Wang LV and Xia Y, Nat. Mater, 2009, 8, 935–939. [PubMed: 19881498]
99. Li C, Zhang Y, Li Z, Mei E, Lin J, Li F, Chen C, Qing X, Hou L, Xiong L, Hao H, Yang Y and Huang P, Adv. Mater, 2018, 30, 1706150.
100. Deng H, Zhong Y, Du M, Liu Q, Fan Z, Dai F and Zhang X, Theranostics, 2014, 4, 904–918. [PubMed: 25057315]
101. Zheng T, Li GG, Zhou F, Wu R, Zhu JJ and Wang H, Adv. Mater, 2016, 28, 8218–8226. [PubMed: 27459898]
102. You J, Zhang G and Li C, ACS Nano, 2010, 4, 1033–1041. [PubMed: 20121065]
103. Huang X, Tang S, Mu X, Dai Y, Chen G, Zhou Z, Ruan F, Yang Z and Zheng N, Nat. Nanotechnol, 2011, 6, 28–32. [PubMed: 21131956]
104. Tang S, Chen M and Zheng N, Small, 2014, 10, 3139–3144. [PubMed: 24729448]

105. Zhou Z, Wang Y, Yan Y, Zhang Q and Cheng Y, ACS Nano, 2016, 10, 4863–4872. [PubMed: 27054555]
106. Dumas A and Couvreur P, Chem. Sci, 2015, 6, 2153–2157. [PubMed: 28694948]
107. Chen Y, Tan C, Zhang H and Wang L, Chem. Soc. Rev, 2015, 44, 2681–2701. [PubMed: 25519856]
108. Augustine S, Singh J, Srivastava M, Sharma M, Das A and Malhotra BD, Biomater. Sci, 2017, 5, 901–952. [PubMed: 28401206]
109. Gong L, Yan L, Zhou R, Xie J, Wu W and Gu Z, J. Mat. Chem. B, 2017, 5, 1873–1895.
110. Zhu SA, Gong LJ, Xie JN, Gu ZJ and Zhao YL, Small Methods, 2017, 1, 1700220.
111. Chen Z, Wang Q, Wang H, Zhang L, Song G, Song L, Hu J, Wang H, Liu J, Zhu M and Zhao D, Adv. Mater, 2013, 25, 2095–2100. [PubMed: 23427112]
112. Liu Y, Bhowmick S and Yakobson BI, Nano Lett, 2011, 11, 3113–3116. [PubMed: 21732643]
113. Lin LS, Cong ZX, Li J, Ke KM, Guo SS, Yang HH and Chen GN, J. Mat. Chem. B, 2014, 2, 1031–1037.
114. Chen W, Ouyang J, Yi X, Xu Y, Niu C, Zhang W, Wang L, Sheng J, Deng L, Liu YN and Guo S, Adv. Mater, 2018, 30, 1703458.
115. Qiu M, Wang D, Liang W, Liu L, Zhang Y, Chen X, Sang DK, Xing C, Li Z, Dong B, Xing F, Fan D, Bao S, Zhang H and Cao Y, Proc. Natl. Acad. Sci. U. S. A, 2018, 115, 501–506. [PubMed: 29295927]
116. Choi JR, Yong KW, Choi JY, Nilghaz A, Lin Y, Xu J and Lu X, Theranostics, 2018, 8, 1005–1026. [PubMed: 29463996]
117. Markovic ZM, Harhaji-Trajkovic LM, Todorovic-Markovic BM, Kepic DP, Arsikin KM, Jovanovic SP, Pantovic AC, Dramicanin MD and Trajkovic VS, Biomaterials, 2011, 32, 1121–1129. [PubMed: 21071083]
118. Yang K, Zhang S, Zhang G, Sun X, Lee ST and Liu Z, Nano Lett, 2010, 10, 3318–3323. [PubMed: 20684528]
119. Orecchioni M, Cabizza R, Bianco A and Delogu LG, Theranostics, 2015, 5, 710–723. [PubMed: 25897336]
120. Robinson JT, Tabakman SM, Liang Y, Wang H, Casalongue HS, Vinh D and Dai H, J. Am. Chem. Soc, 2011, 133, 6825–6831. [PubMed: 21476500]
121. Pan J, Zhu X, Chen X, Zhao Y and Liu J, Biomater. Sci, 2018, 6, 372–387. [PubMed: 29334095]
122. Splendiani A, Sun L, Zhang Y, Li T, Kim J, Chim CY, Galli G and Wang F, Nano Lett, 2010, 10, 1271–1275. [PubMed: 20229981]
123. Chou SS, Kaehr B, Kim J, Foley BM, De M, Hopkins PE, Huang J, Brinker CJ and Dravid VP, Angew. Chem., Int. Ed, 2013, 52, 4160–4164.
124. Wang S, Li K, Chen Y, Chen H, Ma M, Feng J, Zhao Q and Shi J, Biomaterials, 2015, 39, 206–217. [PubMed: 25468372]
125. Lin H, Wang X, Yu L, Chen Y and Shi J, Nano Lett, 2017, 17, 384–391. [PubMed: 28026960]
126. Xuan J, Wang Z, Chen Y, Liang D, Cheng L, Yang X, Liu Z, Ma R, Sasaki T and Geng F, Angew. Chem., Int. Ed, 2016, 55, 14569–14574.
127. Lin H, Gao S, Dai C, Chen Y and Shi J, J. Am. Chem. Soc, 2017, 139, 16235–16247. [PubMed: 29063760]
128. Fu HD, Li ZB, Xie HH, Sun ZB, Wang BK, Huang H, Han GL, Wang HY, Chu PK and Yu XF, RSC Adv, 2017, 7, 14618–14624.
129. Shao J, Xie H, Huang H, Li Z, Sun Z, Xu Y, Xiao Q, Yu XF, Zhao Y, Zhang H, Wang H and Chu PK, Nat. Commun, 2016, 7, 12967. [PubMed: 27686999]
130. Qian X, Gu Z and Chen Y, Mater. Horiz, 2017, 4, 800–816.
131. Yang T, Tang Y, Liu L, Lv X, Wang Q, Ke H, Deng Y, Yang H, Yang X, Liu G, Zhao Y and Chen H, ACS Nano, 2017, 11, 1848–1857. [PubMed: 28117993]
132. Zhou M, Li J, Liang S, Sood AK, Liang D and Li C, ACS Nano, 2015, 9, 7085–7096. [PubMed: 26098195]

133. Yang W, Guo W, Le W, Lv G, Zhang F, Shi L, Wang X, Wang J, Wang S, Chang J and Zhang B, ACS Nano, 2016, 10, 10245–10257. [PubMed: 27791364]
134. Zhang S, Sun C, Zeng J, Sun Q, Wang G, Wang Y, Wu Y, Dou S, Gao M and Li Z, Adv. Mater, 2016, 28, 8927–8936. [PubMed: 27560922]
135. Chen H, Song M, Tang J, Hu G, Xu S, Guo Z, Li N, Cui J, Zhang X, Chen X and Wang L, ACS Nano, 2016, 10, 1355–1362. [PubMed: 26741791]
136. Saeed M, Iqbal MZ, Ren WZ, Xia YZ, Liu C, Khan WS and Wu AG, J. Mat. Chem. B, 2018, 6, 3800–3810.
137. Ou G, Li Z, Li D, Cheng L, Liu Z and Wu H, Nano Res, 2016, 9, 1236–1243.
138. Yuan L, Lin W, Zheng K, He L and Huang W, Chem. Soc. Rev, 2013, 42, 622–661. [PubMed: 23093107]
139. Rajora MA, Lou JWH and Zheng G, Chem. Soc. Rev, 2017, 46, 6433–6469. [PubMed: 29048439]
140. Bhattarai P and Dai Z, Adv. Healthc. Mater, 2017, 6, 1700262.
141. Doane TL and Burda C, Chem. Soc. Rev, 2012, 41, 2885–2911. [PubMed: 22286540]
142. Mishra A, Behera RK, Behera PK, Mishra BK and Behera GB, Chem. Rev, 2000, 100, 1973–2012. [PubMed: 11749281]
143. Le Guennic B and Jacquemin D, Acc. Chem. Res, 2015, 48, 530–537. [PubMed: 25710687]
144. Pansare V, Hejazi S, Faenza W and Prud'homme RK, Chem. Mater, 2012, 24, 812–827. [PubMed: 22919122]
145. Pham W, Cassell L, Gillman A, Koktysh D and Gore JC, Chem. Commun, 2008, 0, 1895–1897.
146. Rasnik I, McKinney SA and Ha T, Nat. Methods, 2006, 3, 891–893. [PubMed: 17013382]
147. Sun W, Guo S, Hu C, Fan J and Peng X, Chem. Rev, 2016, 116, 7768–7817. [PubMed: 27314280]
148. Luo S, Zhang E, Su Y, Cheng T and Shi C, Biomaterials, 2011, 32, 7127–7138. [PubMed: 21724249]
149. Sheng ZH, Hu DH, Xue MM, He M, Gong P and Cai LT, Nanomicro Lett, 2013, 5, 145–150.
150. Zhang C, Wang S, Xiao J, Tan X, Zhu Y, Su Y, Cheng T and Shi C, Biomaterials, 2010, 31, 1911–1917. [PubMed: 19963270]
151. Cheng L, He WW, Gong H, Wang C, Chen Q, Cheng ZP and Liu Z, Adv. Funct. Mater, 2013, 23, 5893–5902.
152. Ng KK and Zheng G, Chem. Rev, 2015, 115, 11012–11042. [PubMed: 26244706]
153. Li MH, Teh C, Ang CY, Tan SY, Luo Z, Qu QY, Zhang YY, Korzh V and Zhao YL, Adv. Funct. Mater, 2015, 25, 5602–5610.
154. Yoon HJ, Lee HS, Lim JY and Park JH, ACS Appl. Mater. Interfaces, 2017, 9, 5683–5691. [PubMed: 28152314]
155. Pan GY, Jia HR, Zhu YX and Wu FG, Nanoscale, 2018, 10, 2115–2127. [PubMed: 29326993]
156. Luo H, Wang Q, Deng Y, Yang T, Ke H, Yang H, He H, Guo Z, Yu D, Wu H and Chen H, Adv. Funct. Mater, 2017, 27, 1702834.
157. Zhou Y, Liang X and Dai Z, Nanoscale, 2016, 8, 12394–12405. [PubMed: 26730838]
158. Huang P, Qian X, Chen Y, Yu L, Lin H, Wang L, Zhu Y and Shi J, J. Am. Chem. Soc, 2017, 139, 1275–1284. [PubMed: 28024395]
159. <j/>Spring BQ, Bryan Sears R, Zheng LZ, Mai Z, Watanabe R, Sherwood ME, Schoenfeld DA, Pogue BW, Pereira SP, Villa E and Hasan T, Nat. Nanotechnol, 2016, 11, 378–387. [PubMed: 26780659]
160. Zhang P, Hu C, Ran W, Meng J, Yin Q and Li Y, Theranostics, 2016, 6, 948–968. [PubMed: 27217830]
161. Singh S, Aggarwal A, Bhupathiraju NV, Arianna G, Tiwari K and Drain CM, Chem. Rev, 2015, 115, 10261–10306. [PubMed: 26317756]
162. Ormond AB and Freeman HS, Materials, 2013, 6, 817–840. [PubMed: 28809342]
163. Liu K, Xing R, Zou Q, Ma G, Mohwald H and Yan X, Angew. Chem., Int. Ed, 2016, 55, 3036–3039.

164. Lu K, He C and Lin W, J. Am. Chem. Soc, 2015, 137, 7600–7603. [PubMed: 26068094]
165. Carter KA, Shao S, Hoopes MI, Luo D, Ahsan B, Grigoryants VM, Song W, Huang H, Zhang G, Pandey RK, Geng J, Pfeifer BA, Scholes CP, Ortega J, Karttunen M and Lovell JF, Nat. Commun, 2014, 5, 3546. [PubMed: 24699423]
166. Lin J, Wang S, Huang P, Wang Z, Chen S, Niu G, Li W, He J, Cui D, Lu G, Chen X and Nie Z, ACS Nano, 2013, 7, 5320–5329. [PubMed: 23721576]
167. Kumar R, Ohulchanskyy TY, Roy I, Gupta SK, Borek C, Thompson ME and Prasad PN, ACS Appl. Mater. Interfaces, 2009, 1, 1474–1481. [PubMed: 20355951]
168. Ramachandran R, Malarvizhi GL, Chandran P, Gupta N, Menon D, Panikar D, Nair S and Koyakutty M, J Biomed Nanotechnol, 2014, 10, 1401–1415. [PubMed: 25016641]
169. Jang WD, Nishiyama N, Zhang GD, Harada A, Jiang DL, Kawauchi S, Morimoto Y, Kikuchi M, Koyama H, Aida T and Kataoka K, Angew. Chem., Int. Ed, 2005, 44, 419–423.
170. Richter AM, Waterfield E, Jain AK, Canaan AJ, Allison BA and Levy JG, Photochem Photobiol, 1993, 57, 1000–1006. [PubMed: 8367528]
171. Abrahamse H and Hamblin MR, Biochem. J, 2016, 473, 347–364. [PubMed: 26862179]
172. Jin CS, Lovell JF, Chen J and Zheng G, ACS Nano, 2013, 7, 2541–2550. [PubMed: 23394589]
173. Wang T, Wang D, Yu H, Wang M, Liu J, Feng B, Zhou F, Yin Q, Zhang Z, Huang Y and Li Y, ACS Nano, 2016, 10, 3496–3508. [PubMed: 26866752]
174. MacLaughlin CM, Ding L, Jin C, Cao P, Siddiqui I, Hwang DM, Chen J, Wilson BC, Zheng G and Hedley DW, J. Biomed. Opt, 2016, 21, 84002. [PubMed: 27552306]
175. Lim CK, Shin J, Lee YD, Kim J, Oh KS, Yuk SH, Jeong SY, Kwon IC and Kim S, Theranostics, 2012, 2, 871–879. [PubMed: 23082099]
176. Li X, Peng XH, Zheng BD, Tang J, Zhao Y, Zheng BY, Ke MR and Huang JD, Chem. Sci, 2018, 9, 2098–2104. [PubMed: 29675251]
177. He H, Ji S, He Y, Zhu A, Zou Y, Deng Y, Ke H, Yang H, Zhao Y, Guo Z and Chen H, Adv. Mater, 2017, 29, 1606690.
178. Spence GT, Hartland GV and Smith BD, Chem. Sci, 2013, 4, 4240–4244.
179. Chen Q, Liu X, Zeng J, Cheng Z and Liu Z, Biomaterials, 2016, 98, 23–30. [PubMed: 27177219]
180. Pu K, Chattopadhyay N and Rao J, J. Control. Release, 2016, 240, 312–322. [PubMed: 26773769]
181. Lyu Y and Pu K, Adv. Sci, 2017, 4, 1600481.
182. Pu K, Mei J, Jokerst JV, Hong G, Antaris AL, Chattopadhyay N, Shuhendler AJ, Kurosawa T, Zhou Y, Gambhir SS, Bao Z and Rao J, Adv. Mater, 2015, 27, 5184–5190. [PubMed: 26247171]
183. Jiang Y and Pu K, Acc. Chem. Res, 2018, 51, 1840–1849. [PubMed: 30074381]
184. Miao Q and Pu K, Adv. Mater, 0, 1801778.
185. Shen Y, Shuhendler AJ, Ye D, Xu JJ and Chen HY, Chem. Soc. Rev, 2016, 45, 6725–6741. [PubMed: 27711672]
186. Qian CG, Chen YL, Feng PJ, Xiao XZ, Dong M, Yu JC, Hu QY, Shen QD and Gu Z, Acta Pharmacol. Sin, 2017, 38, 764–781. [PubMed: 28552910]
187. Shao J, Ruan C, Xie H, Li Z, Wang H, Chu PK and Yu XF, Adv. Sci, 2018, 5, 1700848.
188. Song X, Gong H, Yin S, Cheng L, Wang C, Li Z, Li Y, Wang X, Liu G and Liu Z, Adv. Funct. Mater, 2014, 24, 1194–1201.
189. Gong H, Cheng L, Xiang J, Xu H, Feng L, Shi X and Liu Z, Adv. Funct. Mater, 2013, 23, 6059–6067.
190. Zhang J, Yang C, Zhang R, Chen R, Zhang Z, Zhang W, Peng SH, Chen X, Liu G, Hsu CS and Lee CS, Adv. Funct. Mater, 2017, 27, 1605094. [PubMed: 29046623]
191. Dimitriev OP, Macromolecules, 2004, 37, 3388–3395.
192. Yang J, Choi J, Bang D, Kim E, Lim EK, Park H, Suh JS, Lee K, Yoo KH, Kim EK, Huh YM and Haam S, Angew. Chem., Int. Ed, 2011, 50, 441–444.
193. Wang J, Guo F, Yu M, Liu L, Tan F, Yan R and Li N, J. Control. Release, 2016, 237, 23–34. [PubMed: 27388755]
194. Ju E, Dong K, Liu Z, Pu F, Ren J and Qu X, Adv. Funct. Mater, 2015, 25, 1574–1580.

195. Tan X, Wang J, Pang X, Liu L, Sun Q, You Q, Tan F and Li N, ACS Appl. Mater. Interfaces, 2016, 8, 34991–35003. [PubMed: 27957854]
196. Cheng L, Yang K, Chen Q and Liu Z, ACS Nano, 2012, 6, 5605–5613. [PubMed: 22616847]
197. Au KM, Lu Z, Matcher SJ and Armes SP, Adv. Mater, 2011, 23, 5792–5795. [PubMed: 22102372]
198. Yang K, Xu H, Cheng L, Sun C, Wang J and Liu Z, Adv. Mater, 2012, 24, 5586–5592. [PubMed: 22907876]
199. Liang X, Li Y, Li X, Jing L, Deng Z, Yue X, Li C and Dai Z, Adv. Funct. Mater, 2015, 25, 1451–1462.
200. Cai Y, Liang P, Tang Q, Yang X, Si W, Huang W, Zhang Q and Dong X, ACS Nano, 2017, 11, 1054–1063. [PubMed: 28033465]
201. Lyu Y, Zeng J, Jiang Y, Zhen X, Wang T, Qiu S, Lou X, Gao M and Pu K, ACS Nano, 2018, 12, 1801–1810. [PubMed: 29385336]
202. Guo L, Liu WM, Niu GL, Zhang PP, Zheng XL, Jia QY, Zhang HY, Ge JC and Wang PF, J. Mat. Chem. B, 2017, 5, 2832–2839.
203. Qi J, Fang Y, Kwok RTK, Zhang X, Hu X, Lam JWY, Ding D and Tang BZ, ACS Nano, 2017, 11, 7177–7188. [PubMed: 28692799]
204. Henderson TA and Morries LD, Neuropsychiatr. Dis. Treat, 2015, 11, 2191–2208. [PubMed: 26346298]
205. Perez-Hernandez M, Del Pino P, Mitchell SG, Moros M, Stepien G, Pelaz B, Parak WJ, Galvez EM, Pardo J and de la Fuente JM, ACS Nano, 2015, 9, 52–61. [PubMed: 25493329]
206. Ng KK, Weersink RA, Lim L, Wilson BC and Zheng G, Angew. Chem., Int. Ed, 2016, 55, 10003–10007.
207. Zhen X, Zhang J, Huang J, Xie C, Miao Q and Pu K, Angew. Chem., Int. Ed, 2018, 57, 7804–7808.
208. Wang S, Lin J, Wang Z, Zhou Z, Bai R, Lu N, Liu Y, Fu X, Jacobson O, Fan W, Qu J, Chen S, Wang T, Huang P and Chen X, Adv. Mater, 2017, 29, 1701013.
209. Sun X, Huang X, Yan X, Wang Y, Guo J, Jacobson O, Liu D, Szajek LP, Zhu W, Niu G, Kiesewetter DO, Sun S and Chen X, ACS Nano, 2014, 8, 8438–8446. [PubMed: 25019252]
210. Sun X, Cai W and Chen X, Acc. Chem. Res, 2015, 48, 286–294. [PubMed: 25635467]
211. Chen L, Chen J, Qiu S, Wen L, Wu Y, Hou Y, Wang Y, Zeng J, Feng Y, Li Z, Shan H and Gao M, Small, 2018, 14, 1702700.
212. Tang Z, Zhang H, Liu Y, Ni D, Zhang H, Zhang J, Yao Z, He M, Shi J and Bu W, Adv. Mater, 2017, 29, 1701683.
213. Song J, Wu B, Zhou Z, Zhu G, Liu Y, Yang Z, Lin L, Yu G, Zhang F, Zhang G, Duan H, Stucky GD and Chen X, Angew. Chem, 2017, 129, 8222–8226.
214. Liu Y, Yang X, Huang Z, Huang P, Zhang Y, Deng L, Wang Z, Zhou Z, Liu Y, Kalish H, Khachab NM, Chen X and Nie Z, Angew. Chem., Int. Ed, 2016, 55, 15297–15300.
215. Zhao J, Zhong D and Zhou S, J. Mat. Chem. B, 2018, 6, 349–365.
216. Sun SK, Wang HF and Yan XP, Acc. Chem. Res, 2018, 51, 1131–1143. [PubMed: 29664602]
217. Jiang Y and Pu K, Small, 2017, 13, 1700710.
218. Ke H, Wang J, Dai Z, Jin Y, Qu E, Xing Z, Guo C, Yue X and Liu J, Angew. Chem., Int. Ed, 2011, 50, 3017–3021.
219. Jiang X, Liu R, Tang P, Li W, Zhong H, Zhou Z and Zhou J, RSC Adv, 2015, 5, 80709–80718.
220. Dou Y, Li X, Yang W, Guo Y, Wu M, Liu Y, Li X, Zhang X and Chang J, ACS Appl. Mater. Interfaces, 2017, 9, 1263–1272. [PubMed: 28029033]
221. Wang J, Tan X, Pang X, Liu L, Tan F and Li N, ACS Appl. Mater. Interfaces, 2016, 8, 24331–24338. [PubMed: 27595856]
222. Smith BR and Gambhir SS, Chem. Rev, 2017, 117, 901–986. [PubMed: 28045253]
223. Chen Z, Zhao P, Luo Z, Zheng M, Tian H, Gong P, Gao G, Pan H, Liu L, Ma A, Cui H, Ma Y and Cai L, ACS Nano, 2016, 10, 10049–10057. [PubMed: 27934074]

224. Zheng M, Yue C, Ma Y, Gong P, Zhao P, Zheng C, Sheng Z, Zhang P, Wang Z and Cai L, ACS Nano, 2013, 7, 2056–2067. [PubMed: 23413798]
225. Song S, Shen H, Yang T, Wang L, Fu H, Chen H and Zhang Z, ACS Appl. Mater. Interfaces, 2017, 9, 9484–9495. [PubMed: 28256824]
226. Welsher K, Sherlock SP and Dai H, Proc. Natl. Acad. Sci. U. S. A, 2011, 108, 8943–8948. [PubMed: 21576494]
227. Zhen X, Xie C and Pu K, Angew. Chem., Int. Ed, 2018, 57, 3938–3942.
228. Chen LJ, Sun SK, Wang Y, Yang CX, Wu SQ and Yan XP, ACS Appl. Mater. Interfaces, 2016, 8, 32667–32674. [PubMed: 27934189]
229. Goel S, England CG, Chen F and Cai W, Adv. Drug Deliv. Rev, 2017, 113, 157–176. [PubMed: 27521055]
230. Zhou M, Zhang R, Huang M, Lu W, Song S, Melancon MP, Tian M, Liang D and Li C, J. Am. Chem. Soc, 2010, 132, 15351–15358. [PubMed: 20942456]
231. Goel S, Chen F, Luan S, Valdovinos HF, Shi S, Graves SA, Ai F, Barnhart TE, Theuer CP and Cai W, Adv. Sci, 2016, 3, 1600122.
232. Goel S, Ferreira CA, Chen F, Ellison PA, Siamof CM, Barnhart TE and Cai W, Adv. Mater, 2018, 30, 1704367.
233. Ni D, Jiang D, Im HJ, Valdovinos HF, Yu B, Goel S, Barnhart TE, Huang P and Cai W, Biomaterials, 2018, 171, 144–152. [PubMed: 29689411]
234. Liu T, Shi S, Liang C, Shen S, Cheng L, Wang C, Song X, Goel S, Barnhart TE, Cai W and Liu Z, ACS Nano, 2015, 9, 950–960. [PubMed: 25562533]
235. Marangoni VS, Neumann O, Henderson L, Kaffes CC, Zhang H, Zhang R, Bishnoi S, Ayala-Orozco C, Zucolotto V, Bankson JA, Nordlander P and Halas NJ, Proc. Natl. Acad. Sci. U. S. A, 2017, 114, 6960–6965. [PubMed: 28630340]
236. Lv R, Yang P, He F, Gai S, Li C, Dai Y, Yang G and Lin J, ACS Nano, 2015, 9, 1630–1647. [PubMed: 25581331]
237. Liu T, Zhang M, Liu W, Zeng X, Song X, Yang X, Zhang X and Feng J, ACS Nano, 2018, 12, 3917–3927. [PubMed: 29578680]
238. Li Y, Hu X, Ding D, Zou Y, Xu Y, Wang X, Zhang Y, Chen L, Chen Z and Tan W, Nat. Commun, 2017, 8, 15653. [PubMed: 28643777]
239. Ju Y, Zhang H, Yu J, Tong S, Tian N, Wang Z, Wang X, Su X, Chu X, Lin J, Ding Y, Li G, Sheng F and Hou Y, ACS Nano, 2017, 11, 9239–9248. [PubMed: 28850218]
240. Yang D, Yang G, Yang P, Lv R, Gai S, Li C, He F and Lin J, Adv. Funct. Mater, 2017, 27, 1700371.
241. Cui J, Jiang R, Guo C, Bai X, Xu S and Wang L, J. Am. Chem. Soc, 2018, 140, 5890–5894. [PubMed: 29676908]
242. Shen Z, Wu A and Chen X, Mol. Pharm, 2017, 14, 1352–1364. [PubMed: 27776215]
243. Deng L, Cai X, Sheng D, Yang Y, Strohm EM, Wang Z, Ran H, Wang D, Zheng Y, Li P, Shang T, Ling Y, Wang F and Sun Y, Theranostics, 2017, 7, 4410–4423. [PubMed: 29158836]
244. Yoon YI, Tang W and Chen X, Small Methods, 2017, 1, 1700173.
245. Tang W, Yang Z, Wang S, Wang Z, Song J, Yu G, Fan W, Dai Y, Wang J, Shan L, Niu G, Fan Q and Chen X, ACS Nano, 2018, 12, 2610–2622. [PubMed: 29451774]
246. Zhou J, Jiang Y, Hou S, Upputuri PK, Wu D, Li J, Wang P, Zhen X, Pramanik M, Pu K and Duan H, ACS Nano, 2018, 12, 2643–2651. [PubMed: 29438610]
247. Yin W, Bao T, Zhang X, Gao Q, Yu J, Dong X, Yan L, Gu Z and Zhao Y, Nanoscale, 2018, 10, 1517–1531. [PubMed: 29303196]
248. Jiang Y, Li J, Zhen X, Xie C and Pu K, Adv. Mater, 2018, 30, e1705980. [PubMed: 29457284]
249. Huo D, Liu S, Zhang C, He J, Zhou Z, Zhang H and Hu Y, ACS Nano, 2017, 11, 10159–10174. [PubMed: 28992409]
250. Vijayaraghavan P, Liu CH, Vankayala R, Chiang CS and Hwang KC, Adv. Mater, 2014, 26, 6689–6695. [PubMed: 25042520]

251. Jain PK, Lee KS, El-Sayed IH and El-Sayed MA, J. Phys. Chem. B, 2006, 110, 7238–7248. [PubMed: 16599493]
252. Liu BJ, Lin KQ, Hu S, Wang X, Lei ZC, Lin HX and Ren B, Anal. Chem, 2015, 87, 1058–1065. [PubMed: 25494875]
253. Near R, Hayden S and El-Sayed M, *J. Phys.* Chem. C., 2012, 116, 23019–23026.
254. Mackey MA, Ali MR, Austin LA, Near RD and El-Sayed MA, J. Phys. Chem. B, 2014, 118, 1319–1326. [PubMed: 24433049]
255. Deng H, Dai F, Ma G and Zhang X, Adv. Mater, 2015, 27, 3645–3653. [PubMed: 25946668]
256. Ayala-Orozco C, Urban C, Knight MW, Urban AS, Neumann O, Bishnoi SW, Mukherjee S, Goodman AM, Charron H, Mitchell T, Shea M, Roy R, Nanda S, Schiff R, Halas NJ and Joshi A, ACS Nano, 2014, 8, 6372–6381. [PubMed: 24889266]
257. Xiao JW, Fan SX, Wang F, Sun LD, Zheng XY and Yan CH, Nanoscale, 2014, 6, 4345–4351. [PubMed: 24622916]
258. Wang Y, Black KC, Luehmann H, Li W, Zhang Y, Cai X, Wan D, Liu SY, Li M, Kim P, Li ZY, Wang LV, Liu Y and Xia Y, ACS Nano, 2013, 7, 2068–2077. [PubMed: 23383982]
259. Lim DK, Barhoumi A, Wylie RG, Reznor G, Langer RS and Kohane DS, Nano Lett, 2013, 13, 4075–4079. [PubMed: 23899267]
260. Song J, Wang F, Yang X, Ning B, Harp MG, Culp SH, Hu S, Huang P, Nie L, Chen J and Chen X, J. Am. Chem. Soc, 2016, 138, 7005–7015. [PubMed: 27193381]
261. Guo B, Sheng Z, Hu D, Li A, Xu S, Manghnani PN, Liu C, Guo L, Zheng H and Liu B, ACS Nano, 2017, 11, 10124–10134. [PubMed: 28892609]
262. Natali M, Campagna S and Scandola F, Chem. Soc. Rev, 2014, 43, 4005–4018. [PubMed: 24604096]
263. Stennett EM, Ciuba MA and Levitus M, Chem. Soc. Rev, 2014, 43, 1057–1075. [PubMed: 24141280]
264. Escudero D, Acc. Chem. Res, 2016, 49, 1816–1824. [PubMed: 27575871]
265. Xu Y, Feng T, Yang T, Wei H, Yang H, Li G, Zhao M, Liu S, Huang W and Zhao Q, ACS Appl. Mater. Interfaces, 2018, 10, 16299–16307. [PubMed: 29676558]
266. Lyu Y, Fang Y, Miao Q, Zhen X, Ding D and Pu K, ACS Nano, 2016, 10, 4472–4481. [PubMed: 26959505]
267. Zhu H, Fang Y, Miao Q, Qi X, Ding D, Chen P and Pu K, ACS Nano, 2017, 11, 8998–9009. [PubMed: 28841279]
268. MacDonald TD, Liu TW and Zheng G, Angew. Chem., Int. Ed, 2014, 53, 6956–6959.
269. Shi J, Tian F, Lyu J and Yang M, J. Mat. Chem. B, 2015, 3, 6989–7005.
270. Song X, Liang C, Gong H, Chen Q, Wang C and Liu Z, Small, 2015, 11, 3932–3941. [PubMed: 25925790]
271. Feng L, Tao D, Dong Z, Chen Q, Chao Y, Liu Z and Chen M, Biomaterials, 2017, 127, 13–24. [PubMed: 28279918]
272. Wurthner F, Kaiser TE and Saha-Moller CR, Angew. Chem., Int. Ed, 2011, 50, 3376–3410.
273. Hochstrasser RM and Kasha M, Photochem. Photobiol, 1964, 3, 317–331.
274. Kasha M, Radiat Res, 1963, 20, 55–70. [PubMed: 14061481]
275. Zou Q, Abbas M, Zhao L, Li S, Shen G and Yan X, J. Am. Chem. Soc, 2017, 139, 1921–1927. [PubMed: 28103663]
276. Deng Y, Huang L, Yang H, Ke H, He H, Guo Z, Yang T, Zhu A, Wu H and Chen H, Small, 2017, 13, 1602747.
277. Jang B, Kim YS and Choi Y, Small, 2010, 7, 265–270. [PubMed: 21213392]
278. Blanco E, Shen H and Ferrari M, Nat. Biotechnol, 2015, 33, 941–951. [PubMed: 26348965]
279. Tong X, Wang Z, Sun X, Song J, Jacobson O, Niu G, Kiesewetter DO and Chen X, Theranostics, 2016, 6, 2039–2051. [PubMed: 27698939]
280. Black KC, Wang Y, Luehmann HP, Cai X, Xing W, Pang B, Zhao Y, Cutler CS, Wang LV, Liu Y and Xia Y, ACS Nano, 2014, 8, 4385–4394. [PubMed: 24766522]

281. Yu Z, Wang M, Pan W, Wang H, Li N and Tang B, Chem. Sci, 2017, 8, 4896–4903. [PubMed: 28959413]
282. Ni D, Jiang D, Valdovinos HF, Ehlerding EB, Yu B, Barnhart TE, Huang P and Cai W, Nano Lett, 2017, 17, 3282–3289. [PubMed: 28418679]
283. Hu X, Yang P, He J, Liang R, Niu D, Wang H and Li Y, J. Mat. Chem. B, 2017, 5, 5931–5936.
284. Zhang C, Bu W, Ni D, Zuo C, Cheng C, Li Q, Zhang L, Wang Z and Shi J, J. Am. Chem. Soc, 2016, 138, 8156–8164. [PubMed: 27264421]
285. Zhang D, Qi GB, Zhao YX, Qiao SL, Yang C and Wang H, Adv. Mater, 2015, 27, 6125–6130. [PubMed: 26350172]
286. Huang P, Gao Y, Lin J, Hu H, Liao HS, Yan X, Tang Y, Jin A, Song J, Niu G, Zhang G, Horkay F and Chen X, ACS Nano, 2015, 9, 9517–9527. [PubMed: 26301492]
287. Liu X, Chen Y, Li H, Huang N, Jin Q, Ren K and Ji J, ACS Nano, 2013, 7, 6244–6257. [PubMed: 23799860]
288. Peng MY, Zheng DW, Wang SB, Cheng SX and Zhang XZ, ACS Appl. Mater. Interfaces, 2017, 9, 13965–13975. [PubMed: 28378999]
289. Korupalli C, Huang CC, Lin WC, Pan WY, Lin PY, Wan WL, Li MJ, Chang Y and Sung HW, Biomaterials, 2017, 116, 1–9. [PubMed: 27912130]
290. Hung CC, Huang WC, Lin YW, Yu TW, Chen HH, Lin SC, Chiang WH and Chiu HC, Theranostics, 2016, 6, 302–317. [PubMed: 26909107]
291. Wang S, Teng Z, Huang P, Liu D, Liu Y, Tian Y, Sun J, Li Y, Ju H, Chen X and Lu G, Small, 2015, 11, 1801–1810. [PubMed: 25565411]
292. Chang Y, Li X, Kong X, Li Y, Liu X, Zhang Y, Tu L, Xue B, Wu F, Cao D, Zhao H and Zhang H, J. Mat. Chem. B, 2015, 3, 8321–8327.
293. Feng L, Li K, Shi X, Gao M, Liu J and Liu Z, Adv. Healthc. Mater, 2014, 3, 1261–1271. [PubMed: 24652715]
294. Zhao R, Han X, Li Y, Wang H, Ji T, Zhao Y and Nie G, ACS Nano, 2017, 11, 8103–8113. [PubMed: 28738680]
295. Kong G, Braun RD and Dewhirst MW, Cancer Res, 2000, 60, 4440–4445. [PubMed: 10969790]
296. Rao L, Bu LL, Ma L, Wang W, Liu H, Wan D, Liu JF, Li A, Guo SS, Zhang L, Zhang WF, Zhao XZ, Sun ZJ and Liu W, Angew. Chem., Int. Ed, 2018, 57, 986–991.
297. Gormley AJ, Larson N, Sadekar S, Robinson R, Ray A and Ghandehari H, Nano Today, 2012, 7, 158–167. [PubMed: 22737178]
298. von Maltzahn G, Park J-H, Lin KY, Singh N, Schwöppe C, Mesters R, Berdel WE, Ruoslahti E, Sailor MJ and Bhatia SN, Nat. Mater, 2011, 10, 545–552. [PubMed: 21685903]
299. Nel AE, Madler L, Velegol D, Xia T, Hoek EM, Somasundaran P, Klaessig F, Castranova V and Thompson M, Nat. Mater, 2009, 8, 543–557. [PubMed: 19525947]
300. Walkey CD, Olsen JB, Guo H, Emili A and Chan WC, J. Am. Chem. Soc, 2012, 134, 2139–2147. [PubMed: 22191645]
301. Pozzi D, Colapicchioni V, Caracciolo G, Piovesana S, Capriotti AL, Palchetti S, De Grossi S, Riccioli A, Amenitsch H and Lagana A, Nanoscale, 2014, 6, 2782–2792. [PubMed: 24463404]
302. Xie C, Zhen X, Miao Q, Lyu Y and Pu K, Adv. Mater, 2018, 30, e1801331. [PubMed: 29611257]
303. Niidome T, Yamagata M, Okamoto Y, Akiyama Y, Takahashi H, Kawano T, Katayama Y and Niidome Y, J. Control. Release, 2006, 114, 343–347. [PubMed: 16876898]
304. Schottler S, Becker G, Winzen S, Steinbach T, Mohr K, Landfester K, Mailander V and Wurm FR, Nat. Nanotechnol, 2016, 11, 372–377. [PubMed: 26878141]
305. Zhou W, Shao J, Jin Q, Wei Q, Tang J and Ji J, Chem. Commun, 2010, 46, 1479–1481.
306. Thapa RK, Ku SK, Choi HG, Yong CS, Byeon JH and Kim JO, Nanoscale, 2018, 10, 1742–1749. [PubMed: 29308494]
307. Piao JG, Gao F, Li YN, Yu L, Liu D, Tan ZB, Xiong YJ, Yang LH and You YZ, Nano Res, 2018, 11, 3193–3204.
308. Khunsuk PO, Chawalitpong S, Sawutdeechaikul P, Palaga T and Hoven VP, Mol. Pharm, 2018, 15, 164–174. [PubMed: 29185337]

309. Jiang H, Chen D, Guo D, Wang N, Su Y, Jin X, Tong G and Zhu X, Biomater. Sci, 2017, 5, 686–697. [PubMed: 28165076]
310. Deng W, Wu Q, Sun P, Yuan P, Lu X, Fan Q and Huang W, Polym. Chem, 2018, 9, 2805–2812.
311. Li Z, Zhang H, Han J, Chen Y, Lin H and Yang T, Adv. Mater, 2018, 30, e1706981. [PubMed: 29663543]
312. Liang X, Fang L, Li X, Zhang X and Wang F, Biomaterials, 2017, 132, 72–84. [PubMed: 28411450]
313. Jang C, Lee JH, Sahu A and Tae G, Nanoscale, 2015, 7, 18584–18594. [PubMed: 26489965]
314. Wilhelm S, Tavares AJ, Dai Q, Ohta S, Audet J, Dvorak HF and Chan WCW, Nat. Rev. Mater, 2016, 1, 16014.
315. Sykes EA, Chen J, Zheng G and Chan WC, ACS Nano, 2014, 8, 5696–5706. [PubMed: 24821383]
316. Hu CM, Zhang L, Aryal S, Cheung C, Fang RH and Zhang L, Proc. Natl. Acad. Sci. U. S. A, 2011, 108, 10980–10985. [PubMed: 21690347]
317. Hu CM, Fang RH, Wang KC, Luk BT, Thamphiwatana S, Dehaini D, Nguyen P, Angsantikul P, Wen CH, Kroll AV, Carpenter C, Ramesh M, Qu V, Patel SH, Zhu J, Shi W, Hofman FM, Chen TC, Gao W, Zhang K, Chien S and Zhang L, Nature, 2015, 526, 118–121. [PubMed: 26374997]
318. Zhang N, Li M, Sun X, Jia H and Liu W, Biomaterials, 2018, 159, 25–36. [PubMed: 29309991]
319. Sun H, Su J, Meng Q, Yin Q, Chen L, Gu WW, Zhang Z, Yu H, Zhang P, Wang S and Li Y, Adv. Funct. Mater, 2017, 27, 1604300.
320. Meng QF, Rao L, Zan M, Chen M, Yu GT, Wei X, Wu Z, Sun Y, Guo SS, Zhao XZ, Wang FB and Liu W, Nanotechnology, 2018, 29, 134004. [PubMed: 29334363]
321. Xuan M, Shao J, Dai L, Li J and He Q, ACS Appl. Mater. Interfaces, 2016, 8, 9610–9618. [PubMed: 27039688]
322. Wan G, Chen B, Li L, Wang D, Shi S, Zhang T, Wang Y, Zhang L and Wang Y, Biomaterials, 2018, 155, 25–40. [PubMed: 29161627]
323. Zhu DM, Xie W, Xiao YS, Suo M, Zan MH, Liao QQ, Hu XJ, Chen LB, Chen B, Wu WT, Ji LW, Huang HM, Guo SS, Zhao XZ, Liu QY and Liu W, Nanotechnology, 2018, 29, 084002. [PubMed: 29339567]
324. Rao L, Cai B, Bu LL, Liao QQ, Guo SS, Zhao XZ, Dong WF and Liu W, ACS Nano, 2017, 11, 3496–3505. [PubMed: 28272874]
325. Jiang Q, Luo Z, Men Y, Yang P, Peng H, Guo R, Tian Y, Pang Z and Yang W, Biomaterials, 2017, 143, 29–45. [PubMed: 28756194]
326. Chen W, Zeng K, Liu H, Ouyang J, Wang L, Liu Y, Wang H, Deng L and Liu YN, Adv. Funct. Mater, 2017, 27, 1605795.
327. Ren X, Zheng R, Fang X, Wang X, Zhang X, Yang W and Sha X, Biomaterials, 2016, 92, 13–24. [PubMed: 27031929]
328. Li J, Zhen X, Lyu Y, Jiang Y, Huang J and Pu K, ACS Nano, 2018, 12, 8520–8530. [PubMed: 30071159]
329. Geng Y, Dalhaimer P, Cai S, Tsai R, Tewari M, Minko T and Discher DE, Nat. Nanotechnol, 2007, 2, 249–255. [PubMed: 18654271]
330. Zhang S, Gao H and Bao G, ACS Nano, 2015, 9, 8655–8671. [PubMed: 26256227]
331. Chithrani BD, Ghazani AA and Chan WC, Nano Lett, 2006, 6, 662–668. [PubMed: 16608261]
332. Li Z, Huang H, Tang S, Li Y, Yu XF, Wang H, Li P, Sun Z, Zhang H, Liu C and Chu PK, Biomaterials, 2016, 74, 144–154. [PubMed: 26454052]
333. Robinson R, Gerlach W and Ghandehari H, J. Control. Release, 2015, 220, 245–252. [PubMed: 26526969]
334. Arnida Janat-Amsbury MM, Ray A, Peterson CM and Ghandehari H, Eur. J. Pharm. Biopharm, 2011, 77, 417–423. [PubMed: 21093587]
335. Chen X, Li J, Huang Y, Wei J, Sun D and Zheng N, Biomater. Sci, 2017, 5, 2448–2455. [PubMed: 29082412]

336. Webb BA, Chimenti M, Jacobson MP and Barber DL, Nat. Rev. Cancer, 2011, 11, 671–677. [PubMed: 21833026]
337. Kong G, Braun RD and Dewhirst MW, Cancer Res, 2001, 61, 3027–3032. [PubMed: 11306483]
338. Raeesi V and Chan WC, Nanoscale, 2016, 8, 12524–12530. [PubMed: 26822539]
339. Chatterjee DK, Diagaradjane P and Krishnan S, Ther. Deliv, 2011, 2, 1001–1014. [PubMed: 22506095]
340. Diagaradjane P, Shetty A, Wang JC, Elliott AM, Schwartz J, Shentu S, Park HC, Deorukhkar A, Stafford RJ, Cho SH, Tunnell JW, Hazle JD and Krishnan S, Nano Lett, 2008, 8, 1492–1500. [PubMed: 18412402]
341. Li J, Xie C, Huang J, Jiang Y, Miao Q and Pu K, Angew. Chem., Int. Ed, 2018, 57, 3995–3998.
342. Su YL, Chen KT, Sheu YC, Sung SY, Hsu RS, Chiang CS and Hu SH, ACS Nano, 2016, 10, 9420–9433. [PubMed: 27684199]
343. Lu N, Huang P, Fan W, Wang Z, Liu Y, Wang S, Zhang G, Hu J, Liu W, Niu G, Leapman RD, Lu G and Chen X, Biomaterials, 2017, 126, 39–48. [PubMed: 28254692]
344. Li Y, Ding J, Zhu J, Tian H and Chen X, Biomacromolecules, 2018, 19, 1950–1958. [PubMed: 29381337]
345. Rahoui N, Jiang B, Taloub N and Huang YD, J. Control. Release, 2017, 255, 176–201. [PubMed: 28408201]
346. Goodman AM, Neumann O, Norregaard K, Henderson L, Choi MR, Clare SE and Halas NJ, Proc. Natl. Acad. Sci. U. S. A, 2017, 114, 12419–12424. [PubMed: 29109274]
347. Vo-Dinh T and Inman BA, Nanomedicine, 2018, 13, 139–144. [PubMed: 29231126]
348. Zhang M, Liu E, Cui Y and Huang Y, Cancer. Biol. Med, 2017, 14, 212–227. [PubMed: 28884039]
349. Dong X, Yin W, Zhang X, Zhu S, He X, Yu J, Xie J, Guo Z, Yan L, Liu X, Wang Q, Gu Z and Zhao Y, ACS Appl. Mater. Interfaces, 2018, 10, 4271–4284. [PubMed: 29318879]
350. Li Y, Deng Y, Tian X, Ke H, Guo M, Zhu A, Yang T, Guo Z, Ge Z, Yang X and Chen H, ACS Nano, 2015, 9, 9626–9637. [PubMed: 26365698]
351. Yu G, Yang Z, Fu X, Yung BC, Yang J, Mao Z, Shao L, Hua B, Liu Y, Zhang F, Fan Q, Wang S, Jacobson O, Jin A, Gao C, Tang X, Huang F and Chen X, Nat. Commun, 2018, 9, 766. [PubMed: 29472567]
352. Yang J, Su H, Sun W, Cai J, Liu S, Chai Y and Zhang C, Theranostics, 2018, 8, 1966–1984. [PubMed: 29556368]
353. Li L, Lu Y, Jiang C, Zhu Y, Yang X, Hu X, Lin Z, Zhang Y, Peng M, Xia H and Mao C, Adv. Funct. Mater, 2018, 28, 1704623. [PubMed: 29706855]
354. Li N, Sun Q, Yu Z, Gao X, Pan W, Wan X and Tang B, ACS Nano, 2018, 12, 5197–5206.
355. Jiang Y, Cui D, Fang Y, Zhen X, Upputuri PK, Pramanik M, Ding D and Pu K, Biomaterials, 2017, 145, 168–177. [PubMed: 28866477]
356. Chen Q, Xu L, Liang C, Wang C, Peng R and Liu Z, Nat. Commun, 2016, 7, 13193. [PubMed: 27767031]
357. Nam J, Son S, Ochyl LJ, Kuai R, Schwendeman A and Moon JJ, Nat. Commun, 2018, 9, 1074. [PubMed: 29540781]
358. Conde J, Oliva N, Zhang Y and Artzi N, Nat. Mater, 2016, 15, 1128–1138. [PubMed: 27454043]
359. Jung BK, Lee YK, Hong J, Ghandehari H and Yun CO, ACS Nano, 2016, 10, 10533–10543. [PubMed: 27805805]
360. Wang BK, Yu XF, Wang JH, Li ZB, Li PH, Wang H, Song L, Chu PK and Li C, Biomaterials, 2016, 78, 27–39. [PubMed: 26646625]
361. Wang S, Tian Y, Tian W, Sun J, Zhao S, Liu Y, Wang C, Tang Y, Ma X, Teng Z and Lu G, ACS Nano, 2016, 10, 8578–8590. [PubMed: 27576159]
362. Ni Q, Teng Z, Dang M, Tian Y, Zhang Y, Huang P, Su X, Lu N, Yang Z, Tian W, Wang S, Liu W, Tang Y, Lu G and Zhang L, Nanoscale, 2017, 9, 1466–1474. [PubMed: 28066849]
363. Cheng W, Nie J, Gao N, Liu G, Tao W, Xiao X, Jiang L, Liu Z, Zeng X and Mei L, Adv. Funct. Mater, 2017, 27, 1704135.

364. Chen X, Zhang Q, Li J, Yang M, Zhao N and Xu FJ, ACS Nano, 2018, 12, 5646–5656.
365. Huang S, Liu Y, Xu X, Ji M, Li Y, Song C, Duan S and Hu Y, J. Mat. Chem. B, 2018, 6, 2217–2229.
366. Wang H, Zhong L, Liu Y, Xu X, Xing C, Wang M, Bai SM, Lu CH and Yang HH, Chem. Commun, 2018, 54, 3142–3145.
367. Chen G, Ding L, Wu P, Zhou Y, Sun M, Wang K and Oupický D, Polym. Adv. Technol, 2018, DOI: 10.1002/pat.4372.
368. Kim J, Kim J, Jeong C and Kim WJ, Adv. Drug Deliv. Rev, 2016, 98, 99–112. [PubMed: 26748259]
369. Lyu Y, Cui D, Sun H, Miao Y, Duan H and Pu K, Angew. Chem., Int. Ed, 2017, 56, 9155–9159.
370. Gong H, Dong Z, Liu Y, Yin S, Cheng L, Xi W, Xiang J, Liu K, Li Y and Liu Z, Adv. Funct. Mater, 2014, 24, 6492–6502.
371. Tian B, Wang C, Zhang S, Feng L and Liu Z, ACS Nano, 2011, 5, 7000–7009. [PubMed: 21815655]
372. Liu Y, Zhen W, Jin L, Zhang S, Sun G, Zhang T, Xu X, Song S, Wang Y, Liu J and Zhang H, ACS Nano, 2018, 12, 4886–4893. [PubMed: 29727164]
373. Yang D, Yang G, Yang P, Lv R, Gai S, Li C, He F and Lin J, Adv. Funct. Mater, 2017, 27, 14.
374. Yang T, Liu L, Deng Y, Guo Z, Zhang G, Ge Z, Ke H and Chen H, Adv. Mater, 2017, 29, 1700487.
375. Ye S, Rao J, Qiu S, Zhao J, He H, Yan Z, Yang T, Deng Y, Ke H, Yang H, Zhao Y, Guo Z and Chen H, Adv. Mater, 2018, 30, e1801216.
376. Tang Q, Xiao W, Huang C, Si W, Shao J, Huang W, Chen P, Zhang Q and Dong XC, Chem. Mater, 2017, 29, 5216–5224.
377. Fan W, Yung B, Huang P and Chen X, Chem. Rev, 2017, 117, 13566–13638. [PubMed: 29048884]
378. Cai Y, Si W, Huang W, Chen P, Shao J and Dong X, Small, 2018, 14, e1704247. [PubMed: 29611290]
379. Zhu H, Cheng P, Chen P and Pu K, Biomater. Sci, 2018, 6, 746–765. [PubMed: 29485662]
380. Gao F, Sun M, Xu L, Liu L, Kuang H and Xu C, Adv. Funct. Mater, 2017, 27, 6.
381. Shen S, Zhu C, Huo D, Yang M, Xue J and Xia Y, Angew. Chem., Int. Ed, 2017, 56, 8801–8804.
382. Wang XQ, Gao F and Zhang XZ, Angew. Chem., Int. Ed, 2017, 56, 9029–9033.
383. Huang Y, Qiu F, Shen L, Chen D, Su Y, Yang C, Li B, Yan D and Zhu X, ACS Nano, 2016, 10, 10489–10499. [PubMed: 27792300]
384. Li X, Kim CY, Lee S, Lee D, Chung HM, Kim G, Heo SH, Kim C, Hong KS and Yoon J, J. Am. Chem. Soc, 2017, 139, 10880–10886. [PubMed: 28708389]
385. Xiao Q, Zheng X, Bu W, Ge W, Zhang S, Chen F, Xing H, Ren Q, Fan W, Zhao K, Hua Y and Shi J, J. Am. Chem. Soc, 2013, 135, 13041–13048. [PubMed: 23924214]
386. Wang S, Li X, Chen Y, Cai X, Yao H, Gao W, Zheng Y, An X, Shi J and Chen H, Adv. Mater, 2015, 27, 2775–2782. [PubMed: 25821185]
387. Yong Y, Cheng X, Bao T, Zu M, Yan L, Yin W, Ge C, Wang D, Gu Z and Zhao Y, ACS Nano, 2015, 9, 12451–12463. [PubMed: 26495962]
388. Ma N, Jiang YW, Zhang X, Wu H, Myers JN, Liu P, Jin H, Gu N, He N, Wu FG and Chen Z, ACS Appl. Mater. Interfaces, 2016, 8, 28480–28494. [PubMed: 27689441]
389. Mao F, Wen L, Sun C, Zhang S, Wang G, Zeng J, Wang Y, Ma J, Gao M and Li Z, ACS Nano, 2016, 10, 11145–11155. [PubMed: 28024338]
390. Liu X, Zhang X, Zhu M, Lin G, Liu J, Zhou Z, Tian X and Pan Y, ACS Appl. Mater. Interfaces, 2017, 9, 279–285. [PubMed: 27966883]
391. Song X, Liang C, Feng L, Yang K and Liu Z, Biomater. Sci, 2017, 5, 1828–1835. [PubMed: 28660918]
392. Yu X, Li A, Zhao C, Yang K, Chen X and Li W, ACS Nano, 2017, 11, 3990–4001. [PubMed: 28395135]

393. Wang S, Chi C, Cheng H, Pan X, Li S, Zhang F, Gaowa S, Ye J, Mao Y, He K, Tian J and Liu H, Small Methods, 2018, 2, 1700368.

394. Wang S, Ma X, Hong X, Cheng Y, Tian Y, Zhao S, Liu W, Tang Y, Zhao R, Song L, Teng Z and Lu G, ACS Nano, 2018, 12, 662–670. [PubMed: 29271636]

395. Yi X, Yang K, Liang C, Zhong X, Ning P, Song G, Wang D, Ge C, Chen C, Chai Z and Liu Z, Adv. Funct. Mater, 2015, 25, 4689–4699.

396. Upputuri PK and Pramanik M, J. Biomed. Opt, 2017, 22, 41006. [PubMed: 27893078]

397. Wang LV and Hu S, Science, 2012, 335, 1458–1462. [PubMed: 22442475]

398. Omar M, Schwarz M, Soliman D, Symvoulidis P and Ntziachristos V, Neoplasia, 2015, 17, 208–214. [PubMed: 25748240]

399. Yao DK, Maslov K, Shung KK, Zhou Q and Wang LV, Opt. Lett, 2010, 35, 4139–4141. [PubMed: 21165116]

400. Zhang HF, Maslov K, Stoica G and Wang LV, Nat. Biotechnol, 2006, 24, 848–851. [PubMed: 16823374]

401. Nasiriavanaki M, Xia J, Wan H, Bauer AQ, Culver JP and Wang LV, Proc. Natl. Acad. Sci. U. S. A, 2014, 111, 21–26. [PubMed: 24367107]

402. Gottschalk S, Fehm TF, Dean-Ben XL and Razansky D, J. Cereb. Blood Flow Metab, 2015, 35, 531–535. [PubMed: 25586142]

403. Weber J, Beard PC and Bohndiek SE, Nat. Methods, 2016, 13, 639–650. [PubMed: 27467727]

404. Kang JH and Chung JK, J. Nucl. Med, 2008, 49 Suppl 2, 164S-179S.

405. Yao J, Kaberniuk AA, Li L, Shcherbakova DM, Zhang R, Wang L, Li G, Verkhusha VV and Wang LV, Nat. Methods, 2016, 13, 67–73. [PubMed: 26550774]

406. Tzoumas S, Deliolanis N, Morscher S and Ntziachristos V, IEEE Trans. Med. Imaging, 2014, 33, 48–60. [PubMed: 24001986]

407. Taruttis A and Ntziachristos V, Nat. Photonics, 2015, 9, 219–227.

408. Dean-Ben XL, Gottschalk S, Mc Larney B, Shoham S and Razansky D, Chem. Soc. Rev, 2017, 46, 2158–2198. [PubMed: 28276544]

409. Kim C, Favazza C and Wang LV, Chem. Rev, 2010, 110, 2756–2782. [PubMed: 20210338]

410. Cheng X, Sun R, Yin L, Chai Z, Shi H and Gao M, Adv. Mater, 2017, 29, 1604894.

411. Jokerst JV, Cole AJ, Van de Sompel D and Gambhir SS, ACS Nano, 2012, 6, 10366–10377. [PubMed: 23101432]

412. De la Zerda A, Zavaleta C, Keren S, Vaithilingam S, Bodapati S, Liu Z, Levi J, Smith BR, Ma TJ, Oralkan O, Cheng Z, Chen X, Dai H, Khuri-Yakub BT and Gambhir SS, Nat. Nanotechnol, 2008, 3, 557–562. [PubMed: 18772918]

413. Homan KA, Souza M, Truby R, Luke GP, Green C, Vreeland E and Emelianov S, ACS Nano, 2012, 6, 641–650. [PubMed: 22188516]

414. Xi L, Grobmyer SR, Zhou G, Qian W, Yang L and Jiang H, J. Biophotonics, 2014, 7, 401–409. [PubMed: 23125139]

415. Li PC, Wang CR, Shieh DB, Wei CW, Liao CK, Poe C, Jhan S, Ding AA and Wu YN, Opt. Express, 2008, 16, 18605–18615. [PubMed: 19581946]

416. de la Zerda A, Liu Z, Bodapati S, Teed R, Vaithilingam S, Khuri-Yakub BT, Chen X, Dai H and Gambhir SS, Nano Lett, 2010, 10, 2168–2172. [PubMed: 20499887]

417. Agarwal A, Huang SW, O'Donnell M, Day KC, Day M, Kotov N and Ashkenazi S, J. Appl. Phys, 2007, 102, 064701.

418. Xie C, Upputuri PK, Zhen X, Pramanik M and Pu K, Biomaterials, 2017, 119, 1–8. [PubMed: 27988405]

419. de la Zerda A, Bodapati S, Teed R, May SY, Tabakman SM, Liu Z, Khuri-Yakub BT, Chen X, Dai H and Gambhir SS, ACS Nano, 2012, 6, 4694–4701. [PubMed: 22607191]

420. Chen YS, Frey W, Kim S, Kruizinga P, Homan K and Emelianov S, Nano Lett, 2011, 11, 348–354. [PubMed: 21244082]

421. Zhen X, Feng X, Xie C, Zheng Y and Pu K, Biomaterials, 2017, 127, 97–106. [PubMed: 28284105]

422. Park JH, Dumani DS, Arsiwala A, Emelianov S and Kane RS, Nanoscale, 2018, 10, 15365–15370. [PubMed: 30083665]
423. Karaman S and Detmar M, J. Clin. Invest, 2014, 124, 922–928. [PubMed: 24590277]
424. Song KH, Kim C, Cobley CM, Xia Y and Wang LV, Nano Lett, 2009, 9, 183–188. [PubMed: 19072058]
425. Pan D, Cai X, Yalaz C, Senpan A, Omanakuttan K, Wickline SA, Wang LV and Lanza GM, ACS Nano, 2012, 6, 1260–1267. [PubMed: 22229462]
426. Kim C, Song KH, Gao F and Wang LV, Radiology, 2010, 255, 442–450. [PubMed: 20413757]
427. Akers WJ, Kim C, Berezin M, Guo K, Fuhrhop R, Lanza GM, Fischer GM, Daltrozzo E, Zumbusch A, Cai X, Wang LV and Achilefu S, ACS Nano, 2011, 5, 173–182. [PubMed: 21171567]
428. Galanzha EI, Shashkov EV, Kelly T, Kim JW, Yang L and Zharov VP, Nat. Nanotechnol, 2009, 4, 855–860. [PubMed: 19915570]
429. Strohm EM, Berndl ES and Kolios MC, Biophys. J, 2013, 105, 59–67. [PubMed: 23823224]
430. Hsu HC, Wang L and Wang LV, J. Biomed. Opt, 2016, 21, 56004. [PubMed: 27207113]
431. Kunjachan S, Ehling J, Storm G, Kiessling F and Lammers T, Chem. Rev, 2015, 115, 10907–10937. [PubMed: 26166537]
432. Hsu PP and Sabatini DM, Cell, 2008, 134, 703–707. [PubMed: 18775299]
433. Kato Y, Ozawa S, Miyamoto C, Maehata Y, Suzuki A, Maeda T and Baba Y, Cancer. Cell. Int, 2013, 13, 89. [PubMed: 24004445]
434. Miao Q, Lyu Y, Ding D and Pu K, Adv. Mater, 2016, 28, 3662–3668. [PubMed: 27000431]
435. Duan Z, Gao YJ, Qiao ZY, Fan G, Liu Y, Zhang D and Wang H, *J. Mater. Chem.* B, 2014, 2, 6271–6282.
436. Wu X, Lin B, Yu M, Yang L, Han J and Han S, Chem. Sci, 2015, 6, 2002–2009. [PubMed: 28706650]
437. Gerling M, Zhao Y, Nania S, Norberg KJ, Verbeke CS, Englert B, Kuiper RV, Bergstrom A, Hassan M, Neesse A, Lohr JM and Heuchel RL, Theranostics, 2014, 4, 604–613. [PubMed: 24723982]
438. Tzoumas S, Nunes A, Olefir I, Stangl S, Symvoulidis P, Glasl S, Bayer C, Multhoff G and Ntziachristos V, Nat. Commun, 2016, 7, 12121. [PubMed: 27358000]
439. Jo J, Lee CH, Kopelman R and Wang X, Nat. Commun, 2017, 8, 471. [PubMed: 28883396]
440. Pu K, Shuhendler AJ, Jokerst JV, Mei J, Gambhir SS, Bao Z and Rao J, Nat. Nanotechnol, 2014, 9, 233–239. [PubMed: 24463363]
441. Yin C, Zhen X, Fan Q, Huang W and Pu K, ACS Nano, 2017, 11, 4174–4182. [PubMed: 28296388]
442. Zhang J, Zhen X, Upputuri PK, Pramanik M, Chen P and Pu K, Adv. Mater, 2017, 29, 1604764.
443. Yang K, Zhu L, Nie L, Sun X, Cheng L, Wu C, Niu G, Chen X and Liu Z, Theranostics, 2014, 4, 134–141. [PubMed: 24465271]
444. Miao Q and Pu K, Bioconjug. Chem, 2016, 27, 2808–2823. [PubMed: 27998078]
445. Yang J, Gupta V, Tallman KA, Porter NA, Carroll KS and Liebler DC, Nat. Protoc, 2015, 10, 1022–1037. [PubMed: 26086405]
446. Seo YH and Carroll KS, Proc. Natl. Acad. Sci. U. S. A, 2009, 106, 16163–16168. [PubMed: 19805274]
447. Lyu Y, Zhen X, Miao Y and Pu K, ACS Nano, 2017, 11, 358–367. [PubMed: 27997794]
448. Knox HJ, Hedhli J, Kim TW, Khalili K, Dobrucki LW and Chan J, Nat. Commun, 2017, 8, 1794. [PubMed: 29176550]
449. Huynh E, Lovell JF, Helfield BL, Jeon M, Kim C, Goertz DE, Wilson BC and Zheng G, J. Am. Chem. Soc, 2012, 134, 16464–16467. [PubMed: 22827774]
450. Tay LM and Xu C, Nanomedicine, 2017, 12, 91–94. [PubMed: 27876447]
451. Oddo L, Cerroni B, Domenici F, Bedini A, Bordi F, Chiessi E, Gerbes S and Paradossi G, J. Colloid Interface Sci, 2017, 491, 151–160. [PubMed: 28024192]

452. Toumia Y, Domenici F, Orlanducci S, Mura F, Grishenkov D, Trochet P, Lacerenza S, Bordi F and Paradossi G, ACS Appl. Mater. Interfaces, 2016, 8, 16465–16475. [PubMed: 27269868]

453. Dixon AJ, Hu S, Klibanov AL and Hossack JA, Small, 2015, 11, 3066–3077. [PubMed: 25703465]

454. Huynh E, Leung BY, Helfield BL, Shakiba M, Gandier JA, Jin CS, Master ER, Wilson BC, Goertz DE and Zheng G, Nat. Nanotechnol, 2015, 10, 325–332. [PubMed: 25822929]

455. Paproski RJ, Forbrich A, Huynh E, Chen J, Lewis JD, Zheng G and Zemp RJ, Small, 2016, 12, 371–380. [PubMed: 26633744]

456. Hannah A, Luke G, Wilson K, Homan K and Emelianov S, ACS Nano, 2014, 8, 250–259. [PubMed: 24303934]

457. Li DS, Yoon SJ, Pelivanov I, Frenz M, O'Donnell M and Pozzo LD, Nano Lett, 2017, 17, 6184–6194. [PubMed: 28926276]

458. Qi J, Chen C, Zhang X, Hu X, Ji S, Kwok RTK, Lam JWY, Ding D and Tang BZ, Nat. Commun, 2018, 9, 1848. [PubMed: 29748611]

459. Jiang Y, Upputuri PK, Xie C, Lyu Y, Zhang L, Xiong Q, Pramanik M and Pu K, Nano Lett, 2017, 17, 4964–4969. [PubMed: 28654292]

460. Wu J, You L, Lan L, Lee HJ, Chaudhry ST, Li R, Cheng JX and Mei J, Adv. Mater, 2017, 29, 1703403.

461. Guo B, Sheng Z, Kenry DH Hu X Lin W, Xu S, Liu C, Zheng H and Liu B, Mater. Horiz, 2017, 4, 1151–1156.

462. Chen Y, Yoon S, Frey W, Dockery M and Emelianov S, Nat. Commun, 2017, 8, 15782. [PubMed: 28593942]

463. Repenko T, Rix A, Ludwanowski S, Go D, Kiessling F, Lederle W and Kuehne AJC, Nat. Commun, 2017, 8, 470. [PubMed: 28883395]

464. Dawidczyk CM, Russell LM and Searson PC, Cancer Res, 2015, canres. 1558.2015.

465. Yun SH and Kwok SJ, Nat. Biomed. Eng, 2017, 1, 0008. [PubMed: 28649464]

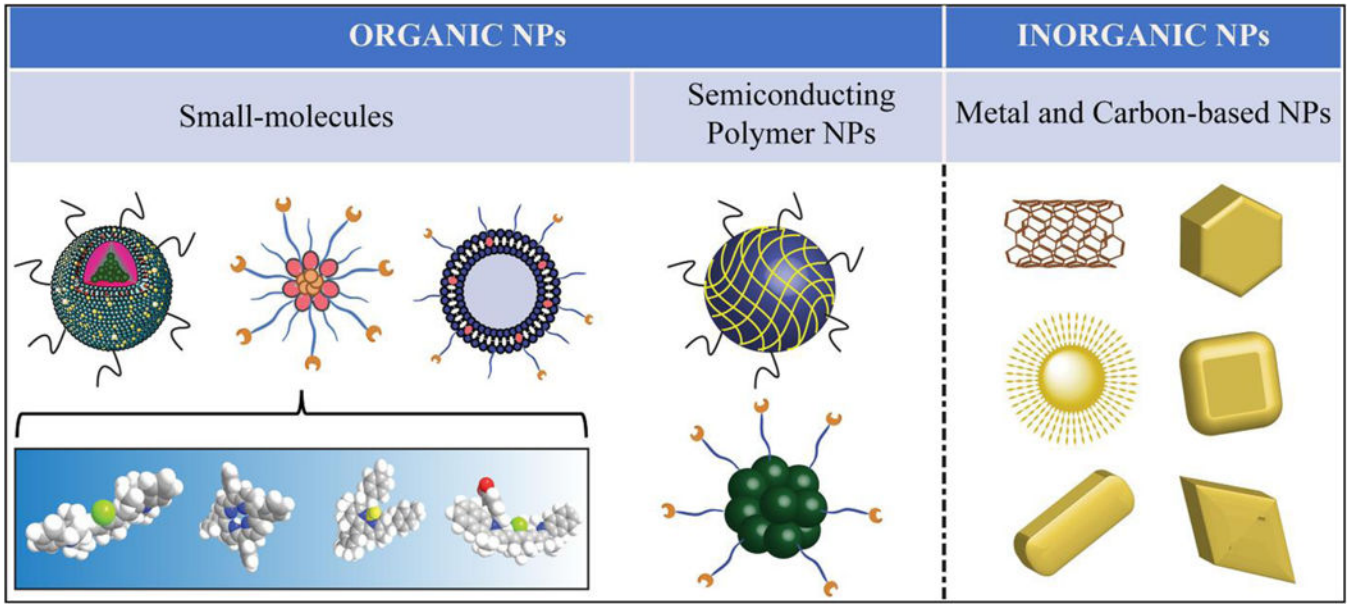

Figure 1.
Classification of nano photothermal transduction agents.

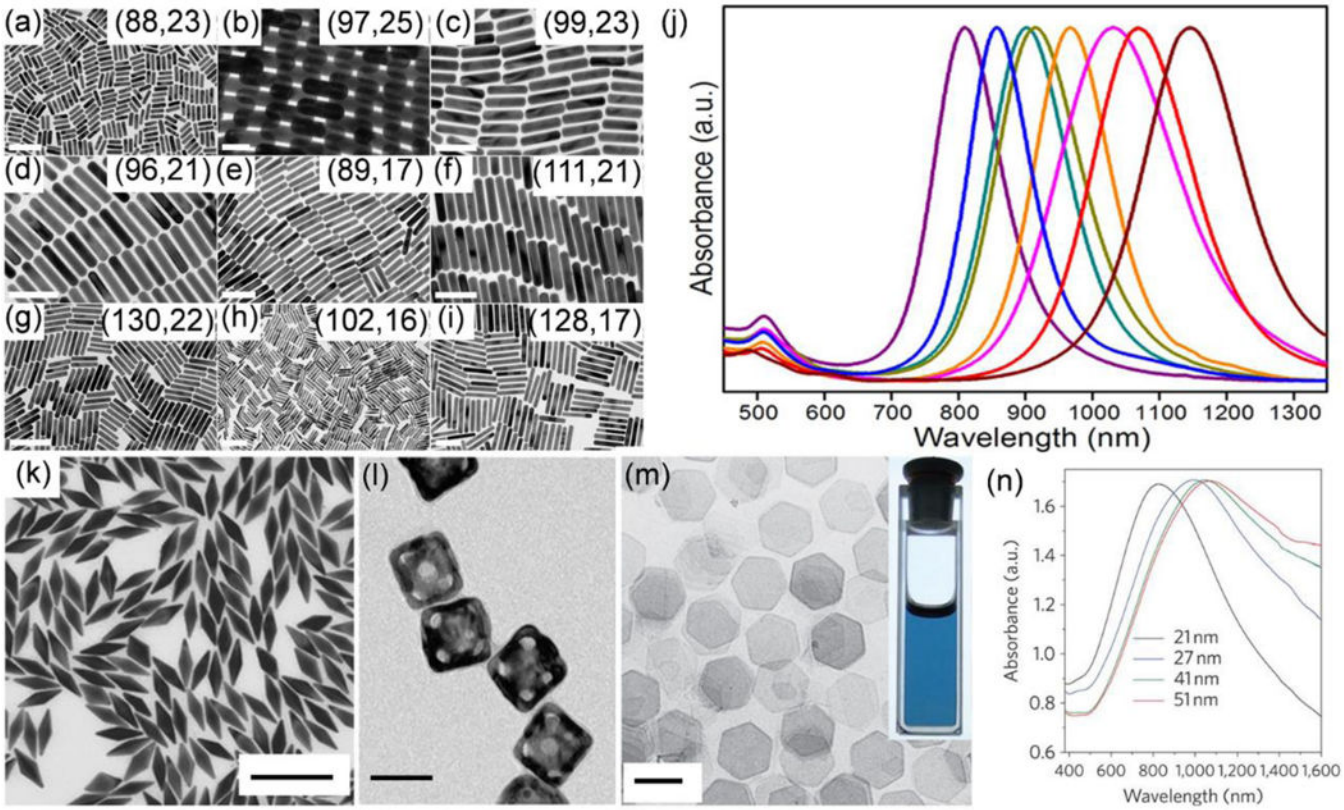

Figure 2.

(a-i) TEM images of Au nanorods synthesized using both CTAB and sodium oleate as ligands in the order of increased aspect ratio from a to i. Scar bars: (a) 200 nm, (b) 50 nm, (c–f) 100 nm, (g–h) 200 nm, and (i) 100 nm. The numbers in the insets represent the average length and width (nm) of each sample measured from TEM images. (j) From left to right are the normalized extinction spectra of Au nanorods corresponding to sample a, c, d, e, f, g, h, and i, respectively. Reproduced from reference 80 with permission from American Chemical Society, copyright 2013. (k) TEM image of Au nanobipyramids. Scar bar: 200 nm. Reproduced from reference 90 with permission from Wiley-VCH, copyright 2015. (l) TEM image of Au nanocages modified with modified by thermal sensitive polymers. Scar bar: 50 nm. Reproduced from reference 102 with permission from Springer Nature, copyright 2009. (m) TEM image of the Pd nanosheets. Scar bar: 100 nm. Inset is a picture of an ethanol dispersion of the Pd nanosheets in a cuvette. (n) The extinction spectra of Pd nanosheets with different edge lengths. Reproduced from reference 103 with permission from Springer Nature, copyright 2011.

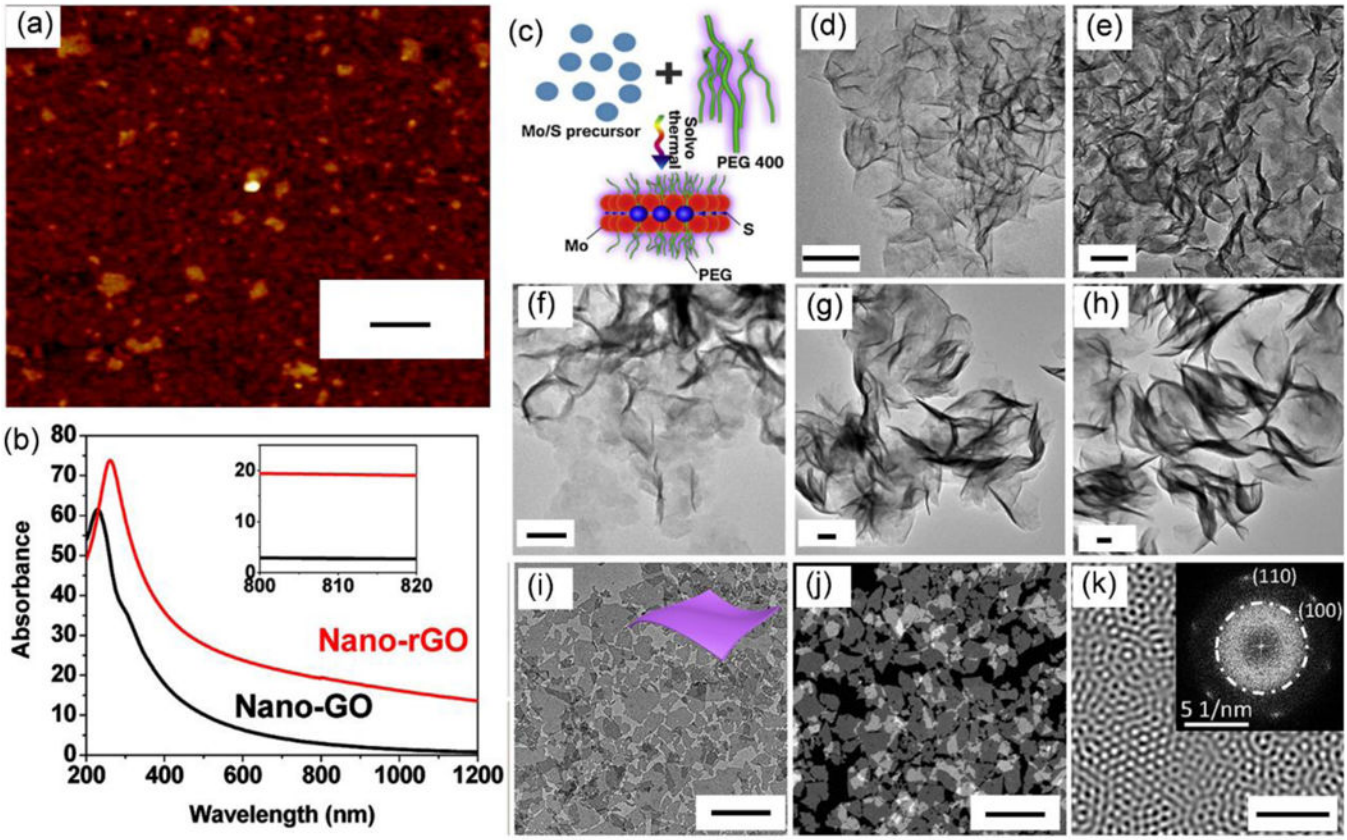

Figure 3.

(a) AFM image of reduced graphene oxide. Scale bar: 50 nm. (b) The absorption spectra of graphene oxide (black) and reduced graphene oxide (red). The inset is the zoom-in absorption spectra in the range between 800 and 820 nm. Reproduced from reference 120 with permission from American Chemical Society, copyright 2011. (c) Schematic illustration of the synthesis of MoS_2 nanosheets *via* solvothermal method and (d-h) TEM images of MoS_2 nanosheets with piece diameter of 50.4, 79.2, 103.1, 194.9, and 297.5 nm, respectively. Scale bars: 50 nm. Reproduced from reference 124 with permission from Elsevier Ltd, copyright 2015. (i) TEM image, (j) dark-field TEM image, and (k) Fourier transform patterns of ultrathin Nb_2C nanosheets. The inset of k is the original SAED pattern. Scar bars: (i,j) 200 nm and (k) 5 nm. Reproduced from reference 127 with permission from American Chemical Society, copyright 2017

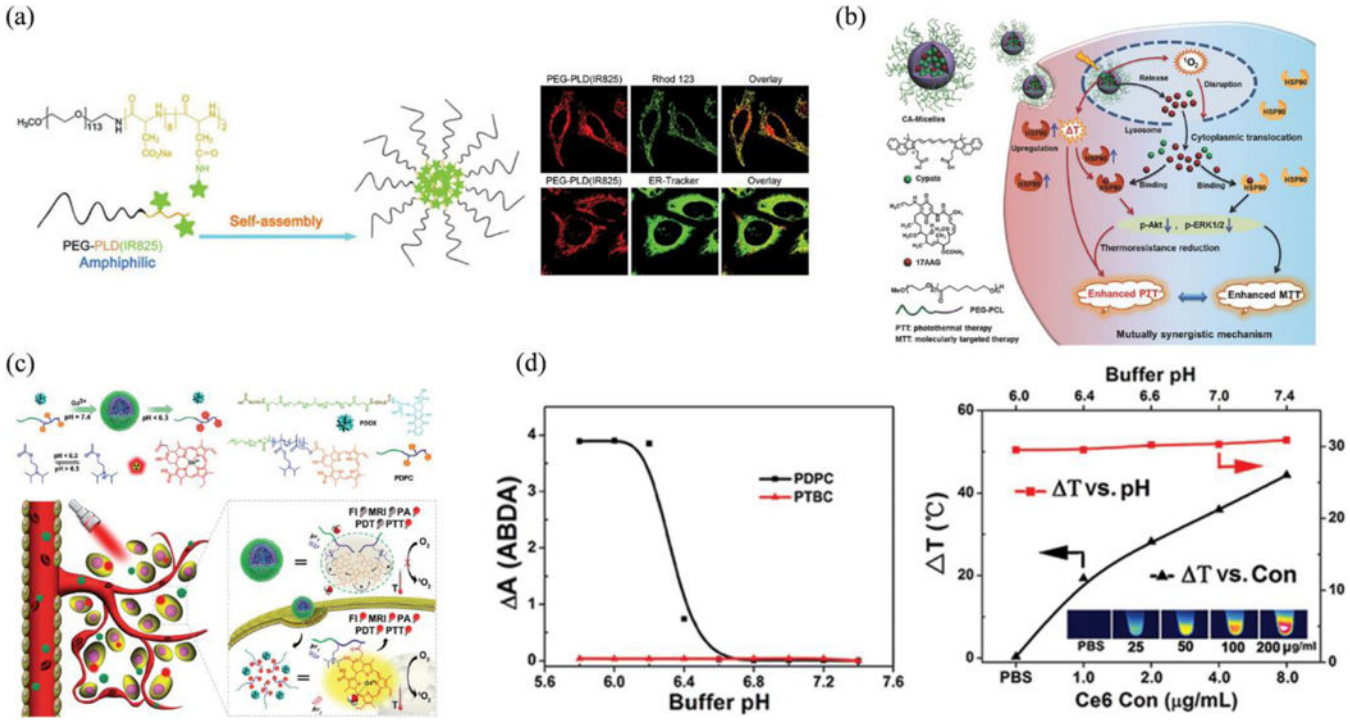

Figure 4:

(a) Schematic illustration of the synthesis of the PEG-PLD(IR825) nanomicelle-based PTT and confocal images of nanomicelles-treated HeLa cells after staining with Rhod 123 and ER-Tracker Green, respectively. Reproduced from reference 155 with permission from Royal Society of Chemistry, copyright 2018. (b) Illustration of the micelles with mutually synergistic molecularly targeted therapy/PTT for highly potent cancer therapy. Reproduced from reference 156 with permission from Wiley, copyright 2017. (c) Illustration for self-assembly and structural composition of the acid-switchable micelles (PDPC) for multimodal imaging and combinational therapy of drug-resistant tumour. (d) ROS generation and photothermal profile of PDPC micelles vs Ce6 concentration under 655 nm laser irradiation (black curve, pH 7.4) or pH value (red curve, Ce6 concentration 50 μg/mL) Reproduced from reference 173 with permission from American Chemical Society, copyright 2016.

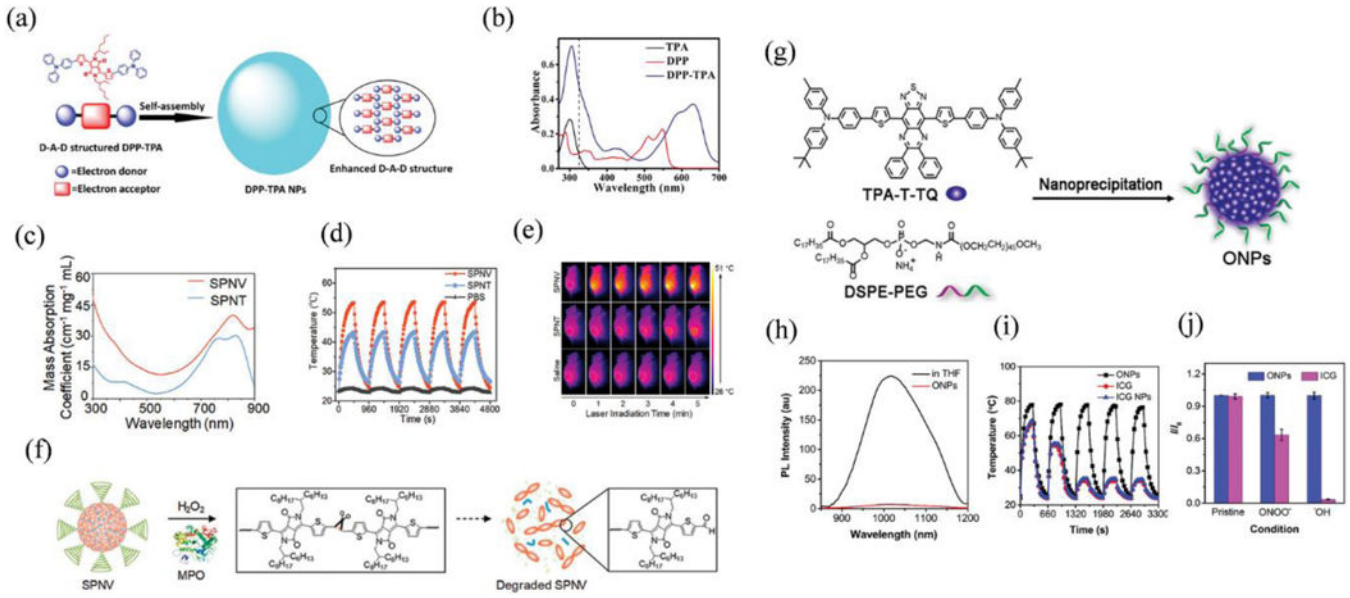

Figure 5:

(a) Schematic illustration of the enhanced D-A-D structured DPP-TPA NPs as theranostic agents for PAI guided PDT/PTT. (b) Absorption spectra of samples dissolved in toluene with a concentration of 10^{-5} mol/L. Reproduced from reference 200 with permission from American Chemical Society, copyright 2016. (c) Absorption spectra, (d) photothermal heating and natural cooling cycles, and (e) IR thermal images of 4T1 tumour-bearing mice under 808 nm laser irradiation with a power density of 0.3 W cm^{-2}. (f) Schematic illustration of the degradation of SPNV in the presence of MPO and H_2O_2. Reproduced from reference 201 with permission from American Chemical Society, copyright 2018. (g) Schematic illustration of the preparation of the TPA-T-TQ ONPs through a nanoprecipitation method and representative TEM image. (h) photoluminescence spectra of TPA-T-TQ in THF solution (black) and the encapsulated ONPs in water (red), (i) antiphotobleaching (five heating-cooling cycles) and (j) antiROS resistant property of ONPs, ICG, and ICG NPs. The power density of the 808 nm laser irradiation is 0.8 W/cm^2. Reproduced from reference 203 with permission from American Chemical Society, copyright 2017.

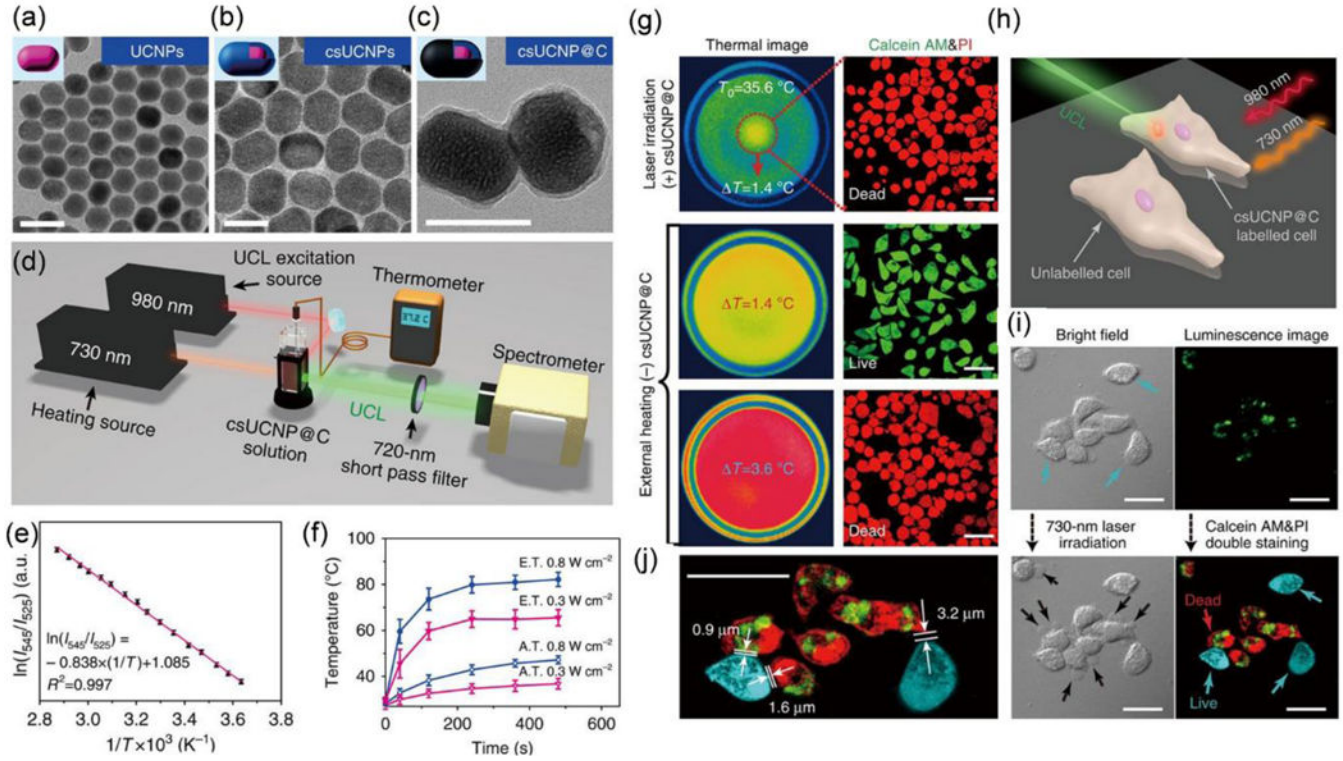

Figure 6.

(a-c) TEM images of the (a) core and (b) core-shell upconversion NPs and (c) core-shell upconversion NPs with a carbon-layer (csUCNP@C). Scale bars: 50 nm. (d) The schematic illustration of the special set-up to simultaneously characterize the macroscopic temperature rise and microscopic temperature rise of csUCNP@C NPs (e) Standard curve indicating the relationship between temperature and ratio of fluorescence intensities at two wavelengths. (f) Temperature rising curves of macroscopic (hollow triangles) versus microscopic (filled triangles) determined by the special set-up. The samples were irradiated by a laser at an intensity of 0.3 W/cm^2 (red) and 0.8 W/cm^2 (blue), respectively. (g) Thermal images and fluorescence imaging of cancer cells co-stained by Calcein AM and PI under laser irradiation (0.3 W/cm^2) or external heating. (h) Schematic illustration of the PTT of a group of adjacent cancer cells with or without csUCNP@C internalized. (i) Bright field and luminescence imaging of the group of adjacent cancer cells with or without csUCNP@C internalized before and after the laser irradiation. (j) Amplified luminescence imaging of cancer cells after the laser irradiation. Scale bars: 30 μm. Reproduced from reference 31 with licence from Creative Commons, copyright 2016

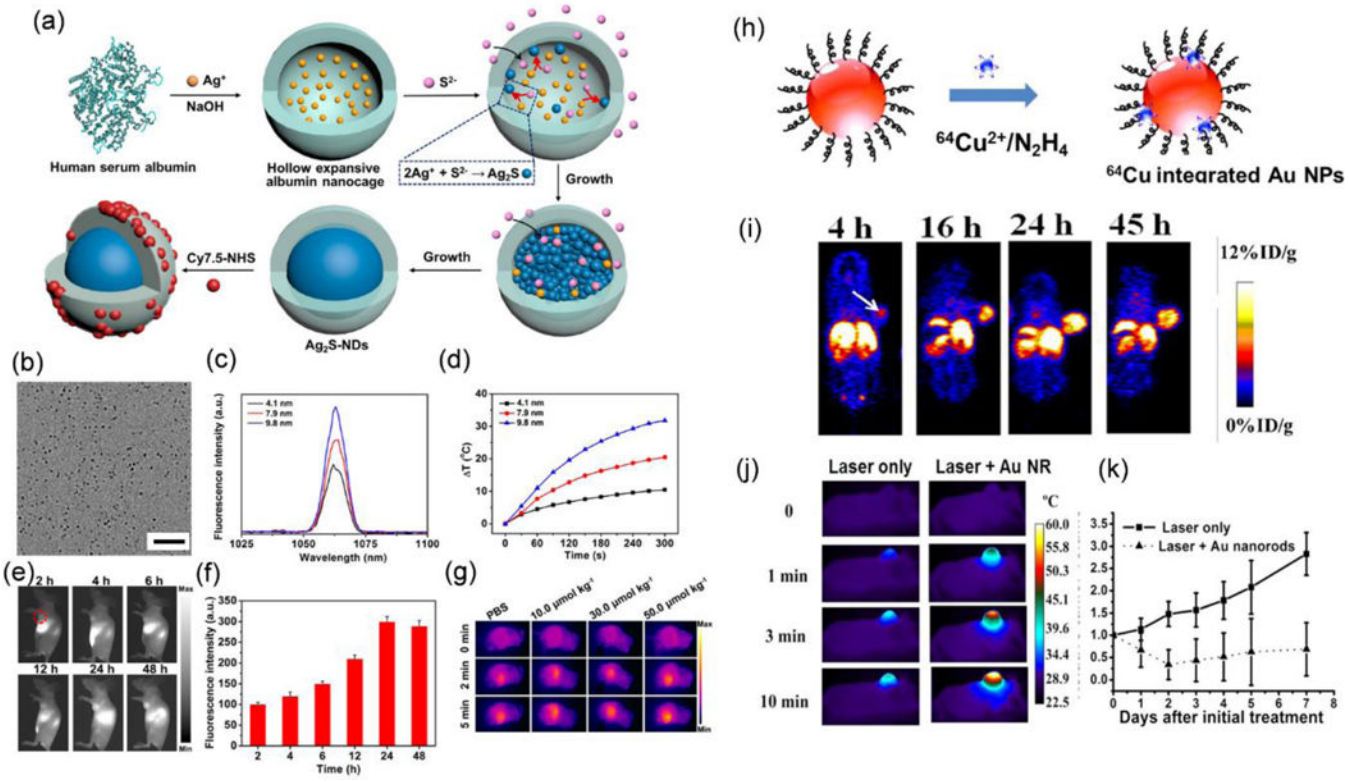

Figure 7.

(a) Schematic illustration of the synthesis of Ag_2S quantum dots using human serum proteins as templates. (b) TEM image of Ag_2S quantum dots with an average diameter of 9.8 nm. Scale bar: 100 nm. (c) Fluorescence spectra and (d) photothermal temperature rising curves of Ag_2S quantum dots with diameters of 4.1, 7.9, and 9.8 nm. (e) *In vivo* NIR-II fluorescence imaging at different times postinjection of Ag_2S quantum dots and (f) the calculated fluorescence intensities. (g) Thermal images of the tumours of tumour-bearing mice under PTT at different conditions. Reproduced from reference 131 with permission from American Chemical Society, copyright 2016. (h) Schematic illustration of the chelator free post-labelling method to chemically reduce ^{64}Cu on Au NPs. (i) Representative whole-body coronal PET images of U87MG tumour-bearing mice at 4, 16, 24, and 45 h after intravenous injection of ^{64}Cu Au nanorods with RGD targeting groups. (j) Thermal images and (k) corresponding temperature rising curves of tumours in U87MG tumour-bearing mice during PTT without and with the injection of Au nanorods with RGH targeting groups. Reproduced from reference 209 with permission from American Chemical Society, copyright 2014.

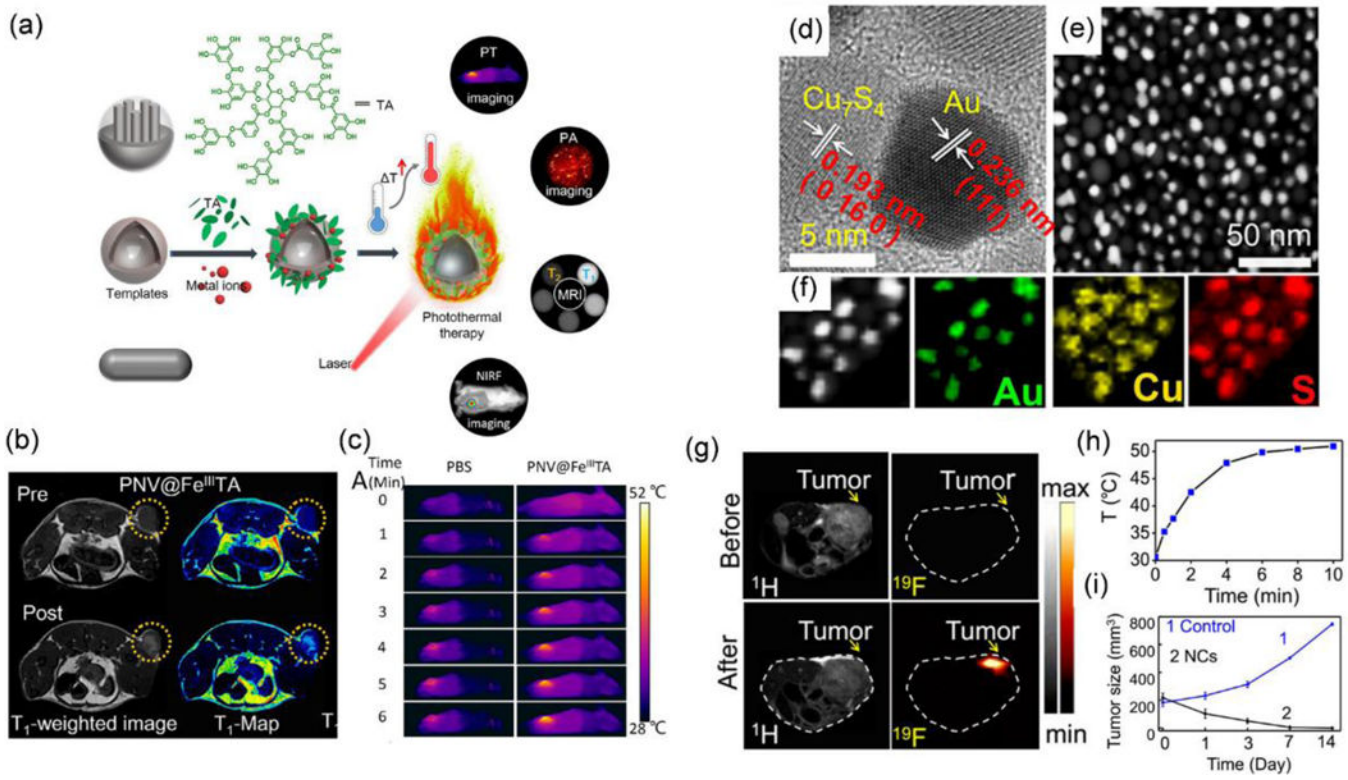

Figure 8.

(a) Schematic illustration of the synthesis of the metal ion/tannic acid shell outside NP templates for multimodal imaging and PTT. (b) The T_1-weighted MRI imaging of tumour before and after injection of polymer NP@ Fe^{III}/tannic acid shell. (c) Thermal imaging of tumours of tumour-bearing mice with the injection of PBS and polymer NP@Fe^{III}/tannic acid shell, respectively. Reproduced from reference 237 with permission from American Chemical Society, copyright 2018. (d) STEM, (e) HAADF-STEM images of the Cu_7S_4-Au NPs and (f) corresponding elemental mapping of the Cu_7S_4-Au NPs. (g) ^1H- and ^{19}F-MRI imaging of the tumour *in vivo* before and after the injection of Cu_7S_4-Au NPs. (h) Temperature rising profile of tumour areas during PTT. (i) Tumour growth curves of PTT after injection of (1) PBS and (2) Cu_7S_4-Au NPs. Reproduced from reference 241 with permission from American Chemical Society, copyright 2018.

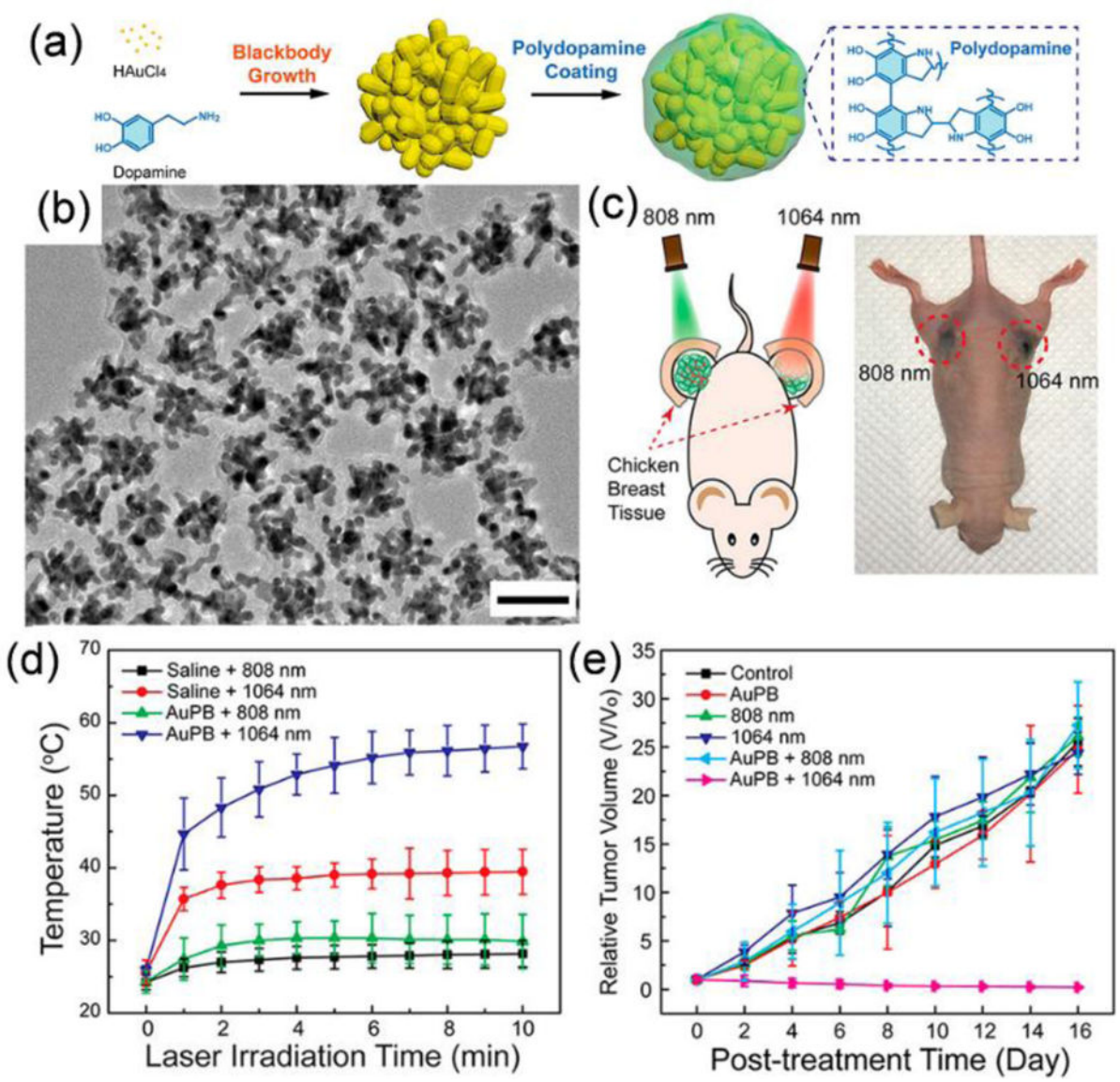

Figure 9.

(a) Schematic illustration of the synthesis of the plasmonic blackbodies by mixing dopamine and Au precursors. (b) TEM image of the plasmonic blackbodies. Scale bar: 50 nm. (c) Schematic illustration of PTT with 808 nm and 1064 nm lasers on 4T1 tumours covered by 5mm of tissues and picture of the mouse after the PTT. (d) Temperature profiles of tumour regions during PTT irradiated by 808 nm and 1064 nm lasers at their MPE dose and (e) corresponding tumour growth curves. Reproduced from reference 246 with permission from American Chemical Society, copyright 2018.

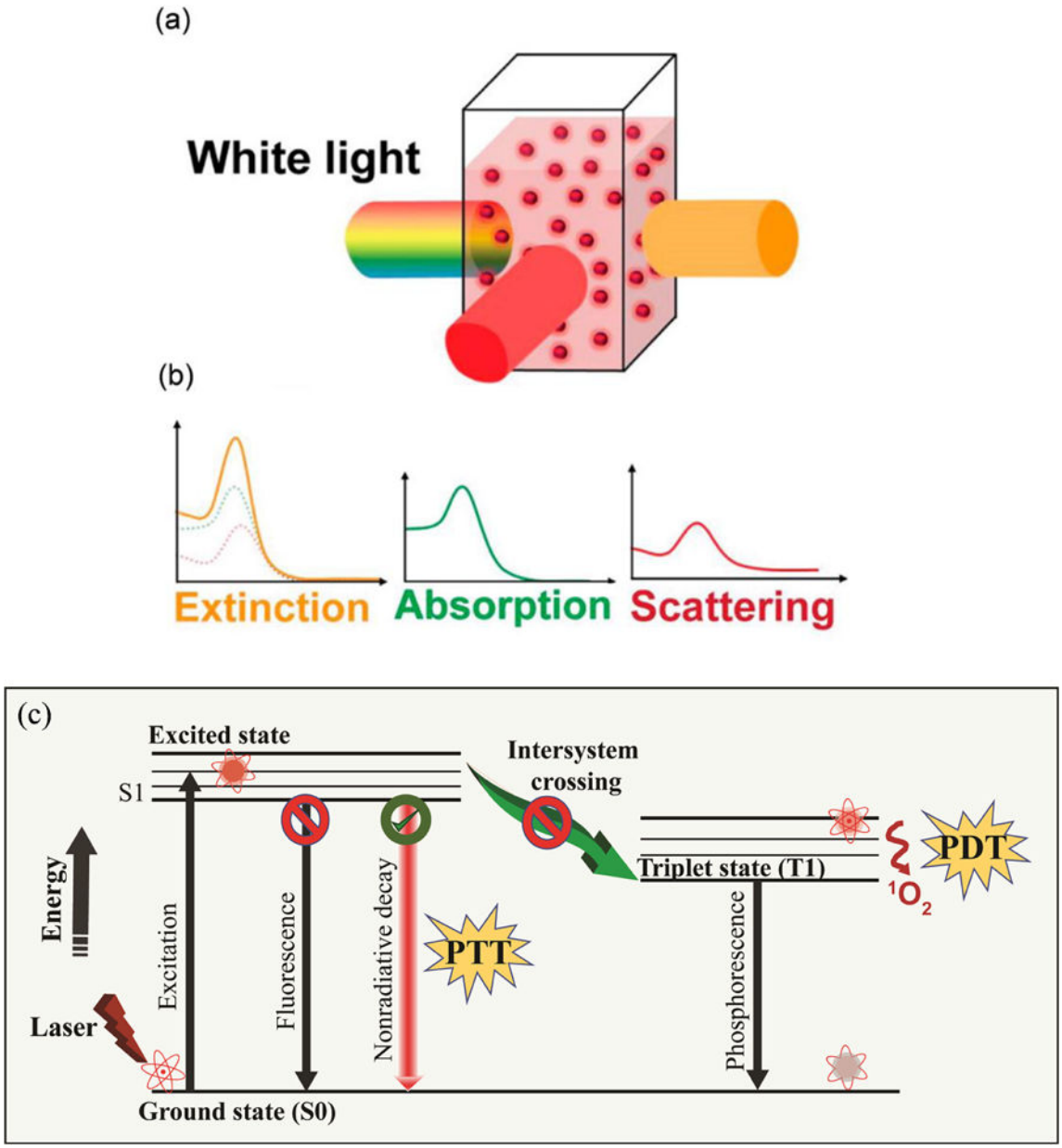

Figure 10.

(a) Schematic illustration of transmitted and scattered light upon illumination of a dispersion of NPs. (b) Schematic illustration of the contribution of absorption and scattering spectra to extinction spectrum. Reproduced from reference 252 with permission from American Chemical Society, copyright 2015. (c) Schematic Jablonski diagram representing different energy transfer mechanism.

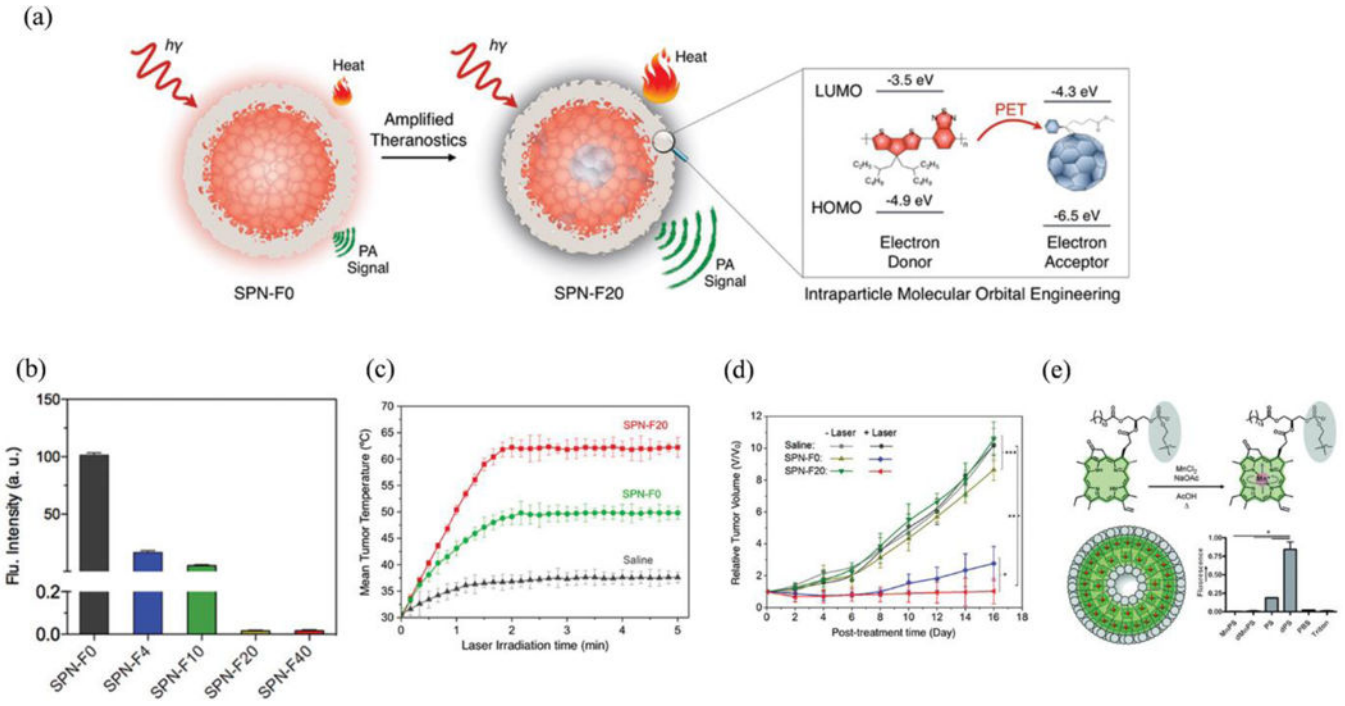

Figure 11:

(a) Illustration of photoinduced electron transfer-induced amplified theranostic SPNPs. (b) *In vitro* quantification of fluorescence. (c) *In vivo* PTT: Mean tumour temperature as a function of laser irradiation time (at post-injection time of 6 h) and (d) tumour growth curves of different groups of mice (with and without laser irradiation) after systemic administration of saline, SPNP-F0, or SPNP-F20. Error bars were based on standard error of mean (SEM) (*$p < 0.05$, **$p < 0.01$, ***$p < 0.001$, $n = 4$). Reproduced from reference 266 with permission from American Chemical Society, copyright 2016. (e) Schematic representation for the synthesis of Mn-porphysome nanovesicles and singlet-oxygen generation by porphysomes after 1 min of laser irradiation (671 nm, 100 mW cm^{-2}) as quantified by singlet oxygen sensor green (SOSG) fluorescence ($n = 3$, *$p < 0.05$). Reproduced from reference 268 with permission from Wiley, copyright 2014.

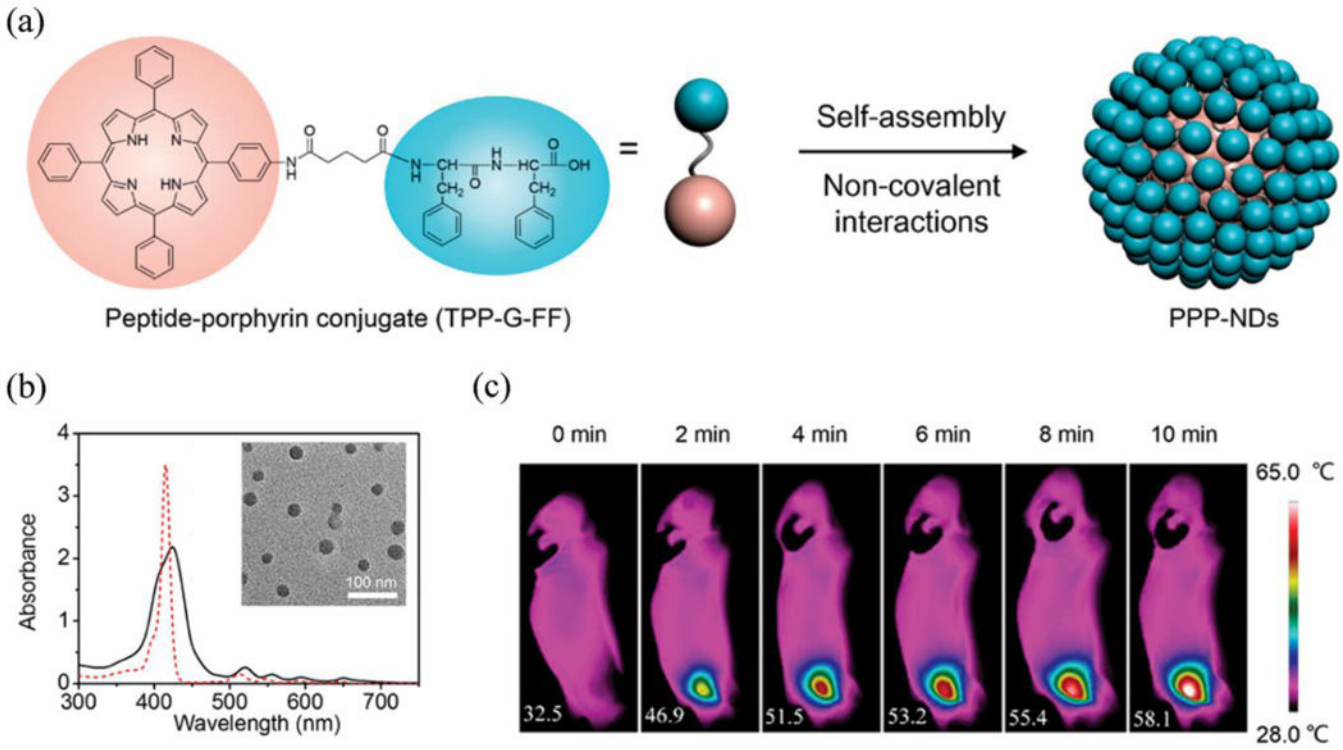

Figure 12:

(a) Molecular structure and self-assembly of a peptide−porphyrin conjugate (TPP-G-FF) into photothermal peptide−porphyrin nanodots (PPP-NDs). (b) UV−vis absorption spectra of PPP-NDs in water (black) and TPPG-FF in ethanol (red) (Inset: TEM image). (c) IR thermal images of intravenous PPP-NDs injected mice under continuous irradiation *in vivo*. Reproduced from reference 275 with permission from American Chemical Society, copyright 2017.

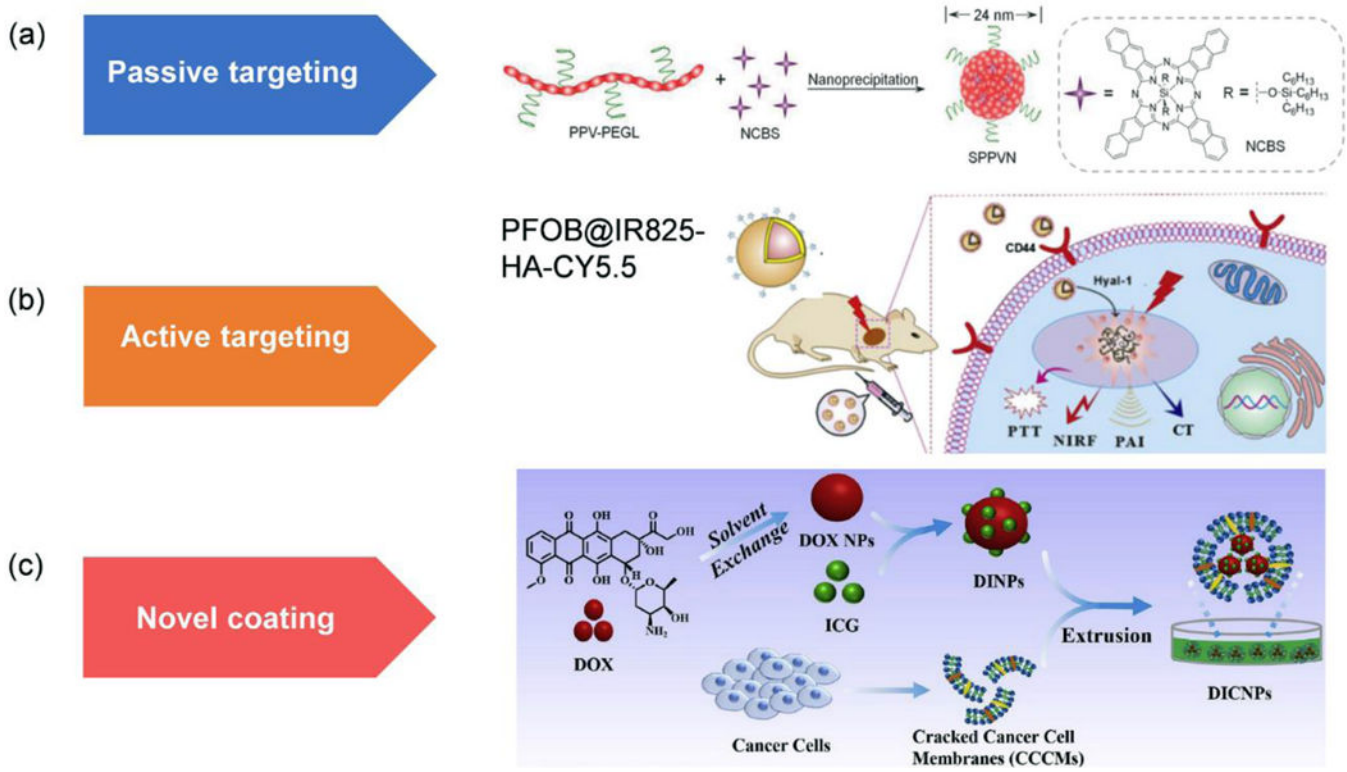

Figure 13.

(a) Schematic illustration of the synthesis of SPPVNs with PEG coating that accumulate in tumours by passive targeting. Reproduced from reference 302 with permission from Wiley-VCH, copyright 2018. (b) Schematic illustration of accumulation of PFOB@IR825-HA-CY5.5 NPs in tumours by active targeting. Reproduced from reference 312 with permission from Elsevier Ltd, copyright 2017. (c) Schematic illustration of the synthesis of Dox NPs@ICG@CCC NPs with cancer cell membrane coating. Reproduced from reference 318 with permission from Elsevier Ltd, copyright 2018

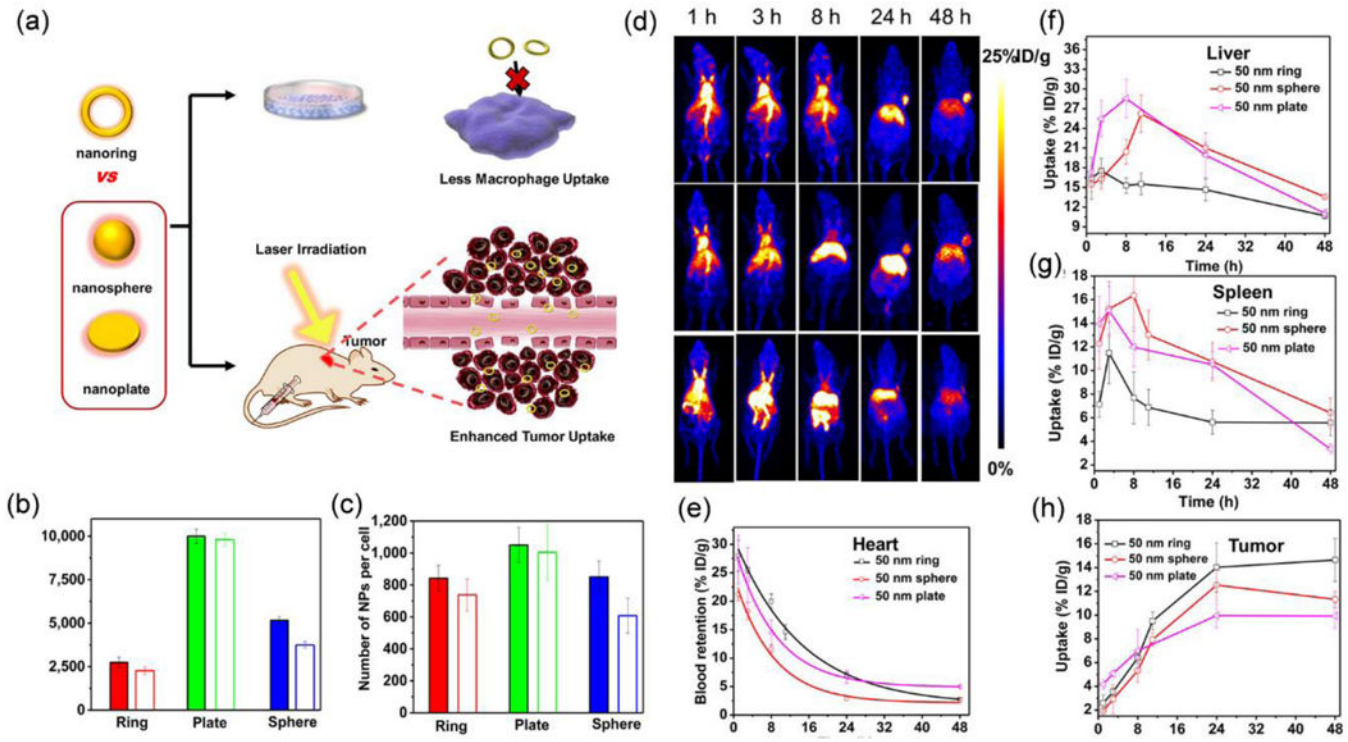

Figure 14.

(a) Schematic illustration of the investigation of shape effects of Au nanorings, Au nanospheres, and Au nanoplates on macrophage uptake and tumour accumulation. (b,c) The macrophage uptake of Au nanorings, Au nanoplates, and Au nanospheres at (b) 37 ^{0}C for 8 h and (c) and 4 ^{0}C for 1 h without (filled) and with (hollow) preformed protein corona. (d) Representative whole-body coronal PET images of the mice at different time postinjection indicating the biodistribution and tumour accumulation of Au nanorings, Au nanospheres, and Au nanoplates (from top to bottom) and the corresponding time-activity curves of the mean uptake of these nanostructures in (e) hearts, (f) livers, (g) spleens, and (h) tumours. Reproduced from reference 43 with permission from American Chemical Society, copyright 2017.

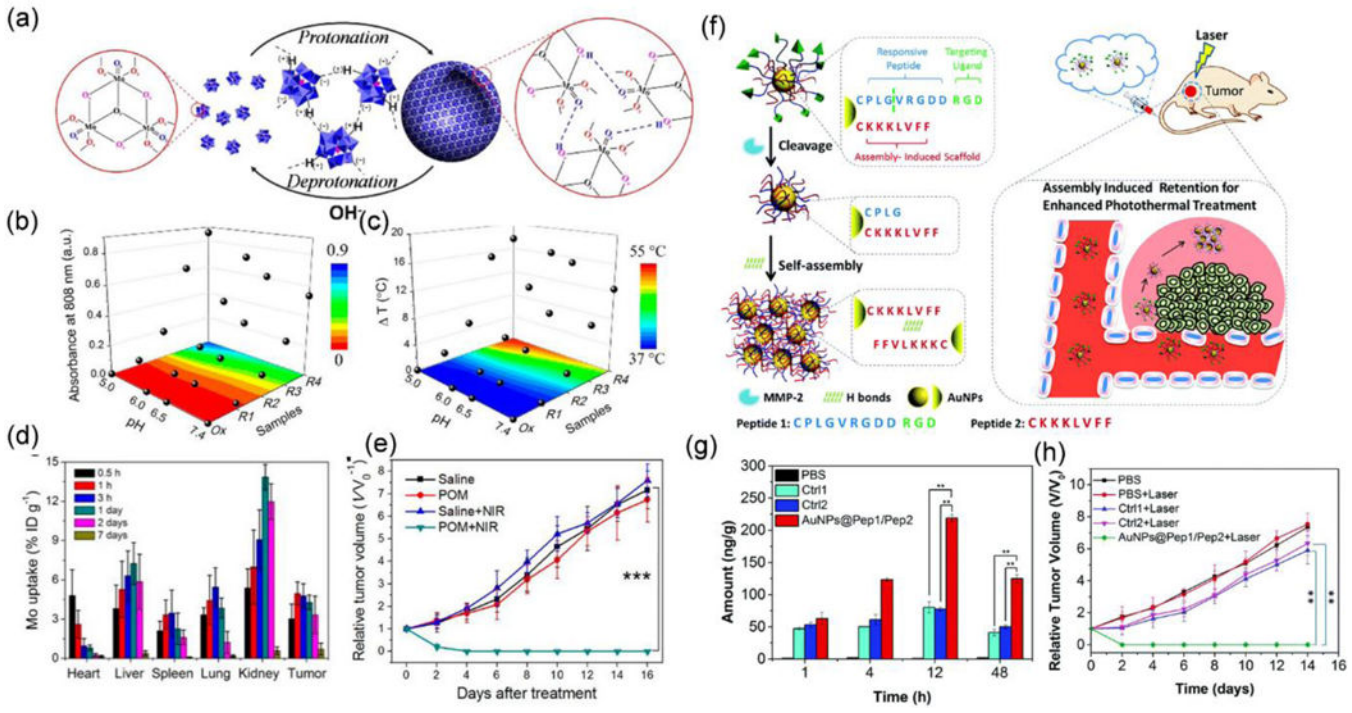

Figure 15.

(a) Schematic illustration of the self-assembly of POM clusters into large aggregates in an acidic environment. (b) diagram indicating enhanced absorption at 808 nm of POM clusters solutions in acidic pH and reduction environments and (c) their corresponding temperature upon irradiation by an 808 nm laser (1.5 W/cm^{-2}, 5 min). (d) The biodistribution and tumour accumulation of POM clusters at different time points postinjection. (e) Tumour growth curves of PTT with POM injected and other control groups. Reproduced from reference 284 with permission from American Chemical Society, copyright 2016. (f) Schematic illustration of the MMP-2 induced self-assembly of peptide-stabilized Au NPs into large aggregations. (g) Quantification of the tumour accumulation of Au NPs@Pep1/Pep2, Ctrl 1 and Ctrl 2 at different time points postinjection. Ctrl 1 represents Au NPs stabilized by only MMP-2 responsive Pep 1. Ctrl 2 represents Au NPs stabilized by MMP2-irresponsive Peptide 1 and Peptide 2. (h) Tumour growth curves of PTT with Au NPs@Pep1/Pep2 injected and other control groups. Reproduced with permission from Royal Society of Chemistry, copyright 2017.

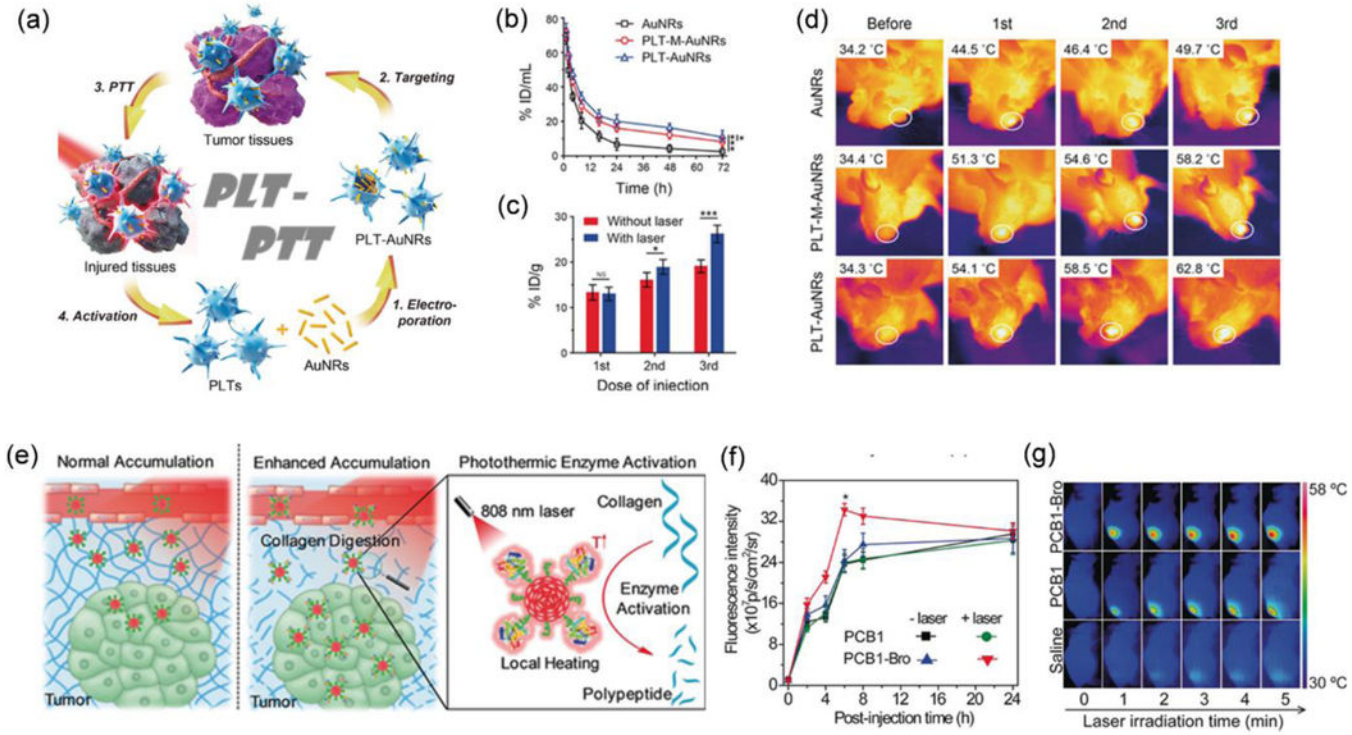

Figure 16.

(a) Schematic illustration of the preparation of PLT-Au nanorods and photothermally induced enhancement of tumour uptake of PLT-Au nanorods for improved PTT. (b) The blood concentration of Au after injection of Au nanorods (black), PLT membrane-cloaked Au nanorods (PLT-M-Au nanorods) (red), and PLT-Au nanorods (blue). (c) The tumour accumulation of PLT-Au nanorods after subsequent doses of injections with or without laser irradiation. (d) Representative thermal images of HNSCC-bearing Tgfbr1/Pten 2cKO mice before and after each photothermal treatment. From top to bottom were mice injected with Au nanorods, PLT-M-Au nanorods, and PLT-Au nanorods, respectively. Reproduced from reference 296 with permission from Wiley-VCH, copyright 2017. (e) Schematic illustration of the photothermally triggered enhanced digestion activity of PCB-Bro toward collagen to increase the NP accumulation in tumour. (f) Fluorescence intensity of tumour regions at different time postinjection of PCB and PCB-Bro with or without irradiation of tumour regions with NIR lasers. (g) Thermal images of tumour-bearing mice at 6 postinjection of PCB-Bro (first row), PCB (second row), and saline (third row) with the tumour exposed to a NIR laser for 5 min. Reproduced from reference 341 with permission from Wiley-VCH, copyright 2018.

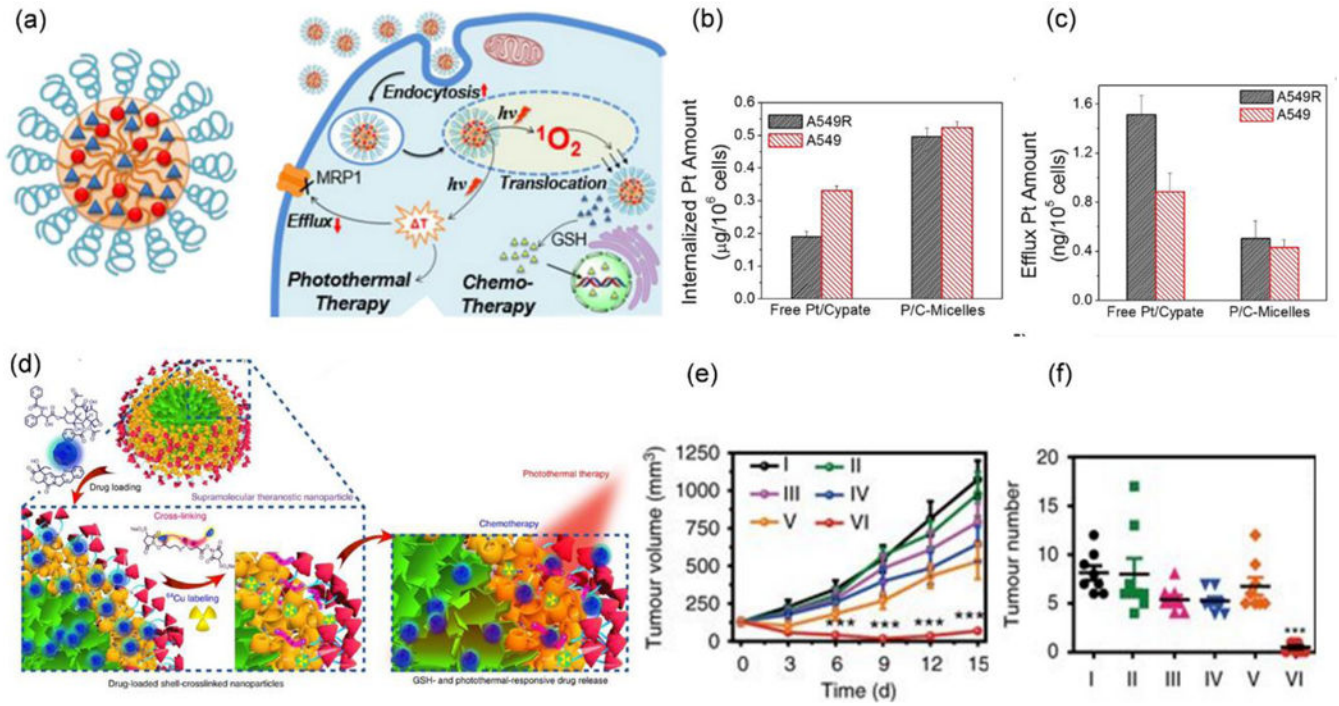

Figure 17.

(a) Schematic illustration of the micelles containing Pt(IV) prodrug and Cypate (P/C-micelles) for overcoming MDR and a combination of PTT and chemotherapy. (b) The uptake of Pt(IV) prodrug by A549R and A549 cells as the form of free drug or payloads of P/C-micelles. (c) Efflux of Pt(IV) prodrug from A549R and A549 cells after incubation with free Pt(IV) prodrug or Pt(IV) prodrug containing micelles. Reproduced from reference 350 with permission from American Chemical Society, copyright 2015. (d) Schematic illustration of the release of drug from supramolecular micelles triggered by photothermal and GSH. (e) Tumour growth curves in an orthotopic 4T1 tumour model treated with a combination of PTT and chemotherapy and other control therapies. The treatment conditions were: (I) PBS, (II) supramolecular micelles with PTX (PTX, 20 mg/kg), (III) Abraxane (PTX, 20 mg/kg), (IV) supramolecular micelles (PTX, 60 mg/kg), (v) supramolecular micelles + laser, and (VI) supramolecular micelles with PTX (PTX, 60 mg/kg) + laser and (f) The numbers of tumour nodules present on the lung surface from each group. Reproduced from reference 351 with licence from Creative Commons, copyright 2018

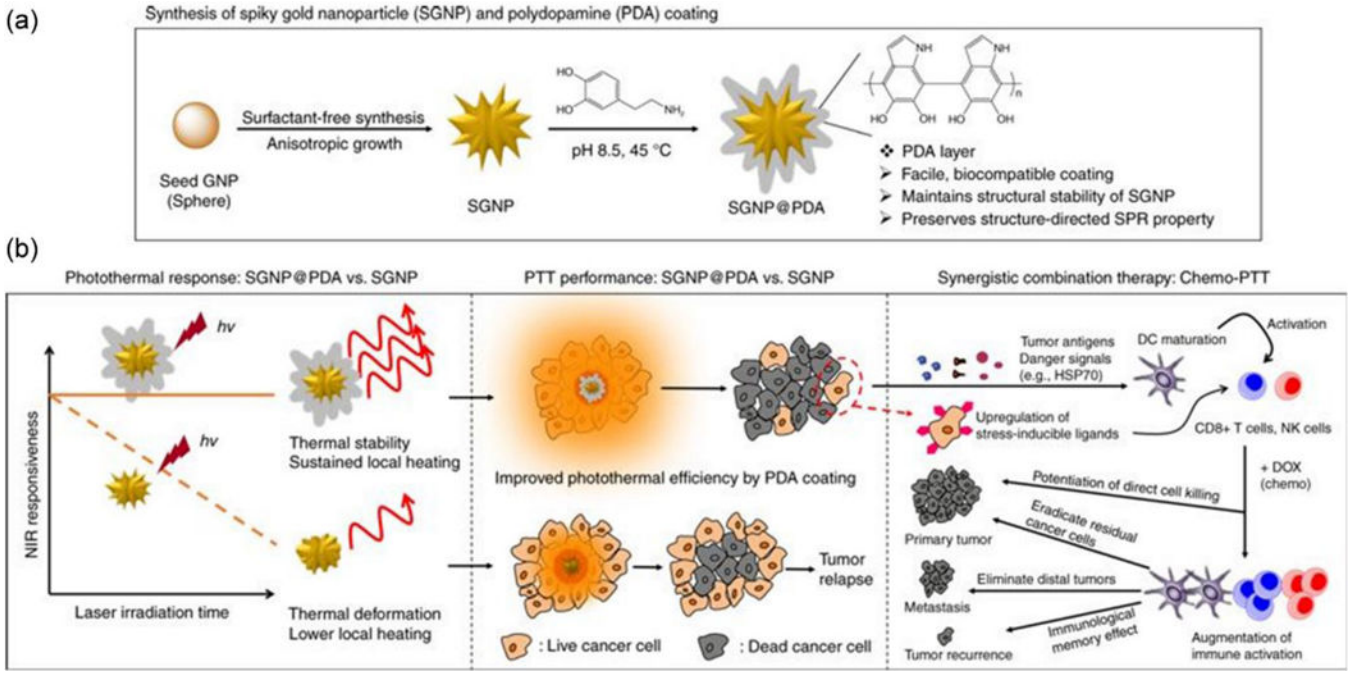

Figure 18.

(a) Schematic illustration of the synthesis of spiky Au NP@dopamine core-shell NPs (SGNP@PDAs) (b) The schematic illustration of how the combination of PTT and a sub-therapeutic dose of Dox triggered anti-tumour immunity for the treatment of primary tumours and tumour metastases and prevention of tumour recurrence. Reproduced from reference 357 with licence from Creative Commons, copyright 2018

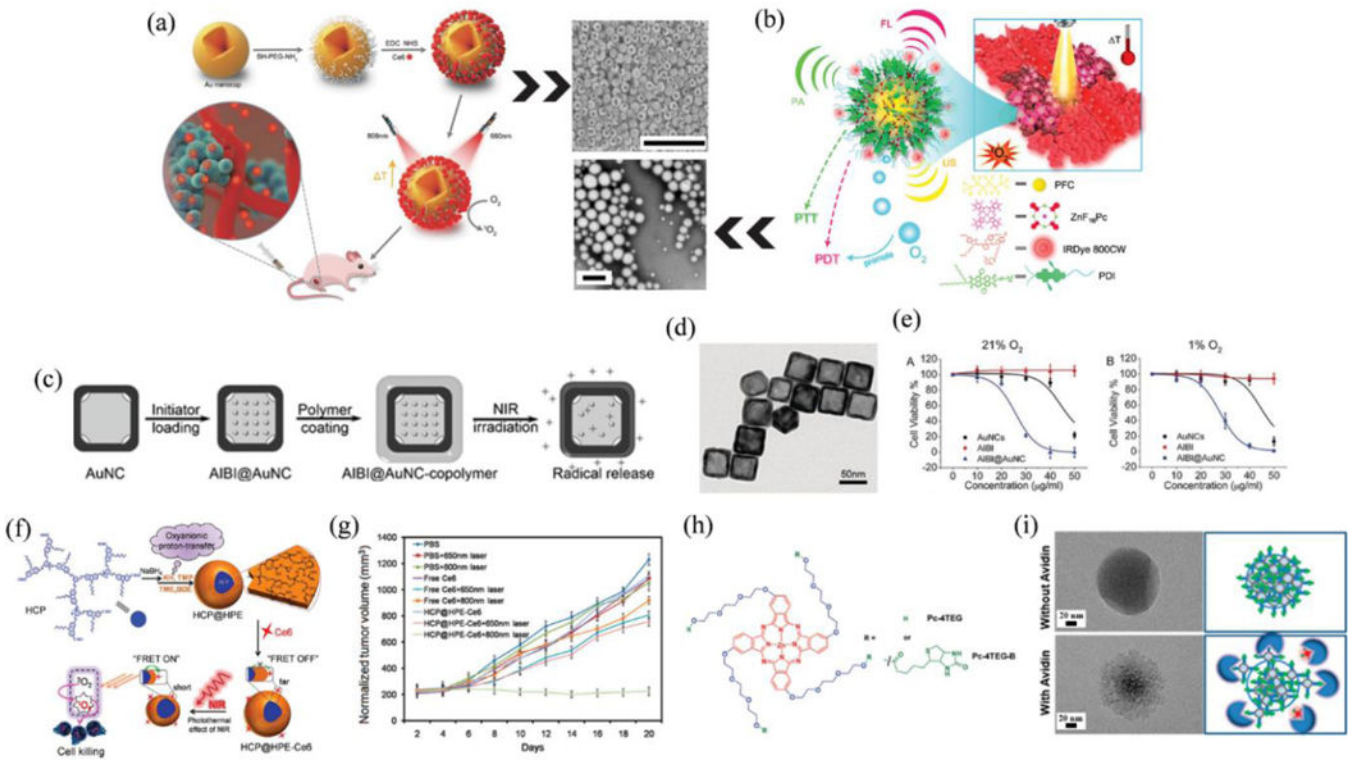

Figure 19:

(a) Schematic illustration of Au nanocage-Ce6 nanostructure for phototherapy followed by a representative SEM image of Au nanocups. Scale bar: 1μm. Reproduced from reference 380 with permission from Wiley, copyright 2017. (b) IRDye800CW-labeled photosensitizer $ZnF_{16}Pc$ loaded PDI nanodroplet (PS-PDI-PAnD) for *in vivo* multimodal imaging-guided combinational photothermal and oxygen self-enriched PDT and representative TEM image. Scale bar: 200 nm. Reproduced from reference 245 with permission from American Chemical Society, copyright 2018. (c) AIBI@Au nanocage copolymer synthesis and its NIR-responsive free-radical releasing ability. (d) TEM images of Au nanocages. (e) Phototoxicity of Au nanocages (0–50 μg mL^{-1}), AIBI (0–50 μg mL^{-1}), and AIBI@Au nanocage (0–50 μg mL^{-1}) to 4T1 cells under normoxic and hypoxic conditions. Reproduced from reference 382 with permission from Wiley, copyright 2017. (f) Synthesis of thermoresponsive HCP@HPE unimolecular micelles and illustration of the combination of the 2P-FRET and photothermal effect of NIR for PDT. (g) *In vivo* tumour growth in HeLa-tumour-bearing nude mice after irradiation of 650 nm or 800 nm. Reproduced from reference 383 with permission from American Chemical Society, copyright 2016. (h) Chemical structure of the building block, Pc-4TEG, and Pc-4TEG-B. (i) NanoPcTB morphology changes in water before and after adding avidin and after standing for 24 h, as determined using TEM. The right column illustrates the proposed mechanisms for the morphology changes. Avidin/NanoPcTB mole ratio is 1/1. Reproduced from reference 384 with permission from American Chemical Society, copyright 2017.

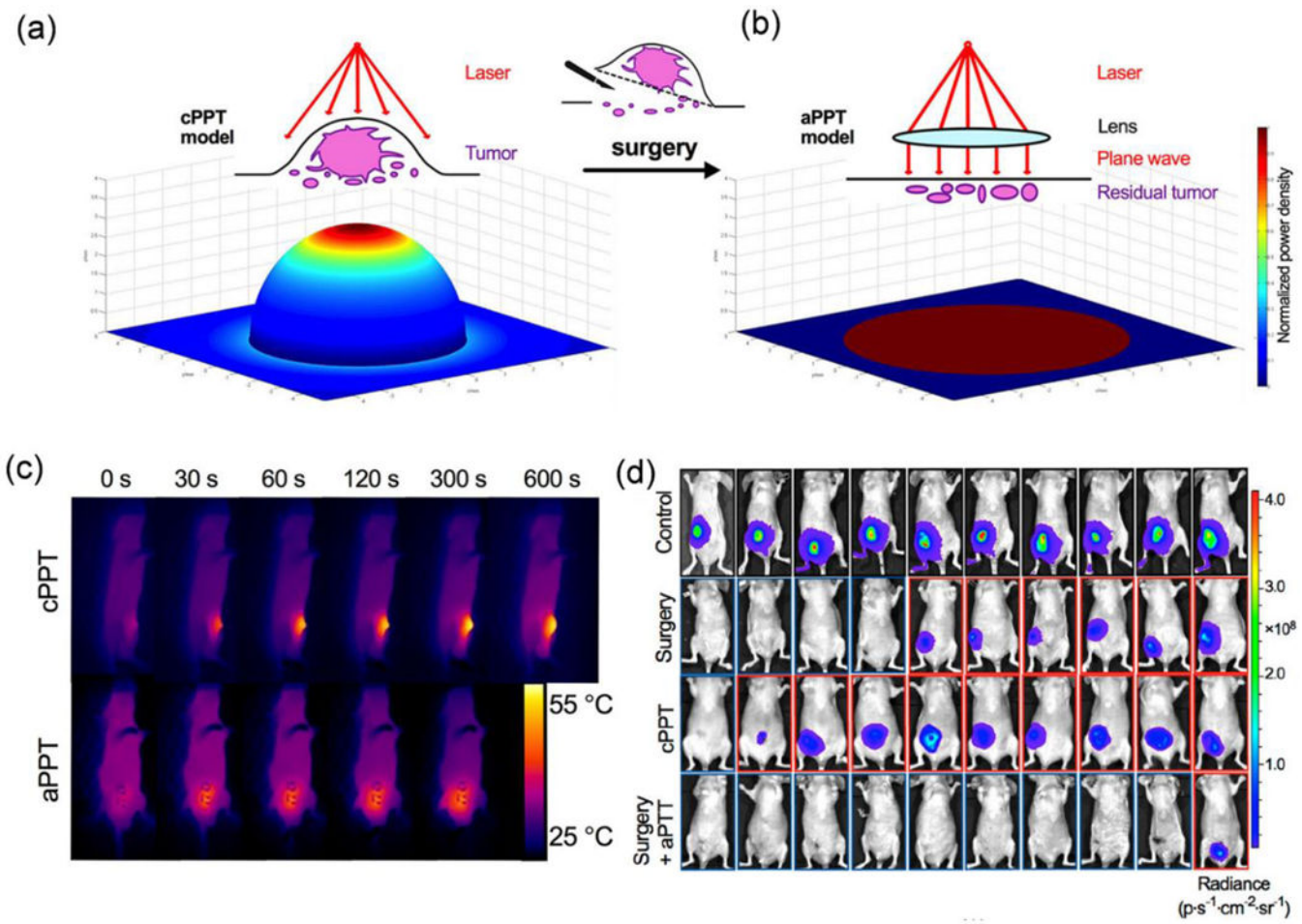

Figure 20.

(a) Schematic illustration of conventional PTT (cPTT) and simulated distribution of laser energy in the tumour area. (b) Schematic illustration of aPTT and simulated distribution of laser energy in surgical bed. (c)Thermal images of tumour-bearing mice during cPTT (2.5 W/cm^2) and aPTT (1 W/cm^2). (d) Bioluminescent images of different groups of tumour-bearing mice with different treatment, including control group, group treated with surgery only, group treated with cPTT only, and the group treated with a combination of surgery and aPTT (from top to bottom). Reproduced from reference 394 with permission from American Chemical Society, copyright 2018

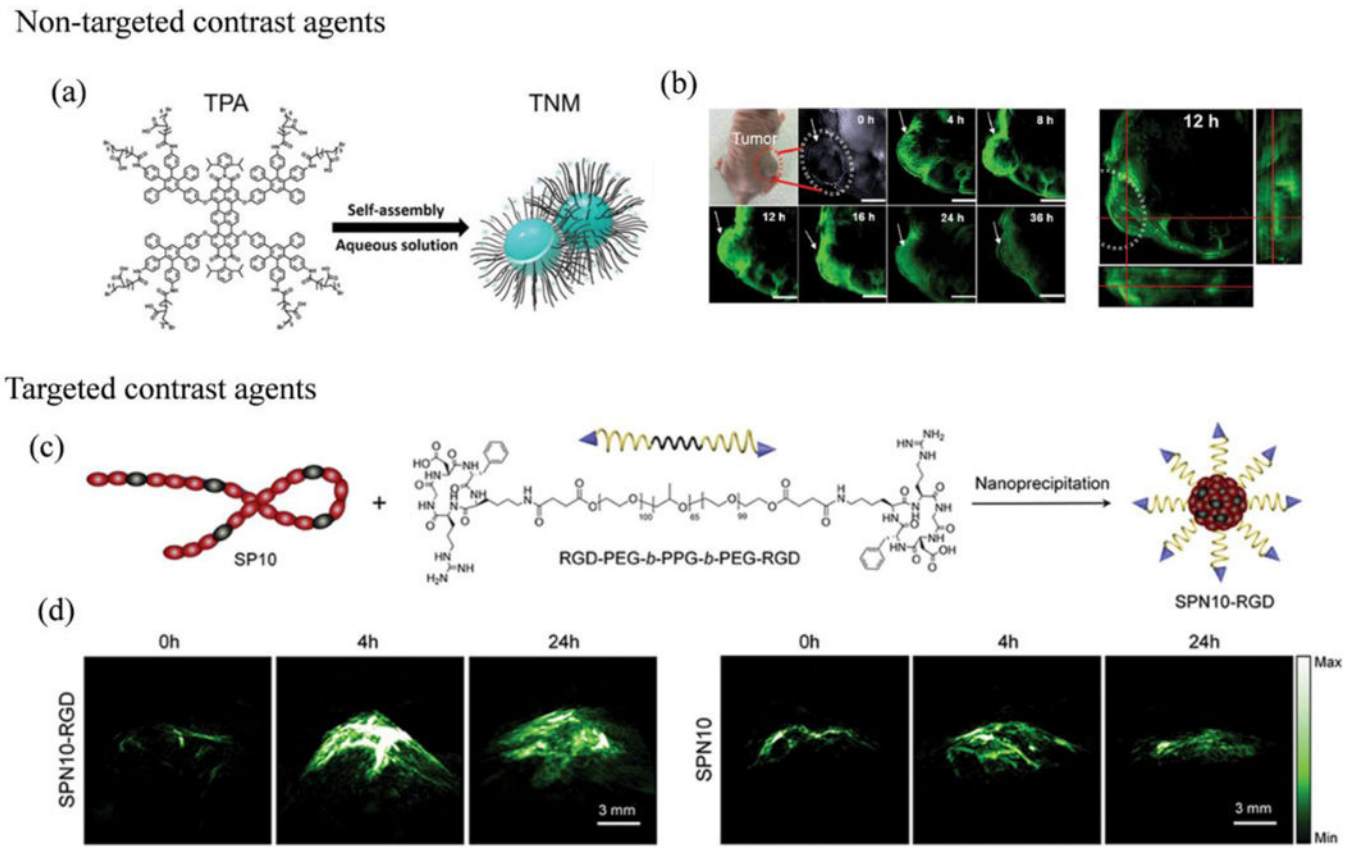

Figure 21:

(a) Basic chemical structures of TPAs and illustration of theranostic TNMs through self-assembly. (b) *In vivo* photoacoustic (MSOT) images of tumours tissue (arrows) at different time points (0, 4, 8, 12, 16, 24, and 36 h) after injection of TNMs *via* tail vein under 710 nm laser irradiation. Scale bar: 3 mm. The 3D MSOT image and enlarged orthogonal views of tumour at 12 h post-injection based on image reconstruction. Reproduced from reference 34 with permission from American Chemical Society, copyright 2017. (c) Synthesis of the targeted SPNP (SPNP10-RGD). (d) *In vivo* PAI of the tumour after systemic administration of SPNP10-RGD or SPNP10 (30 μg in 120 μL) for 0, 4 and 24 h, respectively. The representative photoacoustic maximum imaging projection (MIP) images with an axial view for SPNP10-RGD and SPNP10. Reproduced from reference 418 with permission from Elsevier, copyright 2017.

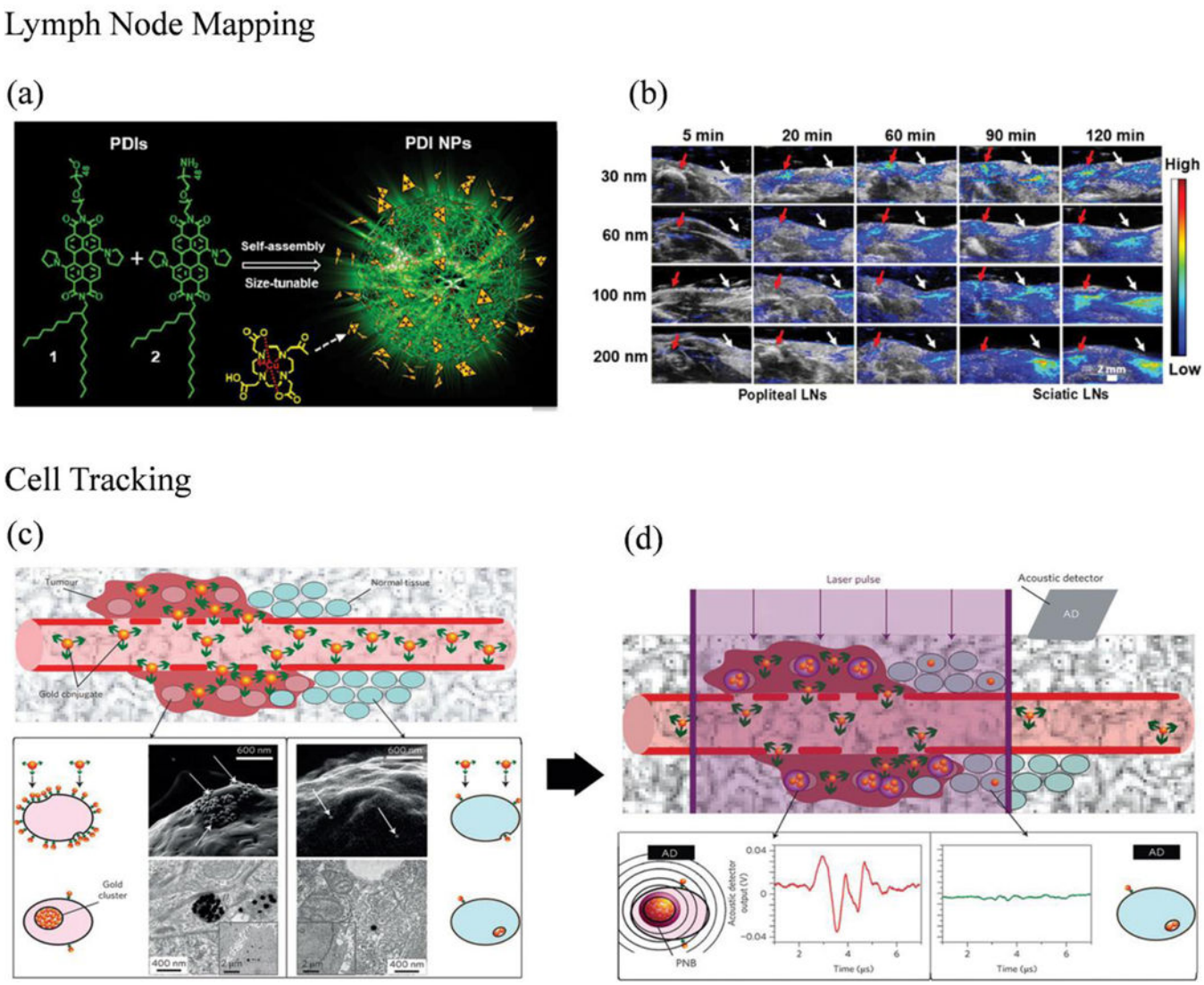

Figure 22:

(a) Schematic illustration of the synthesis of PDI NP. (b) Representative overlaid coronal PAI and ultrasound images that show size-dependent uptake in popliteal lymph nodes (LNs) and sciatic LNs at different time points postinjection. Reproduced from reference 42 with permission from American Chemical Society, copyright 2017. (c) Systemic delivery and accumulation of Au conjugates to the tumour *via* their leaky vasculature *in vivo*. Representative SEM images of cancer cells showing Au NPs accumulation and intracellular clustering *f* receptor-mediated endocytosis. (d) The acoustic signal of a PNB (illustrative red time response) reports even a single cancer cell in the solid tissue, but not normal cells (illustrative green time response). Reproduced from reference 57 with permission from Springer Nature, copyright 2016.

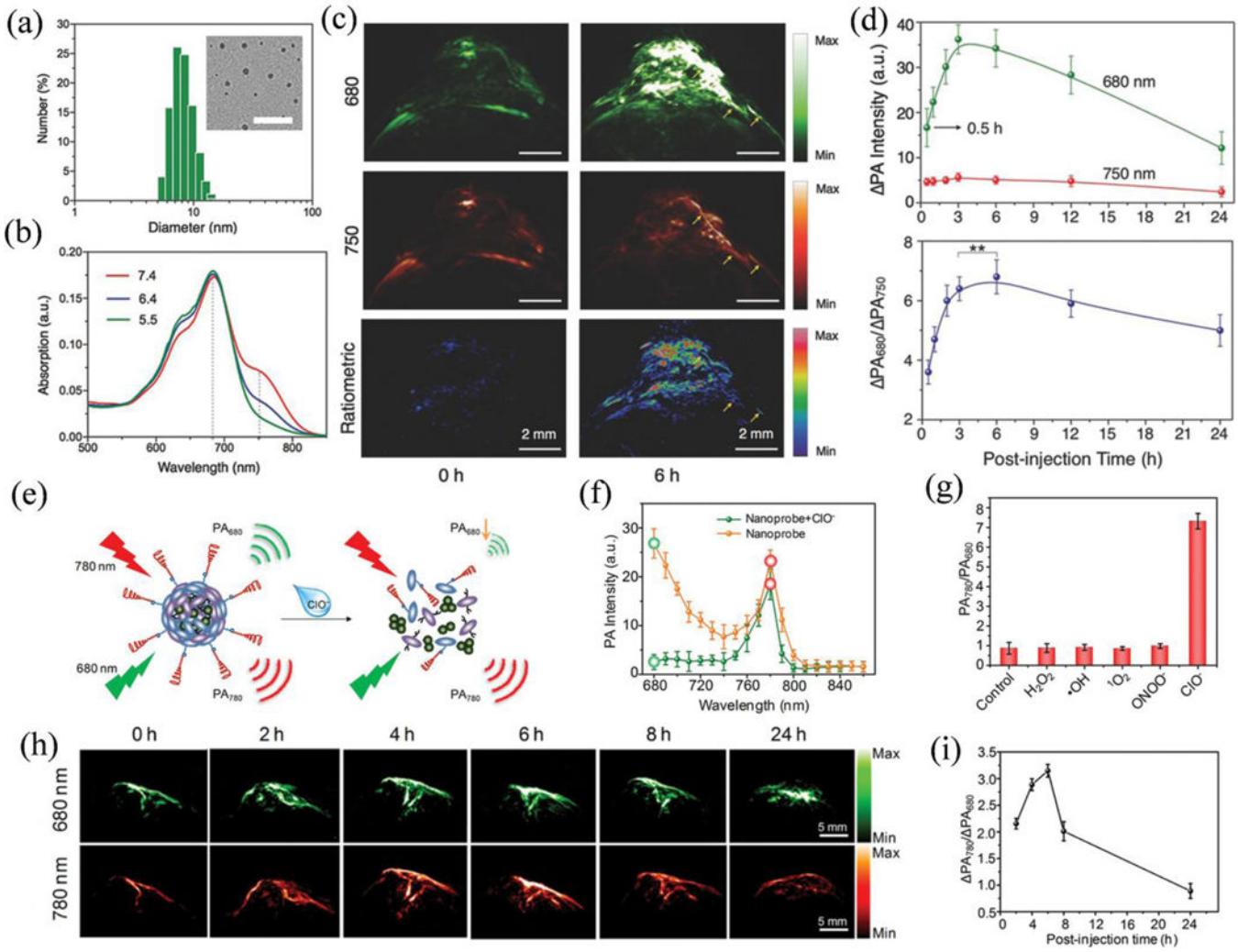

Figure 23:

(a) Dynamic light scattering, TEM image (Scale bar: 50 nm) and (b) UV–vis absorption spectra of SON_{50} at different pH. (c) Photoacoustic and ratiometric images ($\Delta PAI_{680}/\Delta PAI_{750}$) of a subcutaneous HeLa tumour in a nude mouse before and 6 h after intravenous administration of SON_{50}. (d) Quantification of the photoacoustic intensity increment at 680 nm and ratiometric photoacoustic signals as a function of time post-injection of SON_{50}. **No statistically significant difference in ratiometric signals between 3 and 6 h ($p>0.05$). Reproduced from reference 434 with permission from Wiley, copyright 2016. (e) Schematic illustration of the sensing mechanism for the SOA nanoprobe. (f) *In vitro* PAI in the absence and presence of ClO^- and (g) Ratiometric photoacoustic responses (PAI_{780}/PAI_{680}) toward different ROS in PBS buffer. (h) *In vivo* PAI of a subcutaneous 4T1 tumour in a nude mouse before and 2, 4, 6, 8, and 24 h after intravenous administration of the nanoprobe and ratiometric photoacoustic signals as a function of postinjection time. (i) Ratiometric quantitation of photoacoustic signals as a function of postinjection time. Reproduced from reference 441 with permission from American Chemical Society, copyright 2017. The representative PA maximum intensity projection (MIP) images with an axial view are demonstrated in both. The error bars represent the SD of three separate measurements (n=3)

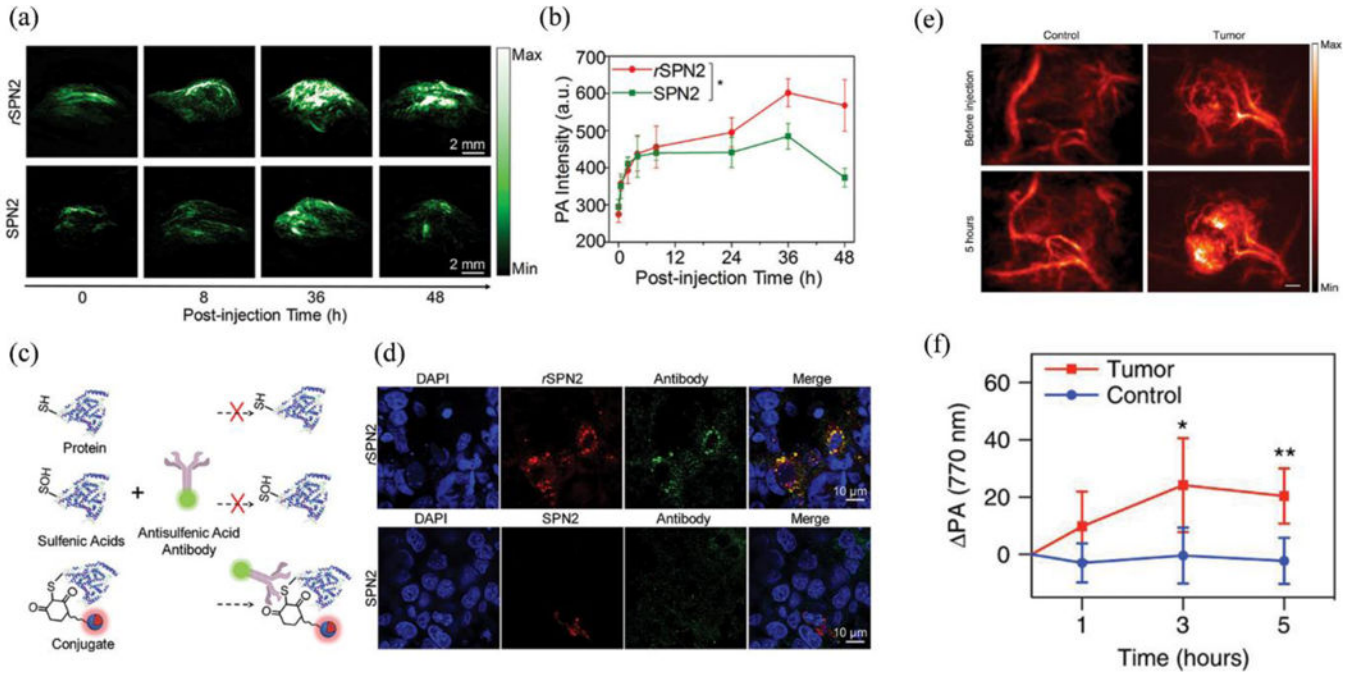

Figure 24:

(a) *In vivo* PAI and (b) quantification of protein sulfenic acids using rSPNP2 or SPNP2. The representative photoacoustic maximum intensity projection (MIP) images with an axial view. (c) Illustration of the mechanism and histological analysis of immunofluorescence staining with the antisulfenic acid antibody. (d) Fluorescence microscopy of tumour slices for mice treated with rSPNP2 or SPNP2 at 48 h of postinjection. (red signals from rSPNP2 or SPNP2, green signals from the staining with an antisulfenic acid antibody, and blue from the nucleus staining. Reproduced from reference 447 with permission from American Chemical Society, copyright 2016. (e) *In vivo* photoacoustic images (770 nm) of the tumour-bearing and control flank before and 5 h following injection of HyP-1. (Scale bar: 2 mm). (f) Time-dependent photoacoustic signal of ischemic limb and control. Results with error bars are represented as mean ± SD. *$p < 0.05$, **$p < 0.01$ (n=4). Reproduced from reference 448 with licence from Creative Commons, copyright 2017.

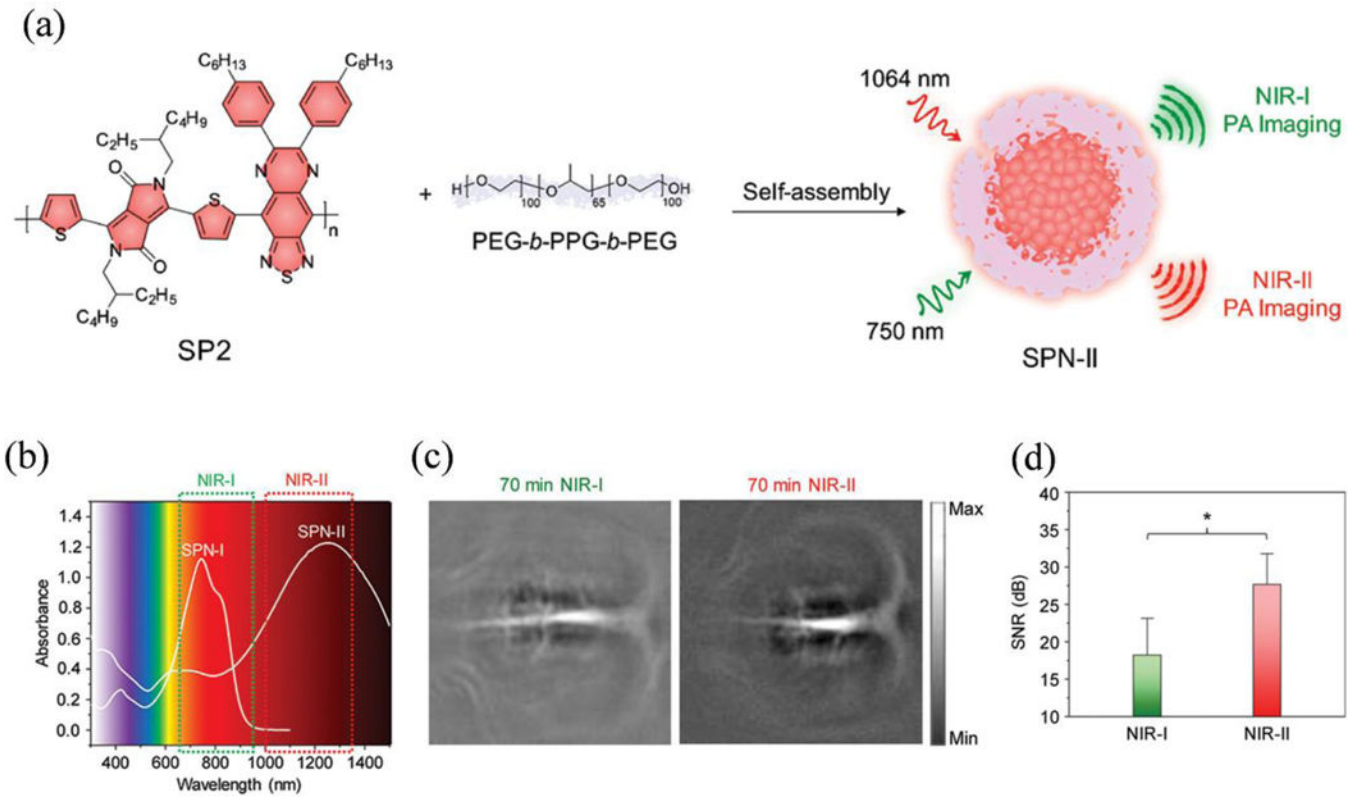

Figure 25:

(a) Schematic illustration for preparation of SPNP-II. (b) UV−vis-NIR absorption spectra of SPNP-II. (c) *In vivo* PAI and (d) SNR of rat brain cortex at 70 min postinjection of SPNP-II at 750 (NIR-I) and 1064 nm (NIR-II). *Statistically significant difference ($p < 0.05$, $n = 3$). Reproduced from reference 459 with permission from American Chemical Society, copyright 2017.